

Oxidative activation of methane over MgO model catalysts

vorgelegt von
Master of Science
Pierre Schwach
geb. in Strasbourg (Frankreich)

von der Fakultät II – Mathematik und Naturwissenschaften
der Technischen Universität Berlin
zur Erlangung des akademischen Grades

Doktor der Naturwissenschaften
- Dr. rer. nat. -

genehmigte Dissertation

Promotionsausschuss:

Vorsitzender: Prof. Dr. Martin Lerch (Technische Universität Berlin)
Berichter/Gutachter: Prof. Dr. Robert Schlögl (Fritz-Haber-Institut der MPG)
Berichter/Gutachter: Prof. Dr. Reinhard Schomäcker (Technische Universität Berlin)
Berichter/Gutachter: Prof. Dr. Klaus Rademann (Humboldt-Universität zu Berlin)

Tag der wissenschaftlichen Aussprache: 11.11.2014

Berlin 2015

Oxidative activation of methane over MgO model catalysts

Pierre Schwach



Berlin 2014

Oxidative activation of methane over MgO model catalysts

Pierre Schwach

Dissertation
at Faculty of Chemistry
Technical University
Berlin

Submitted by
Pierre Schwach
born in Strasbourg (France)

Berlin, 11.11.2014

First referee: Prof. Dr. Robert Schlögl

Second referee: Prof. Dr. Reinhard Schomäcker

Third referee: Prof. Dr. Thomas Risse

Date of oral examination: 11.11.2014

”God created the solids, the devil their surfaces”

– Wolfgang Pauli –

Acknowledgement

First and foremost I would like to express my profound gratitude and deep respect to Prof. Robert Schlögl who gave me the great opportunity of working at his Department of Inorganic Chemistry at the Fritz Haber Institute of the Max Planck Society. His profound intellect and immense knowledge has been a motivation and inspiration for my work.

I also need to deeply thank my supervisor, Dr. Annette Trunschke, for her continuous support and her endless patience. Her advice and constant scientific input have been a guidance during my PhD whilst allowing me the freedom to develop my own ideas.

Besides my advisors, I would like to thank all the members of the examination committee: Prof. Reinhard Schomäcker at the Technical University Berlin for hosting me as an external student. I am grateful to Prof. Thomas Risse at the Free University of Berlin for kindly agreeing to be part of my examination committee. I also thank Prof. Martin Lerch at the Technical University Berlin for taking the chair during the defense.

I would like to express my gratitude to all the members of the Inorganic Chemistry Department and especially the members of the reactivity group for the warm working atmosphere, the inspiring chats, moral support, and constant help.

I am deeply grateful to all colleagues that contributed by performing experiments, technical assistance and fruitful discussion and without whom the conduction of this work would not have been possible. I would like to acknowledge the following people (in no particular order): Jutta Kröhnert (IR), Dr. Genka Tzolova-Müller (UV-vis), Maike Hashagen (N₂ physisorption, IR, ICP), Dr. Frank Girgsdies (XRD), Gisela Weinberg (SEM-EDX), Dr. Tom Cotter (discussion), Edith Kitzelmann (XRD, TG), Gisela Lorenz (N₂ physisorption), Achim Klein-Hoffmann (XRF), Dr. Neil G. Hamilton (IR, discussion), Dr. Andrey Tarasov (TG), Siegfried Engelschalt (catalytic setup and technical support), Dr. Benjamin Frank (discussion), Wiebke Frandsen (TEM, SEM, discussion), Dr. Marc Willinger (TEM, discussion), Jasmin Allan (XRD), Julia Neuendorf (XRD), Stefanie Kühl (XRD), Pia Nielsen (BET), Dr. Kazuhiko Amakawa (discussion), Daniel Brenneke (synthesis), Dr. Olaf Timpe

(technical assistance, ICP), Iris Pieper (from TU Berlin, ICP-MS), Stefan Schulz (synthesis), Dr. Maik Eichelbaum (EPR, discussion), Cyriac Massue (discussion), Dr. Thomas Lunkenbein (TEM), Lukas Thum (synthesis, discussion).

I would like to thank Horst Schwäricke and Georg Heyne and their teams in the mechanical and electronical workshop. I also thank the glassblower Horst Müller for his collaboration.

Finally I thank family and friends for their support, patience, unceasing encouragement and love.

Abstract

The role of surface structure and defects in the oxidative coupling of methane (OCM) was studied over magnesium oxide as a model catalyst. Pure MgO nano-particles with varying primary particle size, shape and specific surface area were prepared by sol-gel synthesis, oxidation of metallic magnesium and hydrothermal post treatments. Kinetic studies reveal the occurrence of two parallel reaction mechanisms and a change in the contribution of these pathways to the overall performance of the catalysts with time on stream. The surface of the MgO catalysts has been studied by FTIR and photoluminescence spectroscopy in the dehydroxylated state before and after catalysis. The resulting observations show that the activity of MgO in the OCM reaction is clearly structure-sensitive.

The initial performance of freshly calcined MgO is governed by a surface-mediated coupling mechanism involving direct electron transfer between methane and oxygen. The abundance of structural defects, in particular mono-atomic steps and Lewis acid/base pairs correlate with the initial rates of both methane consumption and C₂₊ hydrocarbon formation. Infrared spectroscopy evidences strong polarization of C-H bonds due to adsorption of methane on dehydroxylated MgO surfaces that contain a high number of mono-atomic steps. It is postulated that these sites effectively promote intermolecular charge transfer between adsorbed methane and weakly adsorbed oxygen that leads to the dissociation of one C-H bond in the methane molecule and simultaneous formation of activated species, like superoxide. The proposed mechanism is consistent with high methane conversion, a correlation between methane and oxygen consumption rates, and high ethylene selectivity after short times on stream.

During time on stream MgO sinters and loses activity in the steam-containing atmosphere at the high reaction temperatures of OCM. The deactivation process involves the depletion of mono-atomic steps and the reconstruction of the MgO termination under formation of polar and faceted surfaces as indicated by photoluminescence spectroscopy. At the same time, gas phase chemistry becomes more important, which includes formation of ethane by gas phase coupling of methyl radicals formed at the surface and the pyrolysis of ethane. Kinetic data reveal that ethylene is mainly not a secondary product from oxidative dehy-

drogenation of ethane.

Since the deactivation of MgO is a self-poisoning process induced by the formation of water in the catalytic reaction, an alternative concept has been proposed to stabilize the catalyst at high activity levels. The concept is based on doping of MgO with transition metal ions in ppm concentrations. Over diluted solid solutions of transition metals in alkaline earth oxides the mechanism of methane activation changes from an intermolecular charge transfer mechanism into a redox process involving charge transfer between the surface and the reactants due to an electronic doping effect. Small amounts of iron increased the catalytic performance and stability of MgO considerably despite particle sintering. The addition of atomically dispersed gold to Fe-MgO, which adsorbs on surface steps (and preferentially mono-atomic steps), enhances the electronic doping effect further.

Zusammenfassung

In der vorliegenden Arbeit wurde reines Magnesiumoxid als Modellkatalysator in der oxidativen Kopplung von Methan (OCM) untersucht, wobei Fragen nach dem Einfluss von Defekten und der Oberflächenstruktur auf die katalytischen Eigenschaften im Mittelpunkt standen. Zu diesem Zweck wurde eine Reihe reiner MgO-Katalysatoren unter Anwendung verschiedener Präparationsmethoden, wie Sol-Gel-Synthese, Oxidation von metallischem Magnesium und hydrothormaler Nachbehandlung von MgO, hergestellt. Die Katalysatoren zeichneten sich durch unterschiedlicher Primärpartikelgröße, -form und spezifische Oberfläche aus. Kinetische Studien zeigten, dass an reinem MgO mindestens zwei verschiedene Reaktionsmechanismen parallel ablaufen, deren Beitrag zum Gesamtumsatz sich mit der Reaktionszeit ändert. Die spektroskopische Charakterisierung der Oberfläche deckte Zusammenhänge zwischen Reaktivität und Oberflächenstruktur auf, die klar zeigen, dass die oxidative Kopplung von Methan über MgO eine strukturempfindliche Reaktion ist.

Die Anfangsleistung von frisch kalziniertem MgO wird durch einen Oberflächen-katalysierten Kopplungsmechanismus bestimmt, der eine direkte Elektronenübertragung zwischen adsorbiertem Methan und adsorbiertem Sauerstoff beinhaltet. Die mittels FTIR-Spektroskopie bestimmte Konzentration von mono-atomaren Stufen und Kanten (Lewis Säure / Basenpaaren) an der Katalysatoroberfläche korreliert mit den Anfangsgeschwindigkeiten des Methanverbrauchs und der C₂₊ Kohlenwasserstoffbildung (C₂₊ entspricht der Summe von Ethan und Ethylen, sowie höherer Kohlenwasserstoffe). Wie durch Infrarotspektroskopie nachgewiesen werden konnte, tritt eine starke Polarisierung der C-H Bindungen im Methan bei Adsorption des Moleküls an mono-atomaren Stufen auf. Es wird postuliert, dass an diesen Zentren ein intermolekularer Ladungstransfer zwischen adsorbiertem Methan und schwach gebundenem Sauerstoff stattfindet, durch den eine C-H Bindung gespalten und eine Superoxid-Spezies gebildet werden können. Die konzertierte Aktivierung von zwei Methanmolekülen kann zur direkten Bildung von Ethylen und Wasser an der Katalysatoroberfläche führen. Der vorgeschlagene Mechanismus steht im Einklang mit experimentellen Beobachtungen, wie einem hohen Methanumsatz unter Anfangsbedingungen, einer Korrelation zwischen den Verbrauchsgeschwindigkeiten von Methan und Sauerstoff und einer hohen Ethylenselektivität zu Beginn der Reaktion.

In der wasserdampfhaltigen Reaktionsatmosphäre sintert MgO, was zu einer Desaktivierung der Katalysatoren durch Abbau der mono-atomaren Stufen und zur Rekonstruktion der MgO Terminierung unter Bildung polarer und facettierter Oberflächen führt. Diese strukturellen Veränderungen konnten durch FTIR- und Photolumineszenzspektroskopie nachgewiesen und mittels Elektronenmikroskopie bestätigt werden. Zur gleichen Zeit nehmen die Beiträge der Gasphasenchemie zur Reaktivität zu. Dazu zählen die Kopplung von an der Oberfläche gebildeten Methylradikalen zu Ethan und dessen Pyrolyse zu CO. Kinetischen Daten zeigten, dass Ethylen in erster Linie kein Produkt einer oxidativen Dehydrierung von Ethan ist.

Da es sich bei der Desaktivierung des Katalysators um eine Selbstvergiftung durch gebildetes Reaktionswasser handelt, wird zur Stabilisierung hoher Aktivitäten ein alternatives Konzept vorgeschlagen, das auf einer elektronischen Dotierung von MgO mit Übergangsmetallionen beruht. Dabei geht der Mechanismus in einen Redox-Mechanismus über. Zum Beispiel konnte durch Dotierung von MgO mit Fe (in ppm Konzentrationen) die Anfangsaktivität trotz Sinterns stabilisiert werden. Dieser Effekt konnte durch Gold-Zusätze noch verstärkt werden.

Table of contents

Acknowledgement	viii
Abstract	xi
Zusammenfassung	xiii
List of Figures	xxii
List of Tables	xxiii
List of schemes	xxiv
List of supporting tables	xxiv
List of supporting figures	xxvi
1 Introduction	1
1.1 General introduction	1
1.2 Reaction mechanism	2
1.3 Technical aspects	3
1.4 Methane activation	4
1.5 Oxygen activation	5
1.6 MgO as model catalyst: synthesis and reactivity	6
1.7 Characterization of the surface properties of MgO	8
1.8 Doping theory	9
1.9 Motivation and aim of the thesis	9
1.10 Outline of the thesis	10
2 Kinetic study	11
2.1 Introduction	12
2.2 Experimental	14
2.2.1 Starting materials	14
2.2.2 Catalyst synthesis	14

2.2.3	Nitrogen adsorption	15
2.2.4	X-ray diffraction	16
2.2.5	Elemental analysis	16
2.2.6	Electron microscopy	16
2.2.7	Oxidative coupling of methane	16
2.3	Results	18
2.3.1	Synthesis of nano-structured MgO catalysts	18
2.3.2	Oxidative coupling of methane	22
2.4	Discussion	32
2.5	Conclusion	39
2.6	Supporting information	40
3	Nature of active sites and reaction mechanism	45
3.1	Introduction	46
3.2	Experimental	47
3.2.1	Catalysts and chemicals	47
3.2.2	Infrared spectroscopy	47
3.2.3	EPR spectroscopy	48
3.2.4	Diffuse reflectance spectroscopy	48
3.2.5	Electron microscopy	49
3.2.6	Photoluminescence	49
3.3	Results	49
3.3.1	IR spectroscopy	50
3.3.2	Photoluminescence (PL) spectroscopy	61
3.3.3	ESR spectroscopy	65
3.4	Discussion	67
3.4.1	Structural changes of the MgO surface during the OCM reaction . .	67
3.4.2	Activation of methane on the dehydroxylated MgO surface	68
3.4.3	Active sites under stationary conditions	72
3.5	Conclusion	73
3.6	Supporting information	75
3.6.1	UV-vis spectroscopy	75
3.6.2	Photoluminescence spectroscopy	76
3.6.3	IR spectra deconvolution	78
4	How doping can work	83
4.1	Introduction	83
4.2	Results and discussion	86
4.3	Conclusion	91

4.4	Experimental Section	91
4.5	Supporting information	92
	Supporting information	92
4.5.1	Experimental Details	92
4.5.2	Diffuse reflectance spectroscopy	96
4.5.3	EPR spectroscopy	96
4.5.4	Temperature-programmed-reduction-oxidation (TPR-TPO)	97
4.5.5	Oxidative coupling of methane	98
4.5.6	Electron microscopy	100
5	Conclusions	101
	Bibliography	103

List of Figures

2.1	TEM images of calcined MgO (on the left-hand side) and MgO after oxidative coupling of methane for 300 hours time on stream ($\text{CH}_4/\text{O}_2/\text{N}_2=3/1/1$, $W/F=0.15 \text{ g}\cdot\text{s}\cdot\text{ml}^{-1}$, $T=1073 \text{ K}$) (on the right-hand side). From top to bottom: S-MgO (A,B), C-MgO (C,D), SG-MgO (E,F), HT-MgO (G,H), and MW-MgO (I,J).	21
2.2	Changes in the conversion of methane (A) and in the selectivity to C_{2+} products (B) with time on stream in the oxidative coupling of methane at $T=1073 \text{ K}$ in a feed of $\text{CH}_4/\text{O}_2/\text{N}_2=3/1/1$, using a catalyst mass of $m_{\text{cat}}=150 \text{ mg}$, and applying a contact time of $W/F=0.15 \text{ g}\cdot\text{s}\cdot\text{ml}^{-1}$ over the differently prepared MgO catalysts.	22
2.3	Change in the selectivity ratio ethylene/ethane (A), and CO_2/CO (B) with time on stream in the same experiments as presented in Fig. 2.2.	23
2.4	Changes in the selectivity to the products ethylene, ethane, CO, and CO_2 with time on stream exemplarily shown for catalyst C-MgO in the same experiments as presented in Fig. 2.2.	24
2.5	TEM images of C-MgO at different time on stream in the OCM reaction, same experimental condition as in Fig. 2.2. A) Before reaction ($S_{\text{BET}}=53.9 \text{ m}^2\cdot\text{g}^{-1}$), B) after 6 h TOS ($S_{\text{BET}}=22.3 \text{ m}^2\cdot\text{g}^{-1}$), C) after 20 h TOS ($S_{\text{BET}}=16.4 \text{ m}^2\cdot\text{g}^{-1}$), D) after 66 h TOS ($S_{\text{BET}}=15.0 \text{ m}^2\cdot\text{g}^{-1}$).	25
2.6	Total yield of the coupling products ethane and ethane for all catalysts (A), and conversion and selectivity exemplarily shown for C-MgO (B) as a function of the contact time at $T=1023 \text{ K}$, using a catalyst mass of $m_{\text{cat}}=150 \text{ mg}$, and a feed composition of $\text{CH}_4/\text{O}_2/\text{N}_2=3/1/1$	25
2.7	Total selectivity to the coupling products ethane and ethane as a function of methane conversion (A), and selectivity to C_2 , and C_3 hydrocarbons exemplarily shown for catalyst C-MgO as a function of methane conversion (B) measured at $T=1023 \text{ K}$, using a catalyst mass of $m_{\text{cat}}=150 \text{ mg}$, and a feed composition of $\text{CH}_4/\text{O}_2/\text{N}_2=3/1/1$. The conversion was changed by variation of the contact time in the range between 0.1 and $0.4 \text{ g}\cdot\text{s}\cdot\text{ml}^{-1}$. . .	27

2.8	Total selectivity to the coupling products ethane and ethane over SiC as a function of methane conversion measured by variation of the contact time (A) (same condition as in Fig. 2.7) and by variation of the temperature (B) (same condition as in Fig. 2.10).	28
2.9	Total yield of the coupling products ethane and ethene (A), and conversion and selectivity exemplarily shown for catalyst C-MgO as a function of the CH_4/O_2 ratio in the feed at $T=1023\text{ K}$, using a catalyst mass of $m_{\text{cat}}=150\text{ mg}$, and a contact time of $0.15\text{ g}\cdot\text{s}\cdot\text{ml}^{-1}$	28
2.10	Total yield of the coupling products ethane and ethane (A), and conversion and selectivity exemplarily shown for C-MgO (B) as a function of the temperature, using a catalyst mass of $m_{\text{cat}}=150\text{ mg}$, a contact time of $0.15\text{ g}\cdot\text{s}\cdot\text{ml}^{-1}$ and a feed composition of $\text{CH}_4/\text{O}_2/\text{N}_2=3/1/1$	30
2.11	Concentration of ethane measured at the outlet of the reactor for all catalysts (A), and concentration of all products as well as methane and oxygen conversion exemplarily shown for catalyst C-MgO (B) as a function of ethane added to the feed at 1023 K , CH_4/O_2 ratio of 3, and constant contact time of $0.15\text{ g}\cdot\text{s}\cdot\text{ml}^{-1}$. The black straight line corresponds to zero conversion of the added ethane.	31
2.12	Concentration of ethylene measured at the outlet of the reactor for all catalysts (A), and concentration of all products as well as methane and oxygen conversion exemplarily shown for catalyst C-MgO (B) as function of ethylene added in the gas feed at 1023 K , CH_4/O_2 ratio of 3, and constant contact time of $0.15\text{ g}\cdot\text{s}\cdot\text{ml}^{-1}$. The black straight line corresponds to zero conversion of the added ethylene.	32
2.13	Methane and oxygen conversion and concentration of products as function of CO_2 added to the feed over C-MgO at 1023 K , CH_4/O_2 ratio of 3, and contact time of $0.15\text{ g}\cdot\text{s}\cdot\text{ml}^{-1}$	33
2.14	Effect of oxygen conversion on the rate of methane conversion and C_{2+} formation at time $t=0\text{ h}$. For reaction conditions, see Table 3	35
3.1	IR spectra of CO adsorbed on C-MgO at $T=77\text{ K}$ with increasing pressure from $p=2.9\text{ Pa}$ to $p=210\text{ Pa}$. (A) Range of carbonyl and carbonite vibrations (B) Evolution of carbonyl bands as a function of the CO equilibrium pressure. Inset: Enlarged representation of carbonyl bands assigned to CO adsorbed on 3-fold coordinated Mg^{2+} cations.	51
3.2	Integrated area of the peaks of adsorbed CO as a function of the equilibrium CO pressure at 77 K (A) and the derived adsorption isotherms (B). The integrated area was determined using spectra normalized with respect to the mass of the wafer.	52

3.3	Spectra of CO adsorbed on MgO at T=77K at a coverage of $\theta = 0.15$. . .	53
3.4	High resolution TEM images of MW-MgO viewed along [100]. The inset in (A) shows a power spectrum, which allows to identify the orientation of the MgO crystal. (B) represents a higher magnified micrograph of (A) taken at the marked region of interest. The mono-atomic steps at the surface are clearly visible and marked by arrows.	54
3.5	Adsorption of ca. 10 Pa methane at T=77 K on pretreated C-MgO (red line) and after pre-adsorption of 200 Pa CO (black line).	56
3.6	(A) Adsorption of CD ₄ at T=77 K at the surface of C-MgO dehydroxylated at 1073 K. (B) Enlarged representation of the spectra in the range of O-D stretching vibrations. Black line: after adsorption of 100 Pa CD ₄ , red line: after evacuation up to $5 \cdot 10^{-4}$ Pa.	58
3.7	Integrated areas of the ν_4 mode of adsorbed CH ₄ on outgassed MgO (green bars) and on MgO that has been pre-saturated with CO ($p_{eq} = 200$ Pa, <i>i.e.</i> $\theta=1$, blue bars) at T=77K. The green bars are a measure of the total number of adsorption sites of methane (di-hapto adsorption at Mg ²⁺ - O ²⁻ acid-base pair sites at edges plus mono-hapto adsorption at basic O ²⁻ sites (corners)), the blue bars indicate the number of the basic O ²⁻ adsorption sites at corners only. The numbers presented on top of the bars indicate the relative content of acid-base pair sites for methane adsorption on the MgO surface in percentage.	59
3.8	Spectra of CO adsorbed at T=77K at $\theta=0.08$ on C-MgO after calcination (red line) and after application in oxidative coupling of methane (black line) under the following reaction conditions: CH ₄ /O ₂ /N ₂ =3/1/1, W/F=0.15 g · s · ml ⁻¹ , T= 1073 K, TOS = 300 h.	60
3.9	2D photoluminescence patterns of fresh (A) and used (B) C-MgO normalized with respect to the intensity	62
3.10	EPR spectra of C-MgO after evacuation at 1023 K in vacuum followed by (a) adsorption of and $5 \cdot 10^3$ Pa O ₂ at room temperature, and subsequent evacuation, and (b) co-adsorption of $9 \cdot 10^3$ Pa CH ₄ and $2 \cdot 10^3$ Pa O ₂ at room temperature and subsequent evacuation. The spectra are recorded at 77 K, at a pressure of about $1 \cdot 10^{-4}$ Pa	65
3.11	Rate of methane consumption and C ₂₊ formation at t=0 as a function of the relative amount of acid-base pairs (edges) on the surface of the catalysts.	69
3.12	Rate of methane consumption plotted versus the integrated area of the CO adsorption peak at 2147 cm ⁻¹ that indicates the abundance of mono-atomic steps (steps in the dimension of a unit cell).	69

4.1	a) HRTEM image showing the stepped surface of Au-Fe-MgO. b) HAADF STEM image with characteristic bright contrast at steps and edges due to decoration with heavy atoms. c) Columns of heavy atoms can also be seen in thin regions in HRTEM.	87
4.2	Yield of ethane and ethene in the oxidative coupling of methane as a function of time on stream (TOS) at T=1023 K; W/F= $0.0167 \text{ g} \cdot \text{s} \cdot \text{ml}^{-1}$, $\text{CH}_4/\text{O}_2/\text{N}_2=3/1/1$	88
4.3	a) HAADF STEM and b) TEM image with localized contrast variations due to defects caused by bulk doping as indicated by arrows. c) HRTEM image of doped MgO particles for which the lattice rotation due to strain is shown in d).	90

List of Tables

2.1	Specific surface area and domain size determined by XRD of MgO catalysts before and after use in oxidative coupling of methane.	19
2.2	Content of traces of transition metals as determined by using inductively coupled plasma-optical emission spectrometry (ICPOES).	20
2.3	Consumption rate of methane, conversions and selectivity measured over MgO catalysts in the oxidative coupling of methane in the initial state ($t=0$) at $T=1023$ K, applying a feed composition of $\text{CH}_4/\text{O}_2/\text{N}_2=3/1/1$, and a contact time of $0.033 \text{ g}\cdot\text{s}\cdot\text{ml}^{-1}$	26
2.4	Consumption rate of methane, conversions and selectivity measured over MgO catalysts in the oxidative coupling of methane in the stationary state at $T=1023$ K, applying a feed composition of $\text{CH}_4/\text{O}_2/\text{N}_2=3/1/1$, and a contact time of $0.15 \text{ g}\cdot\text{s}\cdot\text{ml}^{-1}$	26
2.5	Kinetic parameters measured over MgO catalysts in oxidative coupling of methane in the stationary state. The apparent activation energies E_a were determined based on the methane consumption rate in the temperature range $T=923\text{-}1073$ K, applying a contact time of $0.15 \text{ g}\cdot\text{s}\cdot\text{ml}^{-1}$, and a feed composition of $\text{CH}_4/\text{O}_2/\text{N}_2=3/1/1$. The reaction orders were determined at $T=1023$ K at a contact time of $0.15 \text{ g}\cdot\text{s}\cdot\text{ml}^{-1}$ and variation of the CH_4/O_2 ratio from 0.75 to 3.6 and the O_2/CH_4 ratio from 3 to 6.	29
3.1	Excitation-emission couples experimentally observed for fresh and used C-MGO in comparison with calculated components of excitation energy maxima.	64
4.1	General characteristics of the doped MgO catalysts and normalized formation rates of coupling products ethane and ethene in OCM of methane.	86

List of schemes

1.1	Simplified scheme of the OCM reaction	2
2.1	Proposed reaction mechanism of the formation of C_{2+} products in the oxidative coupling of methane over pure, freshly dehydroxylated MgO catalysts.	36
3.1	Coordination of methane and CO at the MgO surface	56
3.2	Proposed mechanism of methane activation on dehydroxylated MgO	71

List of supporting tables

3.1	Integration of the Gaussian components in arbitrary unit.	81
4.1	Hydrogen consumption in TPR (H_2 evolution during activation (negative values)).	97

List of supporting figures

2.1	SEM images of calcined MgO (left side) and MgO after oxidative coupling of methane for 300 hours time on stream ($\text{CH}_4/\text{O}_2/\text{N}_2=3/1/1$, $W/F=0.15 \text{ g}\cdot\text{s}\cdot\text{ml}^{-1}$, $T=1073 \text{ K}$). From top to bottom: S-MgO (A,B), C-MgO (C,D), SG-MgO (E,F), HT-MgO (G), and MW-MgO (H,I).	41
2.2	Conversion and selectivity for S-MgO as a function of the contact time at $T=1023 \text{ K}$, using a catalyst mass of $m_{cat}=150 \text{ mg}$, and a feed composition of $\text{CH}_4/\text{O}_2/\text{N}_2=3/1/1$	42
2.3	Conversion and selectivity for SG-MgO as a function of the contact time at $T=1023 \text{ K}$, using a catalyst mass of $m_{cat}=150 \text{ mg}$, and a feed composition of $\text{CH}_4/\text{O}_2/\text{N}_2=3/1/1$	42
2.4	Conversion and selectivity for HT-MgO as a function of the contact time at $T=1023 \text{ K}$, using a catalyst mass of $m_{cat}=150 \text{ mg}$, and a feed composition of $\text{CH}_4/\text{O}_2/\text{N}_2=3/1/1$	43
2.5	Conversion and selectivity for MW-MgO as a function of the contact time at $T=1023 \text{ K}$, using a catalyst mass of $m_{cat}=150 \text{ mg}$, and a feed composition of $\text{CH}_4/\text{O}_2/\text{N}_2=3/1/1$	43
3.1	UV-vis spectra of C-MgO catalyst measured in vacuum at 293 K after pre-treatment in vacuum at 923 K	75
3.2	2D photoluminescence of fresh S-MgO (#12817) recorded at 300 K in dynamic vacuum after activation at 1073 K in vacuum.	76
3.3	2D photoluminescence of used S-MgO (#12992) recorded at 300 K in dynamic vacuum after activation at 1073 K in vacuum.	76
3.4	2D photoluminescence of fresh SG-MgO (#12342) recorded at 300 K in dynamic vacuum after activation at 1073 K in vacuum.	77
3.5	2D photoluminescence of fresh HT-MgO (#12498) recorded at 300 K in dynamic vacuum after activation at 1073 K in vacuum.	77
3.6	Spectrum of CO adsorbed on S-MgO at $T=77 \text{ K}$ and a coverage of $\theta=0.15$. Black curve: experimental data, red curve: fitting, green curves: individual Gaussian component.	78

3.7	Spectrum of CO adsorbed on C-MgO at T=77 K and a coverage of $\theta=0.15$. Black curve: experimental data, red curve: fitting, green curves: individual Gaussian component.	79
3.8	Spectrum of CO adsorbed on SG-MgO at T=77 K and a coverage of $\theta=0.15$. Black curve: experimental data, red curve: fitting, green curves: individual Gaussian component.	79
3.9	Spectrum of CO adsorbed on MW-MgO at T=77 K and a coverage of $\theta=0.15$. Black curve: experimental data, red curve: fitting, green curves: individual Gaussian component.	80
3.10	Spectrum of CO adsorbed on HT-MgO at T=77 K and a coverage of $\theta=0.15$. Black curve: experimental data, red curve: fitting, green curves: individual Gaussian component.	80
3.11	Comparison of the fitted Gaussian component for the contribution of the 2147 cm^{-1} band for the five MgO catalysts.	81
4.1	UV-vis spectra of the doped catalysts measured in Ar at 293 K after pretreatment in Ar at 923 K.	96
4.2	EPR spectrum of Au-Fe-MgO after pretreatment at 1073 K under high vacuum, measured at 77 K, A) Experimental (black line) and simulated spectrum (red line). B) Experimental spectra of Fe^{3+} at lower magnetic field. Both spectra are measured at a frequency of 9.63637 GHz.	96
4.3	TPR-O of Fe-MgO. The blue line was measured during pretreatment in 90 $\text{mL}\cdot\text{min}^{-1}$ Ar applying a heating rate of 10 $\text{K}\cdot\text{min}^{-1}$	97
4.4	TPR-O of Au-Fe-MgO. The blue line was measured during pretreatment in 90 $\text{mL}\cdot\text{min}^{-1}$ Ar applying a heating rate of 10 $\text{K}\cdot\text{min}^{-1}$	98
4.5	Methane conversion in the oxidative coupling of methane as a function of time on stream (TOS) at T=1023 K; W/F= 0.0167 $\text{g}\cdot\text{s}\cdot\text{ml}^{-1}$; $\text{CH}_4/\text{O}_2/\text{N}_2=3/1/1$	98
4.6	Oxygen conversion in the oxidative coupling of methane as a function of time on stream (TOS) at T=1023 K; W/F= 0.0167 $\text{g}\cdot\text{s}\cdot\text{ml}^{-1}$; $\text{CH}_4/\text{O}_2/\text{N}_2=3/1/1$	99
4.7	Selectivity of the sum of ethane and ethene (C2) in the oxidative coupling of methane as a function of time on stream (TOS) at T=1023 K; W/F= 0.0167 $\text{g}\cdot\text{s}\cdot\text{ml}^{-1}$; $\text{CH}_4/\text{O}_2/\text{N}_2=3/1/1$	99
4.8	Series of HRTEM images recorded at different defocus reveal the presence of strongly scattering atoms located at the steps in the Au-Fe-MgO catalyst after catalysis.	100

1. Introduction

1.1 General introduction

Since the 1970s and the two energy crises of 1973 and 1979, new methane resources including coal bed methane and shale gas were found and exploited beside natural gas fields. [1] The increased exploitation of methane was accompanied by scientific and industrial efforts to use methane as raw material and transform it to value-added products.

Several methods were developed to convert methane into syngas ($\text{CO} + \text{H}_2$). The produced hydrogen and/or carbon monoxide are used to produce, for example, methanol, ammonia, or higher alkanes and alcohols (through Fischer-Tropsch synthesis). Other indirect ways include reactions like steam reforming ($\text{CH}_4 + \text{H}_2\text{O}$), dry reforming ($\text{CH}_4 + \text{CO}_2$) or partial oxidation ($\text{CH}_4 + \text{O}_2$).

Except for synthesis of hydrogen cyanide and chloroform, the direct transformation of methane to more valuable products is more challenging and nowadays still in the stage of research and development. These transformations include direct methanol synthesis, non-oxidative coupling of methane to aromatics and oxidative coupling of methane (OCM) to ethane and ethylene.

The oxidative coupling of methane was first proposed by Keller and Bhasin [2] in 1982 followed by the work of Hinsien and Baerns in 1983 [3] and the group of Lunsford in 1985. [4–6] These pioneering works disclosed the perspective to produce ethylene from methane instead from crude oil through steam cracking.

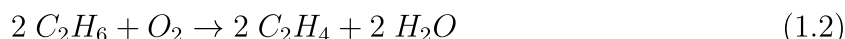
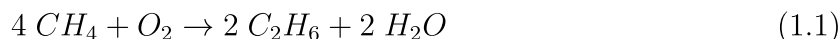
Ethylene is a bulk chemical produced on a large scale (ca. 130 mty worldwide). It is an essential reactant in the production of polymers. Furthermore, ethylene is used in the production of ethylene oxide, acetaldehyde, vinyl chloride, ethylene dichloride, styrene, ethyl benzene, ethanol and propionaldehyde, which are all important basic chemicals in the chemical industry.

More than 30 years after the pioneering works of Keller and Bhasin no significant progress was achieved. The yield of 30 % C_2 products (i.e. ethylene and ethane) in a single pass methane conversion was not surpassed so far. Higher yields are, however, required for a viable economical process.

1.2 Reaction mechanism

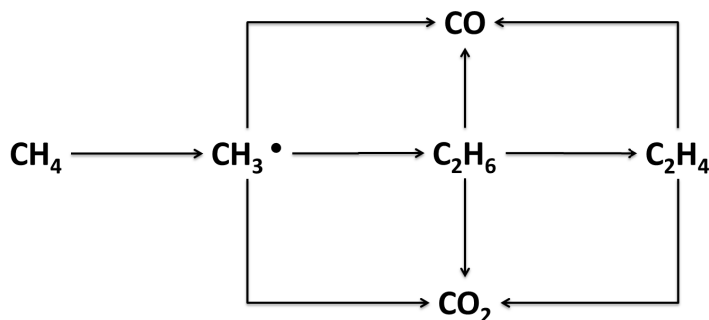
The scientific community widely agrees in an over-simplified view that the selective formation of ethylene from methane occurs via three main steps: (i) the activation of methane leading to the formation of methyl radicals through C-H bond breaking by hydrogen abstraction, (ii) the homogeneous coupling of two methyl radicals to ethane in the gas phase and (iii) the oxidative dehydrogenation of ethane (ODE) to ethylene. Non-selective (homogeneous and/or heterogeneous) oxidative reactions may happen at each step resulting in deeper oxidation and finally the formation of carbon oxides (COx) (see Scheme 1.1)

According to the simple reaction network outlined above, the oxidative coupling of methane has been generally written as:



More detailed mechanisms are still under debate in the literature. The situation is complex due to the harsh condition at which the reaction takes place and the large variety of different types of catalyst that have been included into the research: reducible oxides, non-reducible oxides, halogen containing oxides, solid electrolytes, supported liquid phase catalysts; doped or undoped oxides. Despite their very different chemistry, all these materials show catalytic activity in the OCM reaction. [7–9]

Recently, Zavyalova *et al.* [8] performed a comprehensive statistical analysis of OCM cat-



Scheme 1.1: Simplified scheme of the OCM reaction (adapted from [7])

alysts including 1000 publications. Accordingly, 68 different elements were used for the preparation of hundreds of different catalysts over the last 30 years. Many of them are binary or ternary oxides. Already in their first publication, Keller and Bhasin [2] reported that 7 different monophasic oxides (Mn, Cd, Sn, Sb, Tl, Pb and Bi) were active in the

OCM reaction while 5 others (Li, Mg, Cr, Co and B) showed little activity. Basic oxides, like alkaline earth oxides, belong to a very important class of catalysts studied in OCM. Some general criteria have been developed for designing an active and selective catalyst. [9] On the one hand, the catalyst must facilitate the abstraction of one hydrogen atom from methane to form methyl radicals, which is enabled by a high capability for the interaction with oxygen. On the other hand, the catalyst should minimize the deep oxidation of methyl species and reduce nonselective reactions between oxygen-containing intermediates and C_{2+} hydrocarbons.

Since gas phase reactions play an important role in the mechanism of catalyzed OCM reaction, work on non-catalytic gas phase OCM is of special interest in order to understand the part played by homogeneous reactions. A recent study combining in situ characterization of formaldehyde formed as intermediate, gas phase kinetic measurements, and modelling under industrial relevant reaction conditions, emphasizes that methyl radical coupling in the gas phase to C_2 products is indeed possible, however, it is by far not the main route for CH_3^\bullet consumption. [10]

A rational development of an active and selective catalyst for OCM failed so far due to complex relations between heterogeneous and homogeneous reaction networks. In this context, engineering considerations represent essential aspects in catalyst development and testing. Comprehensive approaches that include reaction engineering are of importance to fully understand the catalytic process. [11]

1.3 Technical aspects

Due to the complexity of the reaction mechanism, i.e. homogeneous/heterogeneous reaction, reactor selection is essential in order to suppress non-selective reactions and enhance the yield of C_{2+} products. The most challenging features are oxygen feed distribution and heat removal. [11] Therefore, reaction conditions have to be chosen carefully in order to eliminate transport phenomena and ensure an accurate kinetic measurement. For instance, in a fixed bed reactor, external mass transport limitations lead to an increase in C_{2+} selectivity due to a lower partial pressure of oxygen. In contrast, in case of intra-particle mass transport limitations the selectivity due to consecutive reactions is generally decreased. However, at the same time, an increase in the C_2H_4/C_2H_6 ratio was reported. [11,12]

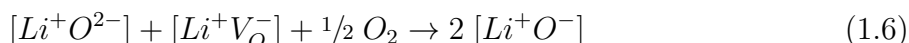
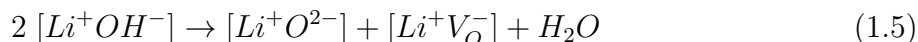
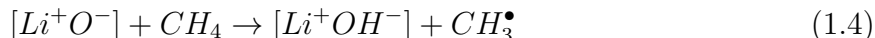
Consequently, some practical aspects have to be considered when using a fixed-bed reactor for OCM kinetic measurements. It is especially important to reduce the voids before and after the catalytic bed in order to reduce the participation of gas phase chemistry. [12]

1.4 Methane activation

The interaction of activated oxygen species on the catalyst surface with weakly adsorbed or gas-phase methane molecules can directly result in homolytic formation of methyl radicals, while methane activation via basic surface oxygen follows a heterolytic cleavage after which the removal of an electron from CH_3^- species is required to generate methyl radicals. In addition, electrophilic oxygen species are involved in the nonselective oxidation of methyl radicals and C_2 -hydrocarbons.

Kinetic isotope effect (KIE) studies suggested the involvement of a C-H bond scission in the rate-determining step over Li/MgO as catalyst. [13] However, it has also been observed that the KIE decreases with increasing methane to oxygen ratio, which indicates that a single rate-determining step does not exist when oxygen is used as oxidizing agent. [14] However, the contributions of homogeneous and heterogeneous reaction steps that follow the formation of the methyl radical and that determine the selectivity of the reaction are less clear. [15,16]

The detection of matrix-isolated methyl and methyl peroxy radicals by EPR spectroscopy suggested that methane is activated through C-H dissociation and formation of methyl radicals. [4] The same authors found some indications for the presence of $[\text{Li}^+\text{O}^-]$ in Li/MgO catalysts and V^- centers in pure MgO catalysts. Based on these two findings they proposed a mechanism for methane activation based on an Eley-Rideal-type reaction mechanism for Li/MgO [4]:

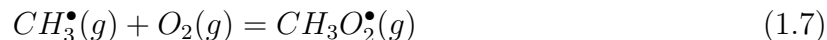


Heterogeneous C-H bond breaking on basic surface sites was also proposed. [17–19]. Accordingly, methane is adsorbed on the surface of a basic catalyst and after dissociation of the C-H bond, CH_3^- and H^+ ions are formed. In the presence of molecular oxygen, an intermolecular electron transfer occurs between CH_3^- and oxygen to form CH_3^\bullet and O_2^- .

Molecular hydrogen that has almost the same bond strength as methane can undergo a similar reaction. Indeed, Knözinger *et al.* reported that H_2 is splitted either homogeneously or heterogeneously on the surface of pure MgO. [20]

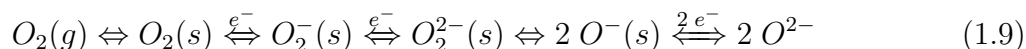
Although methane can already be activated at lower temperatures by adsorbed oxygen species, the selective OCM reaction generally proceeds only at temperatures above ca. 900 K. The intrinsic requirement of such high temperatures for the OCM reaction is still not fully understood. High reaction temperature may favor the desorption of methyl species from the surface to the gas phase, which may reduce the further oxidation of methyl species by surface oxygen species. High reaction temperature may also favor the decomposition of the methyl peroxy radical ($\text{CH}_3\text{O}_2^\bullet$) in the gas phase, reducing nonselective gas-phase

reactions. [9]



1.5 Oxygen activation

Depending on oxygen partial pressure, temperature, and the ability of the metal oxide to transform weakly adsorbed oxygen entities into lattice oxygen, the following oxygen species might exist in an equilibrium state. [9]



A high surface concentration of oxygen anion vacancies favors oxygen adsorption and transformation into less electrophilic species (O^- , O^{2-}). Baerns *et al.* [9] emphasized the fact that the electrical conductivity of the metal oxide controls the type of adsorbed species on the surface. They found out that both the p-type conductivity and the oxygen-ion conductivity are favorable for the selectivity towards C_{2+} in the OCM reaction [9]. They concluded that an ideal OCM catalyst should possess a high capacity of transforming oxygen species into lattice oxygen (i. e. nucleophilic species) and only provide the surface with active oxygen species (e. g. O^- or O_{LC}^{2-} (lattice oxygen in low coordination)) in such a concentration that molecular methane can be efficiently activated while the surface non-selective reactions are minimized. Dubois and Cameron came to a similar conclusion: a good OCM catalyst is a strong basic oxide that exhibit a p-type conductivity and oxygen mobility at reaction temperature. [21]

Buyevskaya *et al.* [22] and Peil *et al.* [23] studied the oxygen diffusion in OCM catalysts by oxygen isotope exchange. The activation energy for oxygen diffusion in MgO is very high (260-270 kJ/mol). It should be mentioned that the high concentration of oxygen vacancies facilitate the conversion of adsorbed oxygen into lattice oxygen, particularly at high temperature. [24]

The dissolution of excess O_2 in non-transition metal oxides such as MgO leads to the formation of positive holes h^\bullet , chemically O^- , which tend to undergo spin pairing:



The peroxy anions thus formed and mostly associated with cation vacancies are thermally stable up to about 800-900 K. Above this temperature they release unbound positive holes, which interact with transition metal impurities, for instance Fe^{2+} , leading to their oxidation. [25]

O^- may also be formed under equilibrium conditions on MgO together with the formation of cation vacancies.

$$\frac{1}{2} O_2 = V''_{Mg} + O^x + 2 O^- \quad (1.11)$$

Concerning the formation of O^- it is also important to note that surface O_2^- ions have the tendency to reduce their effective charge due to the decrease in electrostatic energy compared to the bulk oxygen. [6]

$$O^{2-} = O^- + e^- \quad (1.12)$$

It has also been suggested by Boudart *et al.* that thermal activation of MgO without any irradiation can generate O^- ions. [26] Martens *et al.* [27], followed the formation of O^- ions indirectly by measuring the hydrogen and oxygen release during the thermal decomposition of $Mg(OH)_2$ to form the oxide. They suggested that O^- ions are formed in the bulk or on the surface by a process such as shown in equation (1.11).

$$OH^- \cdots OH^- = 2 O^- + H_2 \quad (1.13)$$

EPR spectroscopy is the most common method used to characterize paramagnetic adsorbed oxygen on the catalyst surface and the formation of point defects, like color centers. Recently, Zhang *et al.* have demonstrated that in situ Raman spectroscopy can be suitable to observe adsorbed oxygen species namely O_2^- and O_2^{2-} under OCM condition. [28] Other in situ analytical methods can also be relevant for the study of point defects, like electrical conductivity measurement, or UV-Vis spectroscopy. Knözinger *et al.*, [29] have characterized color centers on the surface of MgO by means of UV-Vis diffuse reflectance spectroscopy.

1.6 MgO as model catalyst: synthesis and reactivity

Since Lunsford *et al.* reported in 1985 about lithium-doped magnesium oxide (Li/MgO) as a suitable and effective catalyst for the OCM reaction, [5] this system has been considered as a benchmark. In Li/MgO, $[Li^+O^-]$ species have been suggested by Lunsford *et al.* to be the active sites responsible for the conversion of methane. [4] However, several uncertainties and drawbacks are connected with the Li/MgO catalyst:

- Only indirect experimental proof of the presence of $[Li^+O^-]$ species under conditions not relevant for OCM;
- Li/MgO catalysts contain always metal ion impurities [30] like Mn^{2+} , Mn^{4+} , Fe^{3+} , and Cr^{3+} , which might also be potential active sites for methane oxidation;

- Lithium loss at the reaction temperature (800 C), leading to a deactivation of the catalysts. [31–34]

Recently Zavyalova *et al.* have demonstrated that lithium in Li-doped MgO acts as a promoter and change the morphology of the primary particle of the MgO catalysts. [32–34] Klabunde *et al.* have shown that it is possible to vary significantly the shape of the primary particles of MgO from nano-polyhedrons to cubic microcrystals by using suitable synthesis methods. [35] They applied a sol-gel method to synthesize polyhedral particles of 4 nm size with a cubic internal structure and stabilized high index crystal planes, in particular (111) planes. Due to the high surface area ($250\text{--}500\text{ m}^2 \cdot \text{g}^{-1}$), the abundance of edge and corner sites in these materials is high. [36] Hexagonal micro crystals are obtained from hydrothermal post treatment (HTPT) of MgO. [35] Hexagonal plates expose mainly (100) and (110) planes. These materials have a lower surface area (about $150\text{ m}^2 \cdot \text{g}^{-1}$). Almost ideal cubic primary particle are obtained by burning Mg in static atmosphere. The resulting magnesium oxide is called smoke MgO. [37] The particles have a size of about 100 nm. The surface area is about $10\text{ m}^2 \cdot \text{g}^{-1}$. Knzinger *et al.* [20] developed a chemical vapor deposition (CVD) technique to produce nano-cube particles of 10 nm that result in high surface area of $300\text{ m}^2 \cdot \text{g}^{-1}$. It is considered that the hydrogen abstraction from methane occurs on $[\text{Li}^+\text{O}^-]$ species present in Li/MgO. Ito *et al.* have proven with TPD and EPR experiments that low coordinated (LC) ions are present on the MgO surface on terraces (L=5), edges (L=4) and corners / kinks (L=3) (see Fig. 2). Especially low-coordinated anions $\text{O}_{\text{LC}}^{2-}$ could be responsible for the heterolytic hydrogen cleavage of a hydrogen-carbon bond in methane even at room temperature with the following reactivity: $\text{O}_{3\text{C}}^{2-} > \text{O}_{4\text{C}}^{2-} >> \text{O}_{5\text{C}}^{2-}$. [38] In addition, it was shown that under thermal or UV irradiation, $\text{O}_{\text{LC}}^{2-}$ ions form electron deficient oxygen anions O_{LC}^- , which can split the C-H bond in methane homolytically to form methyl radicals. [39] Hargreaves *et al.* have studied the structure sensitivity of MgO in the OCM reaction [40] and the isotopic exchange of oxygen with the MgO surface by investigating differently prepared catalysts. [41] Two catalysts with the same primary particles shape but with different surface area have been compared. The two magnesium oxides exposed largely $\{001\}$ planes. One of the catalysts had, due to its smaller cube length, a higher number of atoms situated on edges and corners. Since the selectivity and specific activity were the same, it has been concluded that these sites, *i. e.*, low coordinated ions on edges and corners, do not play a significant role in the OCM reaction on MgO. The most selective MgO is characterized by a greater proportion of higher index crystal planes, *e. g.*, $\{111\}$ surfaces. Lunsford *et al.* confirmed that the addition of lithium changes the morphology of the MgO primary particles but that this change has no effect on the reactivity of the OCM reaction. [42]

1.7 Characterization of the surface properties of MgO

Traditional methods of the synthesis of MgO involve heating of $\text{Mg}(\text{OH})_2$, which is composed of a layered brucite structure, or the decomposition of various magnesium salts. Spoto *et al.* reviewed the formation and sintering of MgO particles by treatment of $\text{Mg}(\text{OH})_2$ in vacuum at high temperature. [43] The $\text{Mg}(\text{OH})_2$ decomposes under vacuum with formation of layers of nano-cubes. These cubes are aligned along the (111) direction. They cannot be considered as separate particles because they appear to be connected continuously across the (100) faces. A consequence of this morphology is that the typical sites characteristic of individual cubic nano-crystals (corners, edges and faces) are not the only morphological properties of this material. Steps and inverse sites of variable height formed by the intersection of (100) terraces are very abundant. It is noteworthy that inverse corners and edges are particular features derived from the partial retention of the long range order in the $\text{Mg}(\text{OH})_2$ layered structure.

Garrone *et al.* [44] have characterized the nature of low-coordinated ions on the surface of alkaline earth oxides by UV-Vis spectroscopy. They compared the observed energies of optical transitions with theoretical models, in particularly the Levine-Mark theory and assigned the absorption to oxygen atoms on edges and corners on the (100) plane rather than higher index planes. Che *et al.* have recorded photoluminescence (PL) spectra of MgO. [45] By varying the primary particle size and shape, the concentration of LC ions on edge and corners was varied. Che *et al.* have developed a method to quantify the ratio of 3-fold coordinated to 4-fold coordinated ions on the MgO surface [46].

LC ions are expected to influence the acid-base properties of MgO catalysts. [47] Baerns *et al.* [48] described different methods to characterize basic sites, which are supposed to be involved in the heterolytic C-H bond splitting in the OCM reaction. [7] Infrared spectroscopy of probe molecules is a powerful technique in order to characterize and quantify LC ions. In a review, Spoto *et al.* resumed thoroughly infrared spectroscopy of adsorbed CO on the surface of MgO. [43]

Goodman *et al.* have claimed that $[\text{Li}^+\text{O}^-]$ in Li/MgO centers are not likely to be directly involved in the methane activation step, but rather promote the production of color centers, *i. e.*, anion vacancies filled by one (F^+) or two electrons (F^0), in the near surface region, which are responsible for this key step in the methane coupling reaction. [49]

Gai *et al.* [50] have demonstrated by in situ TEM, that the calcination of $\text{Mg}(\text{OH})_2$ to MgO under high vacuum lead to the formation of anion vacancies along the (111) direction and to the formation of extended structural defects. This paper shows that the concentration of anion vacancies increases when the calcination temperature increases. At the same time, the strength of the basic sites on the surface of the oxide increases.

Paganini *et al.* [51] have shown that full dehydration of $\text{Mg}(\text{OH})_2$ leads to the formation of anion vacancies preferentially at low coordinated anions ($\text{L}=4$ and $\text{L}=3$) present on

structural defects (steps, edges, corners and kinks). In this way, polar (111) micro-facets (or inverse corners) stabilized by three Mg^{2+} ions, are formed. These anion vacancies can dissociate H_2 . Irradiation of magnesium oxide by UV light in presence of adsorbed H_2 leads to the formation of color centers $\text{F}_s^+(\text{H})$. The adsorption of O_2 on anion vacancies or $\text{F}_s^+(\text{H})$ color centers in presence of adsorbed H_2 leads to the formation of superoxide O_2^- species adsorbed on the MgO surface near to the vacancy. Superoxides seem to have an important role in the OCM reaction as emphasized by Baerns *et al.* [9] Osada *et al.* found a positive correlation between the intensity of the O_2^- signal (measured by EPR spectroscopy) and the C_{2+} selectivity. They believe that O_2^- ions belong to the active site on the surface of the catalyst. [52]

1.8 Doping theory

The electronic properties of a catalyst can be modified by doping. Two types of dopants should be distinguished: acceptors, which act as trap for free electrons (n-type conductivity), and donors who can trap free holes (p-type conductivity). For instance, in the case of substitutional solutions, the dopants with lower valance act as acceptors, while with higher valance they act as donors. For the OCM reaction, an acceptor type dopant is usually required for improving the catalytic performance, *i.e.*, acceptance of an electron from methane to form a methyl radical. [9] At the same time, the electronic properties of the catalyst control the activation of molecular oxygen. [53] Recently Cui *et al.* developed the concept of homogeneous electronic doping. Mo^{2+} ions in the bulk of a CaO single crystal were able to donate electrons to the surface of the wide band gap catalyst and activate molecular oxygen to form superoxide on the defect free surface. [54]

1.9 Motivation and aim of the thesis

The analysis of the literature concerning the reaction mechanism of the oxidative coupling of methane, the function of the catalyst, and the nature of the active sites presented above has shown that the general picture is still not clear. One issue in this respect is the impact of structural defects on the surface of alkaline earth oxides on their catalytic properties in OCM that has been discussed controversially. The aim of this thesis is, therefore, to gain knowledge about the structure sensitivity of methane activation over alkaline earth oxide. This work focuses in particular on the influence of the morphology of the primary catalyst particles on the oxidative coupling of methane over MgO model catalysts. Pure MgO was selected as a model catalyst, since this system has been investigated in modified form since more than 20 years and considerable knowledge already exists. The morphology of the

catalyst particles was varied by varying the preparation technique. Relations between the nature and abundance of morphological surface defects such as steps and corners on the reactivity of pure magnesium oxide in the oxidative coupling of methane are addressed. A mechanism for methane activation is proposed based on kinetic and spectroscopic results.

1.10 Outline of the thesis

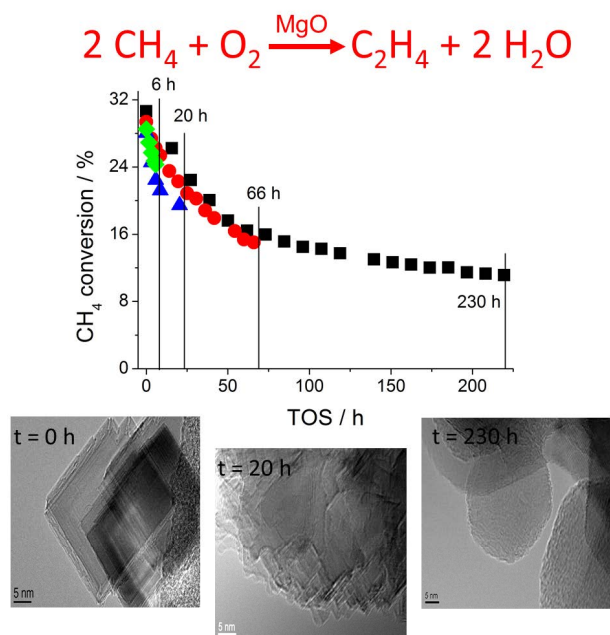
Chapter 2: The synthesis and general characterization of five morphologically different pure magnesium oxides is presented. Based on a comprehensive kinetic study a new reaction mechanism that dominates in the initial state of the reaction over the dehydroxylated catalysts is proposed. Under these conditions, MgO is highly active. Kinetic parameters of deactivated MgO in the stationary state are determined and discussed.

Chapter 3: The active sites, which are responsible for this high activity in the initial state are determined by infrared and photoluminescence spectroscopy. Quantitative correlations between the abundance of the active sites and the rates of methane consumption and product formation are established. Reaction intermediates have been observed by infrared and EPR spectroscopy that support the reaction mechanism proposed in Chapter 2.

Chapter 4: Based on the results obtained in Chapter 2 and 3, we developed a strategy to stabilize and enhance the performance of magnesium oxide in the OCM reaction. For this purpose electronic doping effect was investigated. Such an electronic doping does not require any surface structural defects. MgO was co-doped with Fe and Au in ppm quantities with the aim to obtain a homogeneous catalyst micro-structure. The concept provides a promising approach to activate and stabilize OCM catalysts.

2. Structure sensitivity of the oxidative activation of methane over MgO model catalysts: I. Kinetic study ¹

Pierre Schwach, Wiebke Frandsen, Marc-Georg Willinger, Robert Schlögl, Annette Trunschke



Abstract The role of surface structure and defects in the oxidative coupling of methane (OCM) was studied over magnesium oxide as a model catalyst. Pure MgO nano-particles with varying primary particle size, shape and specific surface area were prepared by sol-gel synthesis, oxidation of metallic magnesium, hydrothermal post treatment of ultra-pure MgO at normal pressure and under pressure in a microwave autoclave. Bulk and microstructure of the catalysts were analyzed by electron microscopy, X-ray diffraction, and nitrogen adsorption. The initial activity of MgO in the OCM reaction is clearly structure-sensitive. Kinetic studies reveal the occurrence of two parallel reaction mechanisms and a change in the contribution of these pathways to the overall performance of the

¹The following chapter is adapted from [55]

catalysts with time on stream. The initial performance of freshly calcined MgO is governed by a surface-mediated coupling mechanism involving direct electron transfer between methane and oxygen. The two molecules are weakly adsorbed at structural defects (mono-atomic steps) on the surface of MgO. The proposed mechanism is consistent with high methane conversion, a correlation between methane and oxygen consumption rates, and high C₂H₄ selectivity after short times on stream. The water formed in OCM reaction causes sintering of the MgO particles and loss of active sites by degradation of structural defects, which is reflected in decreasing activity of MgO with time on stream. At the same time, gas phase chemistry becomes more important, which includes formation of ethane by coupling of methyl radicals formed at the surface and the pyrolysis of C₂H₆. The mechanistic concepts of the work presented in this work (Part I) will be substantiated in Part II by spectroscopic characterization of the catalysts. [56]

Keywords: MgO; oxidative coupling; methane; ethane; ethylene; defects; reaction mechanism.

Acknowledgement The authors thank Gisela Lorenz and Pia Kjaer Nielsen for their help with the surface area measurements, Dr. Frank Girgsdies and Edith Kitzelmann for performing the XRD analysis, and Iris Pieper at the Technical University Berlin for chemical analysis. This work was conducted in the framework of the COE UniCat (www.unicat.tu-berlin.de) of the German Science Foundation.

2.1 Introduction

Activation of methane over heterogeneous catalysts remains an attractive subject in view of the abundance of natural gas and renewable methane resources. The scientific interest in oxidative coupling of methane (OCM) to ethane, ethylene, and higher hydrocarbons (C₂₊ products), however, went down noticeably during the past years. One reason might be that in spite of numerous attempts using chemically very different catalysts, C₂₊ yields of about 30 % have not been significantly surpassed so far. In addition, the diversity of known active catalyst masses complicates the identification of a general functional model. [8] The not yet fully resolved relationship between surface and gas phase chemistry of CH₄ at the high reaction temperatures inspired us to deal with fundamental questions of methane activation on the surface of heterogeneous catalysts in a systematic approach addressing in particular the function of surface defects using magnesium oxide as a model catalyst.

Li-doped MgO was discovered by Lunsford et *al.* as an active catalyst in the oxidative coupling of methane using molecular oxygen 28 years ago. [5] The originally proposed reaction mechanism involves the activation of gas-phase O_2 on either intrinsic cationic vacancies on the surface of Li-free MgO or on substitutional Li^+ ions under formation of O^- or $[Li^+O^-]$ centers, respectively, [4, 5] which can abstract a hydrogen atom from methane. The resulting methyl radical is released to the gas phase to undergo selective coupling to ethane. According to this reaction mechanism, the selectivity could be to a large extent governed by consecutive reactions, since methyl radicals may not exclusively collide with themselves. By reaction with gas phase oxygen or with O_2^- ions on the catalyst surface, $CH_3O_2^\bullet$ radicals or surface methoxy species CH_3O^- can be formed, respectively, which are considered as intermediates in the undesired formation of CO_2 that limits the C_{2+} yield. The mechanism, which has been proposed by Lunsford et *al.* for MgO and Li-MgO, has been adopted meanwhile also for chemically very different catalysts. [7]

The outstanding activity of Li-MgO compared to pure MgO in methane activation has been explicitly attributed to the presences of the specific $[Li^+O^-]$ - centers. [42] However, lithium causes sintering of magnesium oxide at the high reaction temperatures. [42] A clear impact of the varying morphology of MgO, which changes in the course of the sintering process, on undesired secondary surface reactions of re-adsorbed methyl radicals was not observed. [42] Recently, it was shown that lithium, which completely desorbs by formation of volatile compounds during the oxidative pretreatment of the catalyst (which involves the loss of all $[Li^+O^-]$ - centers), acts as a structural promoter that favors the formation of terminating higher index planes like $\{111\}$ or $\{110\}$. [32, 34] The highest selectivity to C_{2+} products was found for pure MgO catalysts, which expose a greater fraction of $\{111\}$ planes, [57] indicating in contradiction to the observations made by Lunsford et *al.* a structure sensitivity of the reaction.

Inconsistent findings have also been reported with respect to activity. From studies of magnesium oxide catalysts, which show similar morphology, but different cube size, it was concluded that edge and corner sites are not relevant for catalysis under steady state conditions. [57] However, Ito et *al.* reported that low coordinated ions on the surface of MgO play an important role in the dissociation of adsorbed methane. [58]

Defects will definitely fulfill a key function with respect to the activation of either methane or oxygen by changing the electronic structure of the wide band gap magnesium oxide particularly with regard to facilitate the transfer of electrons between the solid surface and the adsorbed molecules, which undergo a redox reaction. [59–62]

The present work addresses relations between the nature and abundance of morphological

surface defects such as steps and corners on pure magnesium oxide and its reactivity in the oxidative coupling of methane. Various synthetic techniques have been applied to prepare nano-structured MgO catalysts with different morphology. In part I of this work, we will report about synthesis, microstructural, and kinetic analysis of the morphologically different MgO catalysts. Part II deals with the spectroscopic investigation of the electronic structure and the coordinatively unsaturated surface sites of MgO. We propose a reaction path for the activation of methane on freshly activated MgO that is confirmed by the detection of reaction intermediates using ESR spectroscopy. The observed fast deactivation of magnesium oxide is interpreted in terms of a change from a concerted reaction that involves co-adsorption of methane and oxygen on monoatomic step sites to a sequential reaction in which methane and oxygen are activated independently. The latter scenario dominates in the stationary state.

2.2 Experimental

2.2.1 Starting materials

Magnesium chips (99.98 %, Sigma Aldrich), magnesium oxide (Puratronic®, 99.99 %, Alfa Aesar), methanol (ROTIPURAN®, ≥ 99.9 %, p.a., ROTH), and toluene (ROTIPURAN®, ≥ 99.9 %, p.a., ROTH) were used as received. Ultrapure water was obtained by using the Milli-Q Synthesis System (MQ). All gases for the catalytic reaction were purchased at Westfalen AG. The purity of nitrogen, argon, and oxygen was 99.999 %, the purity of hydrocarbons was 99.95 %.

2.2.2 Catalyst synthesis

Magnesium oxide was prepared applying various dry and wet methods starting with metallic Mg or MgO. Purchased MgO (C-MgO) is used as reference and raw material for surface modification.

By oxidation of Mg in air, the so-called “smoke” (S) magnesium oxide (S-MgO) was obtained. The generated oxide particles were collected using a glass funnel.

Starting from metallic Mg, but following a sol-gel (SG) procedure, [63] SG-MgO was prepared by dissolving 7 g Mg in 300 mL methanol under argon and stirring at $T=273$ K. The resulting solution of $\text{Mg}(\text{OCH}_3)_2$ was diluted with 1 liter toluene and hydrolysis was initiated by adding 11 g water (0.61 mol, 2 eq) drop-wise under stirring at the same temperature. The solution was aged for 12 h at $T=295$ K until a gel was formed. A fraction of

180 mL of the gel was then placed in a Teflon-lined 300 mL autoclave (Parr GmbH). The autoclave was first purged and then pressurized to 7 bar with N_2 . Subsequently, the gel was heated in the closed autoclave to 538 K applying a heating rate of 1 K/min. After 3 hours the pressure achieved 70 bar. The system was allowed to equilibrate at 538 K for 10 min. Then, the heater was switched off and the pressure was released within 1 min. The obtained $Mg(OH)_2$ aerogel was further dried in air at 393 K for 12 h.

Purchased magnesium oxide (C-MgO) was modified by hydrothermal treatment (HT) in water at normal pressure. For this purpose, 5 grams of C-MgO were treated in 500 mL of distilled water at $T=373$ K under reflux for 16 h. After cooling to room temperature, the suspension was filtered and washed with distilled water. The powder was dried at 393 K for 12 h giving the precursor of HT-MgO.

Hydrothermal treatment of C-MgO was also performed under pressure using microwave (MW) heating. Two Teflon autoclaves with a volume of 80 mL were filled each with 5 grams of C-MgO suspended in 60 mL of distilled water and heated to 483 K for 3 hours in a microwave (Speedwave MWS-3+, Berghof Products + Instruments GmbH). The resulting suspension was filtered and washed with distilled water. The obtained material was dried at 393 K in air for 12 h yielding the precursor of MW-MgO.

All synthesis techniques result in $Mg(OH)_2$ or $MgO-Mg(OH)_2$ phase mixtures which were transformed into the oxide by calcination in a O_2/Ar (20/80) atmosphere applying a flow of 150 mL/min. The precursor (3 g) was placed into a ceramic crucible, which was positioned into of a quartz tube. The calcination was performed at 1123 K ($3\text{ K}\cdot\text{min}^{-1}$) for 6 hours. The resulting catalysts were stored under argon and freshly pre-treated before analysis or catalysis as described in the following sections.

2.2.3 Nitrogen adsorption

The surface area determination was carried out in a volumetric N_2 physisorption set-up (Autosorb-6-B, Quantachrome) at the temperature of liquid nitrogen. The sample was degassed in dynamic vacuum at a temperature of 473 K for 2 h prior to adsorption. Full adsorption and desorption isotherms were measured. The linear range of the adsorption isotherm ($p/p_0=0.050.3$) was considered to calculate the specific surface area according to the BET method.

2.2.4 X-ray diffraction

The X-ray diffraction (XRD) measurements were performed in Bragg-Brentano reflection geometry on a Bruker AXS D8 Advance theta/theta diffractometer equipped with a secondary graphite monochromator (Cu $K_{\alpha 1}$ radiation, $\lambda=1.5406$ Å) and scintillation detector. The sample powder was filled into the recess of a cup-shaped sample holder, the surface of the powder bed being flushed with the sample holder edge. Diffraction patterns were recorded in the range $20-90^\circ 2\theta$ with a step size of 0.02° and an accumulation time of 15 s/step. The XRD data were analyzed by full pattern fitting using the TOPAS software (version 3, copyright 1999, 200 Bruker AXS).

2.2.5 Elemental analysis

Metal impurities were analyzed by inductively coupled plasmaoptical emission spectrometry (ICP-OES) using a ICP-OES 6000 Series spectrometer (Thermo). The samples were dissolved in 10 mL of 66 % HNO_3 for 6 hours at 458 K.

2.2.6 Electron microscopy

Transmission electron microscopy (TEM) was performed using a Philips CM 200 instrument. The microscope is equipped with a field emission gun and was operated at 200kV. Samples for TEM were prepared in a dry way, i.e. without dispersing the particles in a solvent. Instead, the copper TEM grids were simply dipped into the respective powder. This method is simple and prevents alteration or contamination of the sample. After tapping off excessive material, enough particles generally remain attached to the holey carbon support film of the grid for TEM investigation. Morphological studies at medium resolution were performed in a Hitachi S4500 field emission scanning electron microscope

2.2.7 Oxidative coupling of methane

The catalytic measurements were carried out in a laboratory fixed bed reaction system designed to investigate partial oxidation of hydrocarbons. The reactor consists of a quartz U-tube (4 mm inner diameter, 6 mm outer diameter, 26 cm length). The inner diameter of the tube downstream the catalyst bed is reduced to 1 mm in order to minimize the influence of gas phase reactions. The reactor is heated using a tube furnace (Carbolite®). An axial K-Type thermocouple inserted in a ceramic jacket was placed just above the catalyst bed for measurement of input gas temperature. To avoid condensation of products

(e.g. water) the reactors, part of the gas delivery system and the gas sampling system are placed in a heating cabinet that is usually kept at 353 K. N₂, O₂, hydrocarbons, and any other gases of interest are mixed outside of the heating cabinet via mass flow controllers (EL-FLOW, Bronkhorst).

Gas analysis is performed online by gas chromatography (gas chromatograph 6890A, Agilent) equipped with two channels. A combination of two capillary columns (GS-Carbonplot (length 30 m, 0.53 mm inner diameter, 40 μ m film thickness), and Plot Mole Sieve 5A (length 30 m, 0.53 mm inner diameter, 25 μ m film thickness)) in connection with a thermal conductivity detector (TCD) is used to analyze the permanent gases CO₂, O₂, N₂, and CO. A combination of two capillary columns (HP-FFAP (length 30 m, 0.53 mm inner diameter, 1 μ m film thickness), and HP Plot Q (length 30 m, 0.53 mm inner diameter, 40 μ m film thickness)) connected to a flame ionization detector (FID) is used to analyze alkanes, olefins, and oxygenates (*e.g.* CH₄, C₂H₆, C₂H₄, C₃H₈, and C₃H₆).

The catalytic experiments were carried out in such a way that the common criteria for a plug flow model were respected, i.e.: $\frac{L}{d_p} > 50$, $\frac{d_r}{d_p} > 10$, $\frac{L}{d_r} > 5$ with L being the length of the catalytic bed, d_r the diameter of the reactor (4 mm) and d_p the diameter of the catalyst particles (0.3-0.2 mm).

Considering the mass balance, the following expression was used to determine the rate of the reaction with respect to the substrate or product i at steady state:

$$\frac{dx_i}{d\left(\frac{W}{F^0}\right)} = -v_i r_i \quad (2.1)$$

Nitrogen was used as internal standard to account for volume effects due to the high temperature, at which the reaction is performed, on the gas phase analysis.

The conversion of oxygen was calculated as follows:

$$X_{O_2} = \frac{\frac{c_{O_2,in}}{c_{N_2,in}} - \frac{c_{O_2,out}}{c_{N_2,out}}}{\frac{c_{O_2,out}}{c_{N_2,out}}} \quad (2.2)$$

The conversion of methane was calculated based on the sum of products:

$$X_{CH_4} = \frac{\sum \left(\frac{n_{carbon-atoms,i}}{n_{carbon-atoms,CH_4}} c_{i,out} \right) - c_{CH_4}}{\sum \left(\frac{n_{carbon-atoms,i}}{n_{carbon-atoms,CH_4}} c_{i,out} \right)} \quad (2.3)$$

Selectivity was calculated including the number of carbon atoms, rather than stoichiometric

coefficients, and the sum of products found:

$$S_i = \frac{\frac{n_{carbon-atoms,i}}{n_{carbon-atoms,CH_4}} C_{i,out}}{\sum \left(\frac{n_{carbon-atoms,i}}{n_{carbon-atoms,CH_4}} C_{i,out} \right)} \quad (2.4)$$

The mass balance of carbon was acceptable (100 ± 1.5 %) indicating that species containing more than 4 carbons or oxygenated species were formed only in negligible quantities. The absence of transport limitations was verified by dimensionless criteria based on the film diffusion model, [64] using the approximations that (i) the pellets are ideal spheres, (ii) the molecular diffusivity is calculated for a binary gas mixture CH_4 - O_2 , and (iii) the particle tortuosity factor is determined from the particle porosity $\tau = \varepsilon^{-0.5}$. For the catalyst that shows the highest activity at steady state (C-MgO), the lowest external effectiveness η_e factor was 0.962 and the highest Thiele modulus ϕ was $3.921 \cdot 10^{-3}$ indicating that neither film nor pore diffusion limitation occur.

2.3 Results

2.3.1 Synthesis of nano-structured MgO catalysts

Different preparation methods and post-synthetic treatments have been applied with the objective to obtain magnesium oxide nano-particles with varying primary particle size, shape, and surface area. Sol-gel synthesis (SG-MgO), and oxidation of metallic magnesium (S-MgO) were used starting from metallic magnesium. Furthermore, commercially available magnesium oxide (C-MgO) was modified by hydrothermal treatment at normal pressure (HT-MgO), and at elevated pressure in a microwave autoclave (MW-MgO).

The surface area of the freshly calcined catalysts, which have been pressed and sieved prior to the catalytic reaction into split particles of a 0.2-0.3 mm sieve fraction, varies by an order of magnitude between $11 \text{ m}^2 \cdot \text{g}^{-1}$ for S-MgO and $111 \text{ m}^2 \cdot \text{g}^{-1}$ for MW-MgO (Table 4.1). The increase in specific surface area is not directly reflected in a decrease of the mean crystallite size determined by XRD indicating that surface texturing contributes substantially to the surface area measured by nitrogen adsorption, in particular for the catalysts prepared by hydrothermal post treatment and sol-gel synthesis.

The purity of the catalysts was controlled by chemical analysis (Table 2.2). The total concentration of transition metal ions, especially iron, chromium, and manganese, does not exceed 10 ppm for the materials that are derived from ultra-pure C-MgO. No additional traces of transition metals are introduced by subsequent hydrothermal treatments

that lead to the catalysts HT-MgO and MW-MgO. The comparatively high iron content of S-MgO (30 ppm) and SG-MgO (46 ppm) results from the use of commercial magnesium that was not purified by distillation.

The morphology and microstructure of the calcined catalysts was analyzed by electron microscopy (Fig. 2.1, left column). All catalysts expose mainly $\{100\}$ faces, but clearly differ with respect to size, shape and the abundance of steps and corners.

Table 2.1: Specific surface area and domain size determined by XRD of MgO catalysts before and after use in oxidative coupling of methane.

Catalyst	Preparation	Calcined catalysts ^[a]				Catalysts after use in OCM ^[b]			
		Catalyst ID ^[c]	S_{BET} [$m^2 \cdot g^{-1}$]	D_{XRD} [nm]	a [Å]	Catalyst ID	S_{BET} [$m^2 \cdot g^{-1}$]	D_{XRD} [nm]	a [Å]
S-MgO	combustion	12817	11.6	85.0	4.2144	12992	7.6	67.3	4.2135
C-MgO	reference	12288	19.1	23.1	4.2145	12798	7.9	77.3	4.2145
SG-MgO	sol-gel	12342	38.6	11.4	4.2175	12500	6.8	84.9	4.2155
HT-MgO	hydrothermal	12498	71.6	14.4	4.2177	12628	n.a	n.a	n.a
MW-MgO	microwave	12994	111.0	13.3	4.2176	13036	12.2	70.5	4.2138

^a $O_2/Ar = 20/80$, 150 mL/min, heating rate 3 K/min, $T=1123$ K, $t=6$ h.

^b $CH_4/O_2/N_2=3/1/1$, $W/F=0.15$ g·s·ml⁻¹, $T=1073$ K, after approximately 300 h TOS.

^c The catalyst ID is required to clearly identify the batch number of various reproductions of catalyst synthesis.

The oxidation of metallic magnesium in air produces large, almost ideal cubic particles, exhibiting mainly $\{100\}$ faces (S-MgO, Fig. 2.1 A). The particles are partially aggregated via shared faces. Due to large size and flat surfaces S-MgO exhibits a low specific surface area of $12 \text{ m}^2 \cdot \text{g}^{-1}$. The average crystallite size determined by XRD is around 85 nm, however, scanning electron microscopy indicates a rather broad size distribution with particles in the range between 50 and 200 nm (Fig. S 2.1 A). Such polydisperse powders are often obtained by combustion of metallic magnesium in air. [65]

The specific surface area of C-MgO after calcination at 1123 K is also relatively small (Table 4.1). The side length of the crystallites observed by TEM (Fig. 2.1 C) is approximately 20-30 nm, which is in agreement with the mean crystallite size of 23 nm measured by XRD. The primary particles are of regular cubic morphology exposing $\{100\}$ faces with sharp edges and corners. The height of the steps that often appear close to the edges of the cubes is in the nanometer range. Smaller steps, in the range of just few Ångströms and eventually even in the dimension of one Mg-O distance (mono-atomic steps) can regularly be observed within the $\{100\}$ faces. The primary particles are agglomerated or aggregated to form clusters up to 5 μm in size (Fig. S 2.1 C).

Magnesium oxide obtained by sol-gel synthesis (SG-MgO) has a larger surface area of $39 \text{ m}^2\cdot\text{g}^{-1}$ and a smaller mean crystallite size of ca. 11 nm. TEM (Fig. 2.1 E) and SEM (Fig. S 2.1 E) images reveal rectangular primary particles with a side length of approximately 20 nm and a narrow size distribution. The microstructure of SG-MgO is quite similar to C-MgO. Agglomerates or aggregates of primary particles comprise a cluster size of approximately $5 \mu\text{m}$.

MgO catalysts obtained by hydrothermal treatment of C-MgO either at normal pressure (HT-MgO) or in a microwave-heated autoclave (MW-MgO) are characterized by substantial nano-structuring of the surface. Whereas the mean crystallite size of the two catalysts is comparable to C-MgO or SG-MgO (Table 4.1), surface roughness is reflected in high surface areas. The regular cubic structure of the starting material C-MgO is no longer visible by TEM (Fig. 2.1 G and I). Conglomerates without distinguishable primary particles are embedded in clusters of a size of ca. $1 \mu\text{m}$ (Fig. S 2.1 G and H).

Table 2.2: Content of traces of transition metals as determined by using inductively coupled plasmaoptical emission spectrometry (ICPOES).

Catalyst	Transition metal impurities [ppm]						
	Cr	Mn	Fe	Co	Ni	Cu	Zn
S-MgO	3.8	6.5	30.3	0.2	1.9	7.2	4.8
C-MgO	0.2	3.0	3.8	0.1	0.1	0.5	1.4
SG-MgO	8.4	10.4	46.3	0.1	6.8	4.0	1.6
HT-MgO	0.1	2.9	3.2	0.1	0.1	0.9	1.6
MW-MgO	0.2	3.1	2.6	0.2	0.2	0.6	1.5

Sintering phenomena are observed for all catalysts after use in the oxidative coupling of methane at 1073 K for approximately 300 hours time on stream. The domain size determined by XRD increases substantially except in the case of S-MgO, that shows a slight size reduction of the initially very large particles (Table 4.1). In agreement with a similar size of the coherently scattering domains in the used catalysts, the specific surface area of all used catalysts is similar and varies between 7 and $12 \text{ m}^2\cdot\text{g}^{-1}$. Sintering is also visible by TEM (Fig. 2.1, right column) and SEM (Fig. S 2.1, right column). After catalysis, the morphology of the primary particles is much more rounded. The characteristic sharp edges and corners of the cubic structure have disappeared and pseudo $\{110\}$ as well as $\{111\}$ faces consisting of stepped edges between $\{100\}$ planes and numerous corners have formed.

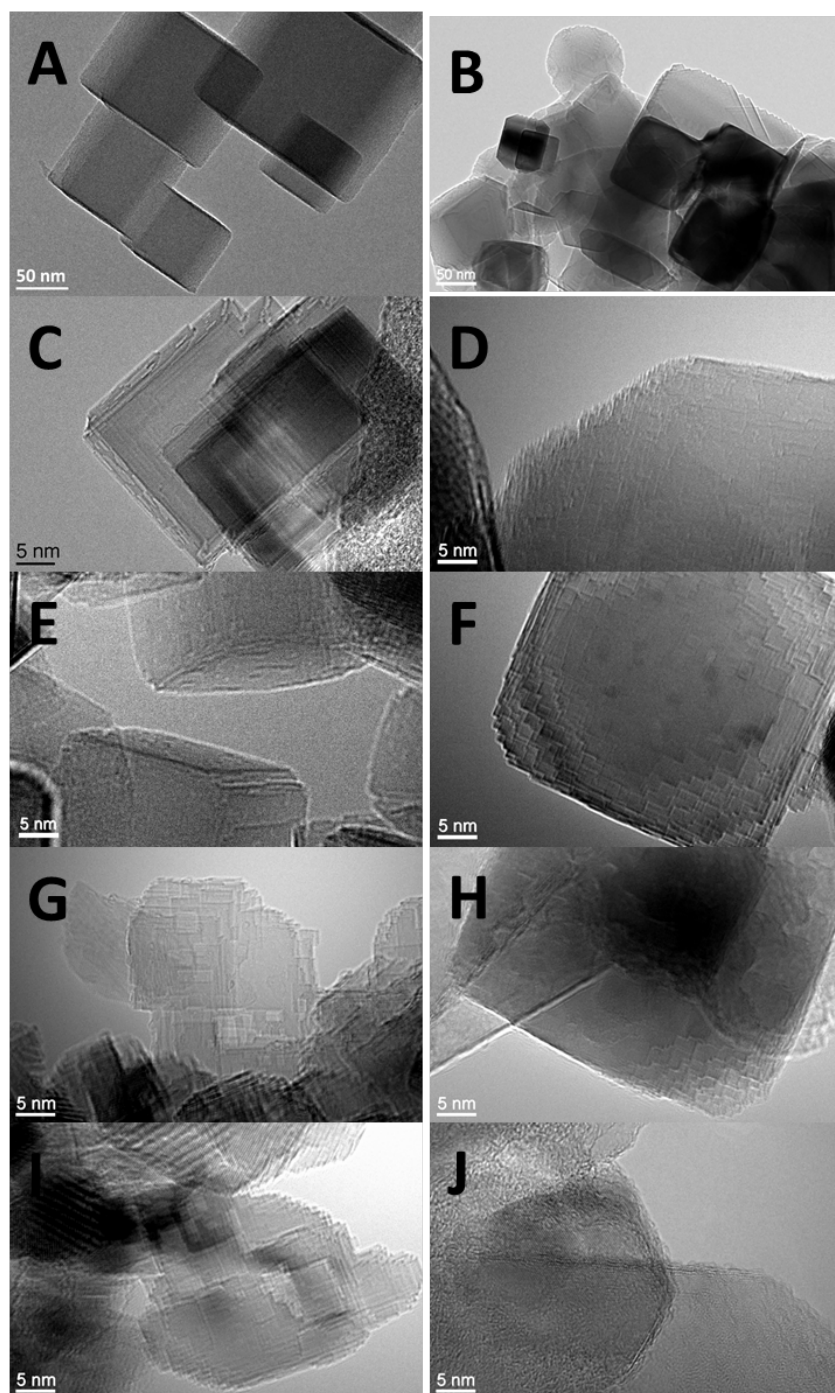


Figure 2.1: TEM images of calcined MgO (on the left-hand side) and MgO after oxidative coupling of methane for 300 hours time on stream ($\text{CH}_4/\text{O}_2/\text{N}_2=3/1/1$, $\text{W/F}=0.15 \text{ g}\cdot\text{s}\cdot\text{ml}^{-1}$, $T=1073 \text{ K}$) (on the right-hand side). From top to bottom: S-MgO (A,B), C-MgO (C,D), SG-MgO (E,F), HT-MgO (G,H), and MW-MgO (I,J).

2.3.2 Oxidative coupling of methane

2.3.2.1 Temporal developments of catalytic properties

The five MgO materials were investigated in the oxidative coupling of methane (OCM). For a better comparison with the kinetic data in the literature, the experimental condition for the OCM reaction were chosen similar to the reference work of Schweer *et al.* [12]. The catalysts experience a strong deactivation with time on stream (TOS) until steady state activity is reached (Fig. 2.2). The time that is required to attain the steady state varies between 1 hour and 230 hours depending on the method that has been applied to synthesis the MgO catalysts. Consequently, the deactivation rate seems to depend strongly on the initial structure of the magnesium oxide. The stability of the catalysts in the OCM reaction decreases in the following order: C-MgO > SG-MgO > MW-MgO > HT-MgO > S-MgO (Fig. 2.2). At 1073 K in a feed of $\text{CH}_4/\text{O}_2/\text{N}_2=3/1/1$ and applying a contact time of $W/F=0.150 \text{ g}\cdot\text{s}\cdot\text{ml}^{-1}$, full conversion of oxygen is achieved for all MgO catalysts (except for S-MgO) in the initial state of the reaction after a few minutes time on stream. Under conditions of total oxygen consumption, the methane conversion is leveled off at a maximum of 30 % for all affected catalysts (Fig. 2.2A). The selectivity to C_{2+} products decreases simultaneously, but in most of the cases only slightly (Fig. 2.2B)

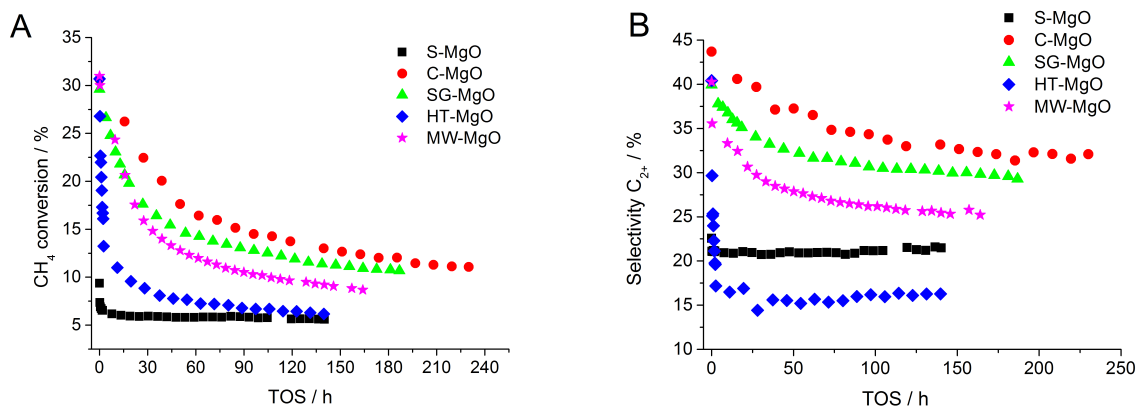


Figure 2.2: Changes in the conversion of methane (A) and in the selectivity to C_{2+} products (B) with time on stream in the oxidative coupling of methane at $T=1073 \text{ K}$ in a feed of $\text{CH}_4/\text{O}_2/\text{N}_2=3/1/1$, using a catalyst mass of $m_{\text{cat}}=150 \text{ mg}$, and applying a contact time of $W/F=0.15 \text{ g}\cdot\text{s}\cdot\text{ml}^{-1}$ over the differently prepared MgO catalysts.

With time on stream, the ratio of ethylene to ethane decreases at the similar rate as the methane conversion decreases (Fig. 2.3A). The carbon dioxide to carbon monoxide ratio declines at a much faster rate (Fig. 2.3B). Fig. 2.4 emphasizes in another way the change

of selectivity with time of stream for the C-MgO catalyst. The decrease of C_2H_4 is accompanied by a decrease of CO_2 , while C_2H_6 and CO follow the opposite trend. This indicates changes in the reaction pathway with time on stream. However, it has to be considered that the formation of the products and the consumption of intermediates are interrelated within a complex reaction network.

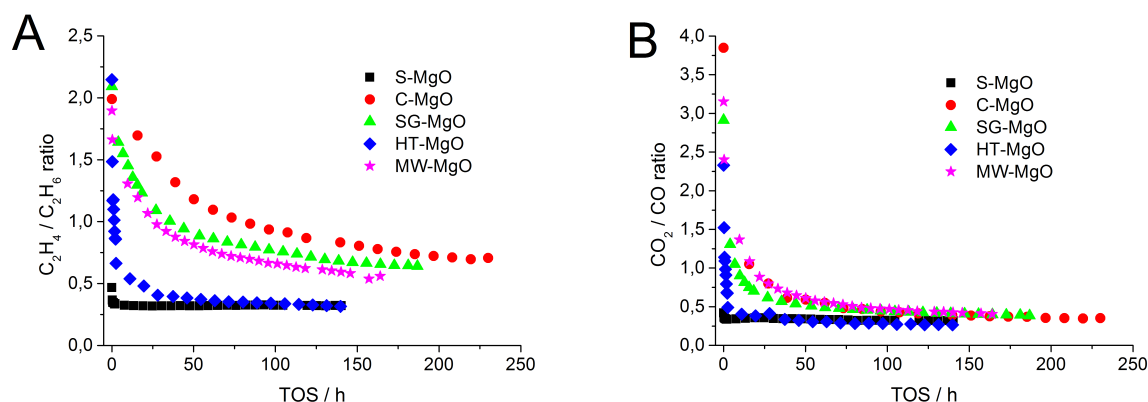


Figure 2.3: Change in the selectivity ratio ethylene/ethane (A), and CO_2/CO (B) with time on stream in the same experiments as presented in Fig. 2.2.

In order to investigate relations between particle morphology, specific surface area, and reactivity, the C-MgO catalyst was analyzed after 6, 20 and 66 hours time on stream by TEM and nitrogen adsorption (Fig. 2.5). The MgO particles are attacked at first at the outer surface of the primary cubic particles exposing $\{100\}$ planes and many steps. With time on stream the cubic particles are transformed into particles exhibiting an octahedral shape (Fig. 2.5B). After 20 hours time on stream, the size of the particles becomes larger but steps and corners can still be recognized (Fig. 2.5C). After 66 hours time on stream the particles are completely rounded and no $\{100\}$ structure can be observed (Fig. 2.5D). With increasing particle size, the surface area decreases as indicated in the caption of Fig. 2.5.

2.3.2.2 Initial performance at oxygen conversion <1

Under the reaction conditions applied in the previous section, total oxygen consumption was observed at time $t=0$ in the case of HT-, MW-, C-, and SG-MgO. As a consequence, the methane conversion levels off at ca. 30 % for all catalysts except S-MgO that shows lower methane conversion. Consequently, similar selectivity towards C_{2+} hydrocarbons of ca. 40 % is observed for all catalysts, which renders a comparison of the catalysts at $t=0$

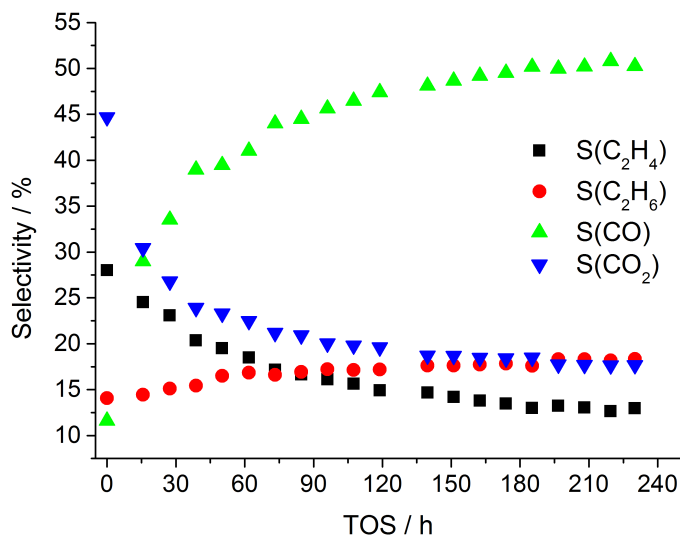


Figure 2.4: Changes in the selectivity to the products ethylene, ethane, CO, and CO₂ with time on stream exemplarily shown for catalyst C-MgO in the same experiments as presented in Fig. 2.2

impossible. To overcome this limitation, the catalysts were tested at lower contact time ($W/F = 0.033 \text{ g}\cdot\text{s}\cdot\text{ml}^{-1}$) and temperature (1023 K). The reactivity of all catalysts under these conditions at $t=0$ is compared in 2.3. MW-MgO exposes the highest consumption rate of methane, combined with the highest yield of C₂₊ hydrocarbons, and the highest ratios of CO₂/CO and C₂H₄/C₂H₆ selectivity, respectively. The selectivity ratios increase with increasing methane and oxygen conversion. The rates measured over the differently prepared MgO catalysts differ by an order of magnitude. The methane consumption rate decreases in the order MW-MgO > SG-MgO > C-MgO > HT-MgO > S-MgO. The rates do not directly correlate with the specific surface areas of the catalysts. Therefore, normalization of the rates to the specific surface area changes the ranking with respect to activity. The specific rate decreases in the order C-MgO > SG-MgO > MW-MgO > S-MgO > HT-MgO.

2.3.2.3 Steady state performance

All kinetic investigations in the stationary state have been performed after reaching constant oxygen and methane conversion and selectivity at 1073 K in a feed of CH₄/O₂/N₂=3/1/1 using a catalyst mass of $m_{\text{cat}}=150 \text{ mg}$ and applying a contact time of $W/F=0.150 \text{ g}\cdot\text{s}\cdot\text{ml}^{-1}$ (*i.e.*, after the experiment shown in Fig. 2.2). This takes 150-250 hours, depending on the catalyst preparation. The performance of the catalysts at steady state is summarized in

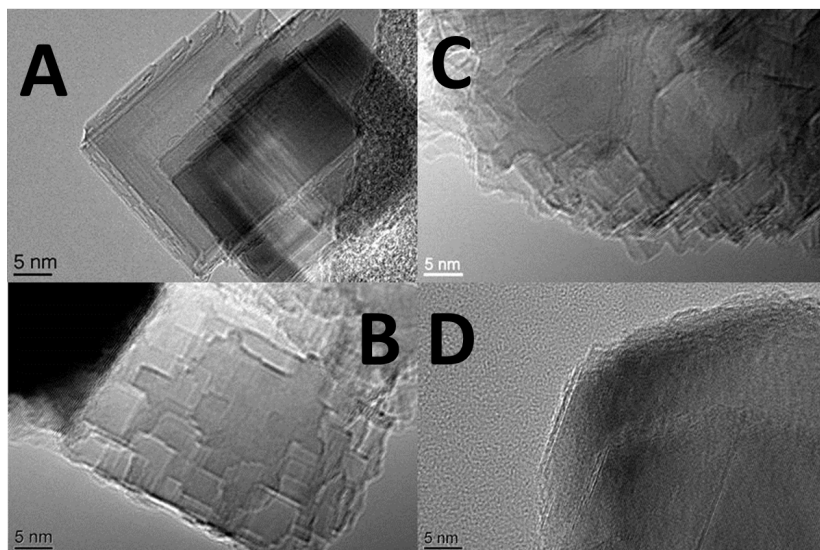


Figure 2.5: TEM images of C-MgO at different time on stream in the OCM reaction, same experimental condition as in Fig. 2.2. A) Before reaction ($S_{BET}=53.9 \text{ m}^2\cdot\text{g}^{-1}$), B) after 6 h TOS ($S_{BET}=22.3 \text{ m}^2\cdot\text{g}^{-1}$), C) after 20 h TOS ($S_{BET}=16.4 \text{ m}^2\cdot\text{g}^{-1}$), D) after 66 h TOS ($S_{BET}=15.0 \text{ m}^2\cdot\text{g}^{-1}$).

Table 2.4.

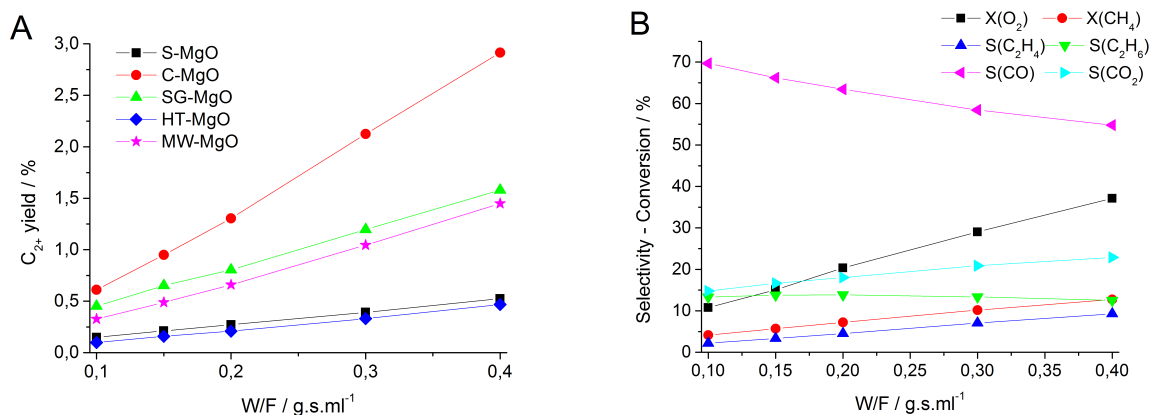


Figure 2.6: Total yield of the coupling products ethane and ethane for all catalysts (A), and conversion and selectivity exemplarily shown for C-MgO (B) as a function of the contact time at $T=1023 \text{ K}$, using a catalyst mass of $m_{\text{cat}}=150 \text{ mg}$, and a feed composition of $\text{CH}_4/\text{O}_2/\text{N}_2=3/1/1$.

The comparison reveals that the differences between the catalysts in the steady state are

Table 2.3: Consumption rate of methane, conversions and selectivity measured over MgO catalysts in the oxidative coupling of methane in the initial state ($t=0$) at $T=1023$ K, applying a feed composition of $\text{CH}_4/\text{O}_2/\text{N}_2=3/1/1$, and a contact time of $0.033 \text{ g}\cdot\text{s}\cdot\text{ml}^{-1}$.

Catalyst	r_{CH_4} [$\mu\text{mol} \cdot \text{s}^{-1} \cdot \text{g}_{\text{cat}}^{-1}$]	r_{CH_4} [$\mu\text{mol} \cdot \text{s}^{-1} \cdot \text{m}_{\text{cat}}^{-2}$]	X_{CH_4} [%]	X_{O_2} [%]	S_{C_2+} [%]	$\text{CO}_2/\text{CO}^{[a]}$	$\text{C}_2\text{H}_4/\text{C}_2\text{H}_6^{[a]}$
S-MgO	16.3	1.41	2.02	5.30	5.24	0.25	0
C-MgO	185.2	9.70	22.61	74.64	27.59	1.10	0.72
SG-MgO	214.4	5.56	26.04	87.36	29.84	1.51	1.01
HT-MgO	65.0	0.91	8.04	26.61	4.73	0.40	0.19
MW-MgO	249.0	2.24	30.16	97.75	40.88	2.28	1.42

^a ratio of selectivity

much smaller compared to the differences in the initial performance. Still, C-MgO shows the highest specific activity and the ranking of the specific activity remains the same as the ranking of specific rates measured at $t=0$. No systematic trends with respect to the yield and selectivity ratios as a function of the oxygen and methane conversion can be observed any more in the stationary state.

Table 2.4: Consumption rate of methane, conversions and selectivity measured over MgO catalysts in the oxidative coupling of methane in the stationary state at $T=1023$ K, applying a feed composition of $\text{CH}_4/\text{O}_2/\text{N}_2=3/1/1$, and a contact time of $0.15 \text{ g}\cdot\text{s}\cdot\text{ml}^{-1}$.

Catalyst	r_{CH_4} [$\mu\text{mol} \cdot \text{s}^{-1} \cdot \text{g}_{\text{cat}}^{-1}$]	r_{CH_4} [$\mu\text{mol} \cdot \text{s}^{-1} \cdot \text{m}_{\text{cat}}^{-2}$]	X_{CH_4} [%]	X_{O_2} [%]	S_{C_2+} [%]	$\text{CO}_2/\text{CO}^{[a]}$	$\text{C}_2\text{H}_4/\text{C}_2\text{H}_6^{[a]}$
S-MgO	4.17	0.55	2.36	10.88	9.01	0.39	0.07
C-MgO	10.43	1.32	5.70	15.07	17.12	0.25	0.24
SG-MgO	8.57	1.26	4.70	13.22	13.85	0.24	0.18
HT-MgO	4.72	n.a.	2.77	7.71	5.74	0.18	0.09
MW-MgO	7.38	0.60	4.31	12.50	11.33	0.26	0.19
SiC	0.25	n.d.	0.14	1.18	64.88	0.00	0.00

^a ratio of selectivity

The detailed kinetic study under stationary conditions comprising all five MgO catalysts reveals an interesting correlation between temperature, contact time, methane to oxygen ratio, and reactivity in the OCM reaction. First, in contrast to the work of Hargreaves *et al.*, [57] in which OCM over MgO was studied at the same reaction temperature, but at higher contact times and in slightly different feed, the contact time has a significant effect on methane conversion and selectivity to C_{2+} hydrocarbons, respectively (Figures 2.6, S 2.2 - S 2.5). The C_{2+} yield increases for all catalysts with increasing contact times (Fig. 2.6 A), which is due to an increase in methane conversion and ethylene selectivity, while the CO selectivity decreases (Figures 2.6 B, S 2.2 - S 2.5). In parallel, the oxygen

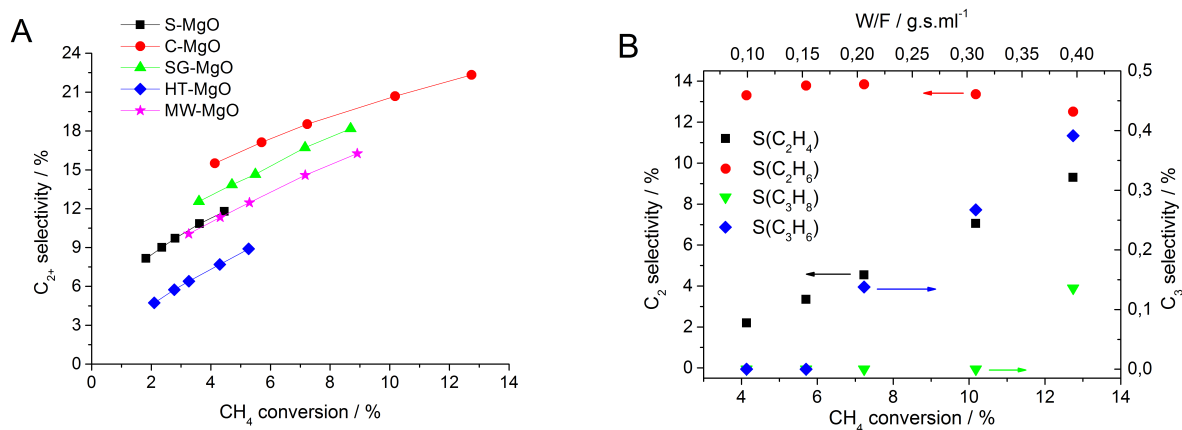


Figure 2.7: Total selectivity to the coupling products ethane and ethane as a function of methane conversion (A), and selectivity to C_2 , and C_3 hydrocarbons exemplarily shown for catalyst C-MgO as a function of methane conversion (B) measured at $T=1023$ K, using a catalyst mass of $m_{cat}=150$ mg, and a feed composition of $CH_4/O_2/N_2=3/1/1$. The conversion was changed by variation of the contact time in the range between 0.1 and 0.4 $g \cdot s \cdot ml^{-1}$.

conversion increases as well. The C_2H_6 selectivity is not affected. However, the increase in the C_{2+} yield is different for the various catalysts, which may also explain the discrepancy to the studies reported previously. [57] Whereas C-MgO shows a 6 times higher yield at $W/F = 0.4$ $g \cdot s \cdot ml^{-1}$ than at $W/F = 0.1$ $g \cdot s \cdot ml^{-1}$, the influence of the contact time on the yield is less pronounced for S-MgO and HT-MgO (Fig. 2.6 A). The same trend becomes also evident from Fig. 2.7 A, where the C_{2+} selectivity is plotted as a function of methane conversion that was changed by varying the contact time at a reaction temperature of $T=1023$ K in the same range and in the same steps in all experiments. The selectivity increases with increasing methane conversion for all catalysts. Fig. 2.7A illustrates also that at the same methane conversion, C-MgO shows the highest selectivity to coupling products followed by $SG-MgO > MW-MgO = S-MgO > HT-MgO$. The representation of the selectivity towards ethylene and ethane as a function of methane conversion for the C-MgO catalyst shows that when methane conversion increases (*i.e.* by increasing the contact time), the C_2H_4 selectivity increases linearly, while the C_2H_6 selectivity stays constant (Fig. 2.7 B). With increasing methane conversion, *i.e.* increasing W/F , the formation of C_3 hydrocarbons sets in, starting with propene followed by propane. This behavior is not in agreement with a reaction pathway, in which ethylene is formed from ethane through oxidative dehydrogenation. For evaluation of the gas phase contributions under the same reaction conditions, silicon carbide was studied, that shows methane conversion below 1% (Fig. 2.8). The trends in ethylene and ethane selectivity over SiC clearly differ from the MgO catalysts. At low methane conversion only C_2H_6 is formed. At higher CH_4 conver-

sion, ethane seems to be decomposed to CO and the formation of C_2H_4 occurs at even higher methane conversion accompanied by the formation of CO_2 .

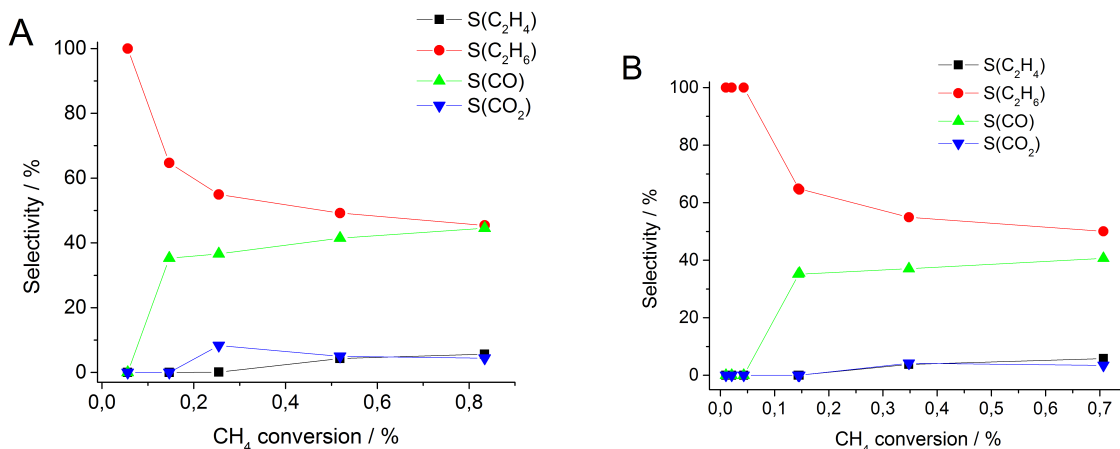


Figure 2.8: Total selectivity to the coupling products ethane and ethane over SiC as a function of methane conversion measured by variation of the contact time (A) (same condition as in Fig. 2.7) and by variation of the temperature (B) (same condition as in Fig. 2.10).

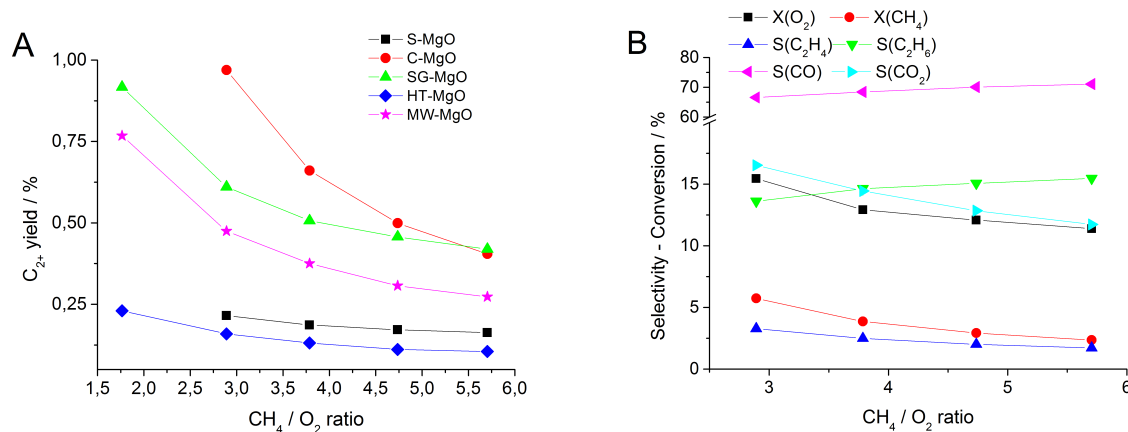


Figure 2.9: Total yield of the coupling products ethane and ethene (A), and conversion and selectivity exemplarily shown for catalyst C-MgO as a function of the CH_4/O_2 ratio in the feed at $T=1023$ K, using a catalyst mass of $m_{cat}=150$ mg, and a contact time of 0.15 g·s·ml $^{-1}$.

With decreasing oxygen concentration in the feed, the C_{2+} selectivity decreases (Fig. 2.9 A). The reaction orders with respect to CH_4 at fixed O_2 concentration, and with respect to

Table 2.5: Kinetic parameters measured over MgO catalysts in oxidative coupling of methane in the stationary state. The apparent activation energies E_a were determined based on the methane consumption rate in the temperature range $T=923-1073$ K, applying a contact time of $0.15 \text{ g}\cdot\text{s}\cdot\text{ml}^{-1}$, and a feed composition of $\text{CH}_4/\text{O}_2/\text{N}_2=3/1/1$. The reaction orders were determined at $T=1023$ K at a contact time of $0.15 \text{ g}\cdot\text{s}\cdot\text{ml}^{-1}$ and variation of the CH_4/O_2 ratio from 0.75 to 3.6 and the O_2/CH_4 ratio from 3 to 6.

Catalyst	E_a (r_{CH_4}) [$\text{kJ}\cdot\text{mol}^{-1}$]	CH_4 reaction order	O_2 reaction order
S-MgO	139 ± 3	0.4	0.7
C-MgO	100 ± 5	0.0	1.3
SG-MgO	133 ± 2	0.3	0.8
HT-MgO	156 ± 2	0.4	0.7
MW-MgO	119 ± 3	0.1	0.9
SiC	297 ± 13	n.d.	n.d.

O_2 at fixed CH_4 concentration are summarized in Table 2.5. The results indicate that the overall reaction rate is almost independent from the methane partial pressure but that the oxygen partial pressure plays an important role in the OCM reaction over MgO. For all the catalysts an increase in the CH_4/O_2 ratio leads to a decrease in methane conversion, as well as CO_2 and C_2H_4 selectivity (results exemplarily shown for C-MgO in Fig. 2.9 B). In contrast, the selectivity to ethane and carbon monoxide increase with decreasing oxygen partial pressure in the feed. These opposite trends for CO and CO_2 indicate that the two products are formed via different pathways (see also Fig. 2.6 B).

The temperature has a major effect on the OCM reactivity. By increasing the temperature from 873 K up to 1073 K, the yield of C_{2+} hydrocarbons increases exponentially (Fig. 2.10 A). The apparent activation energies calculated based on the rate of methane consumption for the five catalysts are shown in Table 5. The synthesis and deactivation history of MgO have a significant impact on the apparent activation energy that varies between $100 \text{ kJ}\cdot\text{mol}^{-1}$ for C-MgO and $156 \text{ kJ}\cdot\text{mol}^{-1}$ for HT-MgO although all catalysts lost their high initial activity and approach similar performance in the stationary state (Table 2.4). Much higher activation energy is measured over SiC ($297 \text{ kJ}\cdot\text{mol}^{-1}$) where gas-phase reactions prevail. Here, only ethane is formed up to 998 K, at 1023 K carbon monoxide starts to occur and ethylene and carbon dioxide appear in the product mixture at temperatures higher than 1048 K. These observations are in agreement with a reaction network dominated by gas-phase reactions, in which ethylene is a consecutive product formed from ethane, CO is the major pyrolysis product, whereas CO_2 is formed only in small amounts. [66] Thus, MgO as a catalyst clearly lowers the energy barrier of methane activation by at least $150 \text{ kJ}\cdot\text{mol}^{-1}$ in comparison to the gas phase reaction. With increasing temperature, the selec-

tivity towards C_{2+} hydrocarbons and CO_2 increases, which is the same trend as observed with increasing methane conversion (results exemplarily shown for C-MgO in Fig. 2.10 B). The increase in selectivity with temperature is consistent with the thermodynamics of the selective and non-selective reaction steps in methane oxidation. [7]

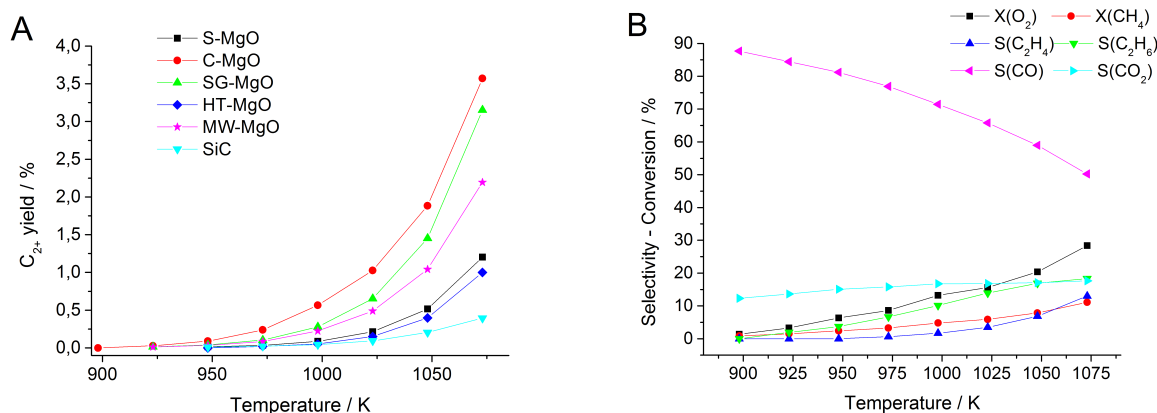


Figure 2.10: Total yield of the coupling products ethane and ethane (A), and conversion and selectivity exemplarily shown for C-MgO (B) as a function of the temperature, using a catalyst mass of $m_{cat}=150$ mg, a contact time of 0.15 g·s·ml $^{-1}$ and a feed composition of $CH_4/O_2/N_2=3/1/1$.

2.3.2.4 Stability of products in the OCM reaction

The stability of the products ethane, ethylene, and carbon dioxide and their influence on the reaction network have been investigated by addition of 1 to 5 vol.% of these gases to the feed under standard steady state condition, *i.e.* $T=1023$ K, CH_4/O_2 ratio = 3, $W/F=0.150$ g·s·ml $^{-1}$, using nitrogen as balance. Since reaction products are co-fed, it is not possible to determine the selectivity. Therefore, partial pressures of the effluent gas components measured by gas chromatography are presented in Fig. 2.11 as a function of the concentration of ethane added to the feed.

The straight black line represents the amount of ethane that should be measured at the outlet of the reactor if no added ethane would react at all. In agreement with the observations made by Roos et al. for Li/MgO catalysts [67], C_2H_6 is not stable in the OCM feed under standard condition. A detailed look inside the gas phase composition exemplarily shown in Fig. 2.11 B for C-MgO indicates that ethane is not oxidized completely to carbon oxides, but transformed into C_2H_4 to a considerable fraction probably through oxidative dehydrogenation of ethane, since the oxygen conversion increases at the same time from

20 to 40 %. The abundance of CO in the effluent gas increases as well probably due to parallel pyrolysis of ethane. Methane conversion is only slightly affected. Hence, a competition between oxidative dehydrogenation of ethane and oxidative coupling of methane is not obvious. The high ethylene content indicates that the partial oxidation of ethane is very selective over MgO. High selectivity in oxidative dehydrogenation of ethane has been reported frequently over alkaline earth oxides. [68]

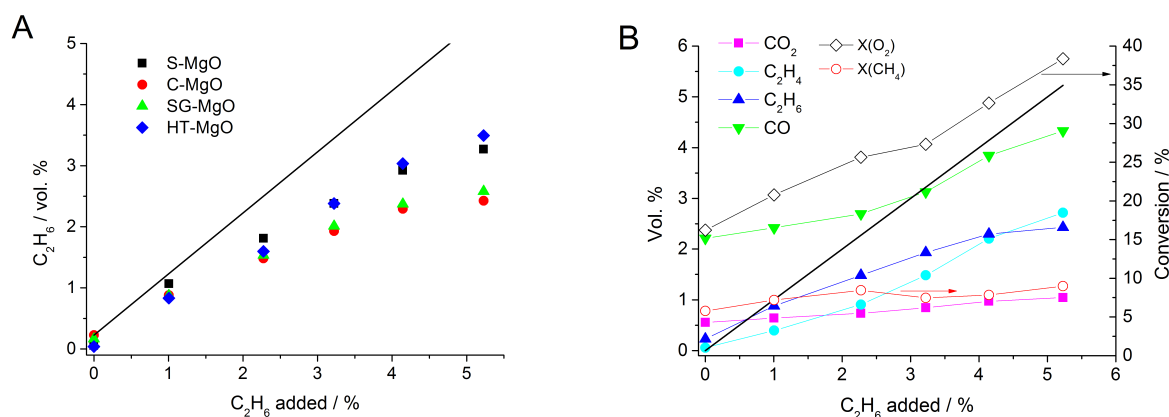


Figure 2.11: Concentration of ethane measured at the outlet of the reactor for all catalysts (A), and concentration of all products as well as methane and oxygen conversion exemplarily shown for catalyst C-MgO (B) as a function of ethane added to the feed at 1023 K, CH_4/O_2 ratio of 3, and constant contact time of $0.15 \text{ g}\cdot\text{s}\cdot\text{ml}^{-1}$. The black straight line corresponds to zero conversion of the added ethane.

In contrast to ethane, ethylene is more stable when added to the OCM feed. This observation is consistent with the higher dissociation energy of the C-H bond in ethylene compared to ethane, 464.2 and $420.5 \text{ kJ}\cdot\text{mol}^{-1}$, respectively. [69] Only C-MgO and SG-MgO are able to convert more ethylene than SiC. After addition of 5% ethylene over C-MgO, conversion of methane and oxygen, as well as the concentration of CO_2 , C_2H_6 and CO increase approximately by a factor of 2 (Fig. 2.12 B). This differs from the results of Roos *et al.* [67] who reported a decrease in methane conversion after ethylene addition. However, in the latter work the catalyst was operated under conditions of complete oxygen consumption. In such a case, the OCM and the ODH reaction compete for the oxygen in the feed. The present increase in methane conversion is probably caused by an increase in the pool of activated oxygen or radicals due to the reaction of the added ethylene.

In summary, the high selectivity to ethylene in the ethane addition experiments indicates that the ethylene generated under OCM conditions is formed by a mechanism different

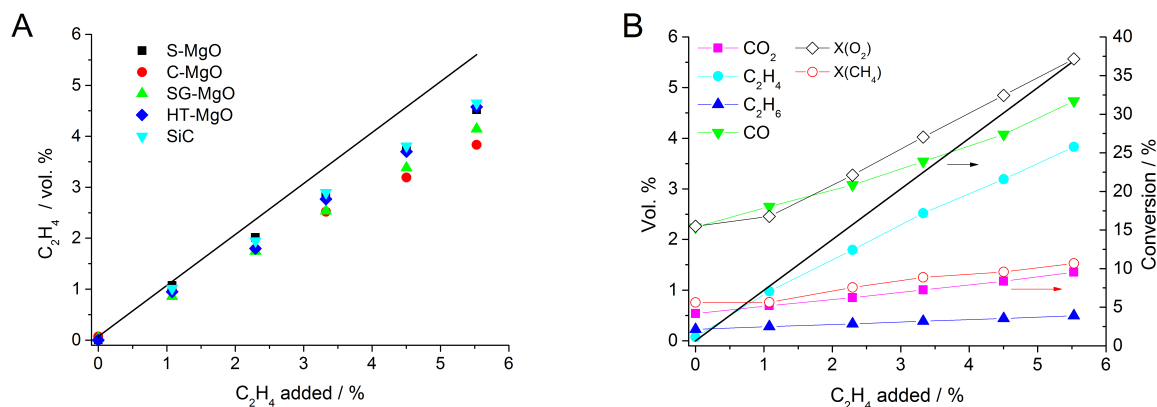


Figure 2.12: Concentration of ethylene measured at the outlet of the reactor for all catalysts (A), and concentration of all products as well as methane and oxygen conversion exemplarily shown for catalyst C-MgO (B) as function of ethylene added in the gas feed at 1023 K, CH_4/O_2 ratio of 3, and constant contact time of $0.15 \text{ g}\cdot\text{s}\cdot\text{ml}^{-1}$. The black straight line corresponds to zero conversion of the added ethylene.

from oxidative dehydrogenation of ethane. ODE happens when auxiliary ethane is added to the OCM feed.

The addition of CO_2 to the feed at 1023 K is associated with only slight decrease in the oxygen conversion (Fig. 2.13). Methane conversion, and CO , CO_2 , C_2H_4 and C_2H_6 concentration stay stable upon addition of 5 vol.% CO_2 . These results indicate that neither dry reforming of methane occurs over MgO under these experimental conditions nor that CO_2 is a poison for the active sites responsible for methane activation.[4] Moreover, no indication was found that the selectivity of C2 products is favored by the presence of CO_2 in the feed as suggested in case of Li/MgO catalysts. [67, 70]

2.4 Discussion

MgO catalysts exhibiting different materials properties, like mean crystallite size, particle size, surface area, and concentration of surface defects were compared in view of their reactivity in the oxidative coupling of methane. The importance of structural aspects in the oxidative coupling of methane over magnesium oxide has been reported previously. [57] Hargreaves et al. studied the morphology of three differently prepared MgO catalysts by transmission electron microscopy and the results were correlated with catalyst performance in the oxidative coupling of methane, resulting in the conclusion that the active sites are

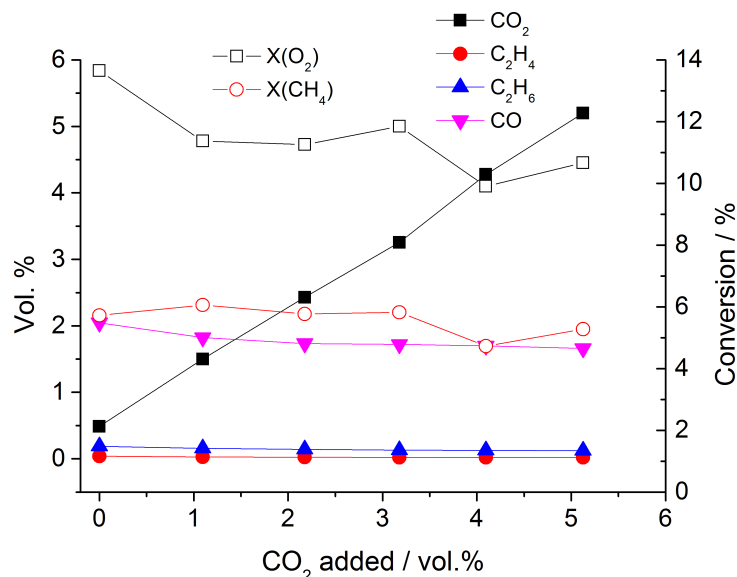


Figure 2.13: Methane and oxygen conversion and concentration of products as function of CO₂ added to the feed over C-MgO at 1023 K, CH₄/O₂ ratio of 3, and contact time of 0.15 g·s·ml⁻¹

mainly located on the planar 100 surfaces and not on steps or corners. Magnesium oxide, which exposed a greater fraction of higher index planes, like {111}, was particularly selective, indicating that a number of different active centers contribute to the catalytic performance on nanostructured MgO.

In the present work, variability in particle morphology and nano-structure of the MgO surface was achieved by applying different synthesis methods and post-treatment procedures of commercially available MgO, respectively. Although all investigated catalysts are chemically composed of the same binary oxide (Table 4.1), the materials exhibit interesting differences in their reactivity in oxidative coupling of methane. An impact of the transition metal impurities (Table 2.2) on the catalytic properties can be excluded. This becomes in particular obvious from comparison of the catalysts C-MgO, HT-MgO, and MW-MgO, which are derived from the same mother MgO having, therefore, very similar concentration of transition metal impurities, but show substantial differences in their catalytic behavior. Accordingly, these differences are probably associated with different surface termination or defect concentration of the magnesium oxides, but not with the impurities

Magnesium oxide is not stable in OCM with time on stream. The deactivation rate varies for the different MgO catalysts (Figures 2.2-2.4) and depends apparently on the synthesis method, and, therefore, on the initial nanostructure. Along with the decrease in methane

and oxygen conversion, the selectivity towards coupling products changes in favor of ethane (Fig. 2.3 A and 2.4). At the same time, the total oxidation to CO_2 is inhibited resulting in an increased amount of CO in the product mixture. CO is a typical gas-phase reaction product. [66] Therefore, this observation might indicate a change in the reaction mechanism from a surface or surface-mediated reaction to a predominantly gas-phase controlled reaction. In parallel with deactivation, drastic changes in catalyst morphology are observed. Sintering is detected by XRD (Table 4.1) and electron microscopy (Figures 2.1, 2.5 and S 2.1). The surface termination becomes more regular, which is expressed in the disappearance of the mono-atomic steps, which are quite abundant in the fresh catalysts (Fig. 2.1). Still, some differences are retained in the steady state reflected in different rates of methane consumption and product formation (Table 2.4), as well as apparent activation energies that vary between 100 and 150 $\text{kJ}\cdot\text{mol}^{-1}$ (Table 2.5) depending on the catalyst preparation. Since all five catalysts are composed of magnesium oxide only, such differences in the apparent activation energy are indeed surprising. The kinetic investigation under steady state conditions described in section 3.2.3 indicates that CO_2 and CO are probably formed via parallel pathways, which may result in different apparent activation energies calculated based on the consumption rate of methane when the concentration of the corresponding active sites involved in rate determining steps is very different on the catalyst surface under steady state conditions. [71] In addition, contributions to gas phase chemistry that vary with time on stream cannot be excluded. Comparison of Fig. 2.2 A with Figures 2.3 A and B, respectively, reveals that the ethylene/ethane ratio changes in parallel to methane conversion, but the CO_2/CO ration shows a completely different behavior, which may be interpreted in terms of a change in the reaction pathway with time on stream.

The reaction kinetics of the oxidative coupling of methane over earth alkaline oxides, whether pure or doped with alkaline elements, have been studied frequently. [11, 15, 16, 72–78] Generally, it is proposed that the reaction is initiated heterogeneously on the catalyst surface and continued as homogeneous reaction in the gas phase. [7] The initial step of the selective coupling of two methane molecules is assumed to be the surface-mediated hydrogen atom abstraction from CH_4 according to an Eley-Rideal-type reaction between oxygen adsorbed on the catalyst surface and methane reacting from the gas phase. [74] Surface O^- centers are supposed to be responsible for hydrogen abstraction, [4] which yields a neutral methyl radical that is released into the gas phase for further reactions. Kinetic isotope effect (KIE) studies suggested the involvement of a C-H bond scission in the rate-determining step over Li/MgO as catalyst. [13] However, it has also been observed that the KIE decreases with increasing methane to oxygen ratio, which indicates that a single rate-determining step does not exist when oxygen is used as oxidizing agent. [14] These findings are in agreement with the varying apparent activation energy measured over the MgO catalyst series in the present work and the interpretation in terms of the parallel

occurrence of independent reaction pathways that cause methane consumption. Accordingly, the apparent reaction order with respect to methane and oxygen also differ for the different catalysts (Table 2.5). Furthermore, the yield of C_{2+} hydrocarbons increases with increasing methane and oxygen consumption (Fig. 2.7), which would be consistent with the comparatively low sticking coefficient of methyl radicals determined on MgO that has been associated with limited consecutive surface reactions of these radicals towards undesired products of total oxidation. [16, 79] However, the contributions of homogeneous and heterogeneous reaction steps that follow the formation of the methyl radical and that determine the selectivity of the reaction are less clear. [15, 16] Analogous uncertainties exist in the literature with respect to the nature of oxygen species that are involved in the reactions. There is no doubt that oxygen is required for selective methane coupling. The oxygen partial pressure has a strong impact on the overall rate of the reaction over pure magnesium oxide as reflected in O_2 reaction orders close to one in the stationary state (Table 2.5). When the reaction is performed under such conditions that the oxygen consumption at $t=0$ is not complete, a linear dependency of the rate of methane consumption on the conversion of oxygen is observed for the different catalysts (Fig. 2.14). This holds also for the rate of C_{2+} formation (Fig. 2.14). These observations suggest that in the initial state of the reaction the selective activation of methane towards the formation of C_{2+} hydrocarbons is directly linked with the consumption of oxygen.

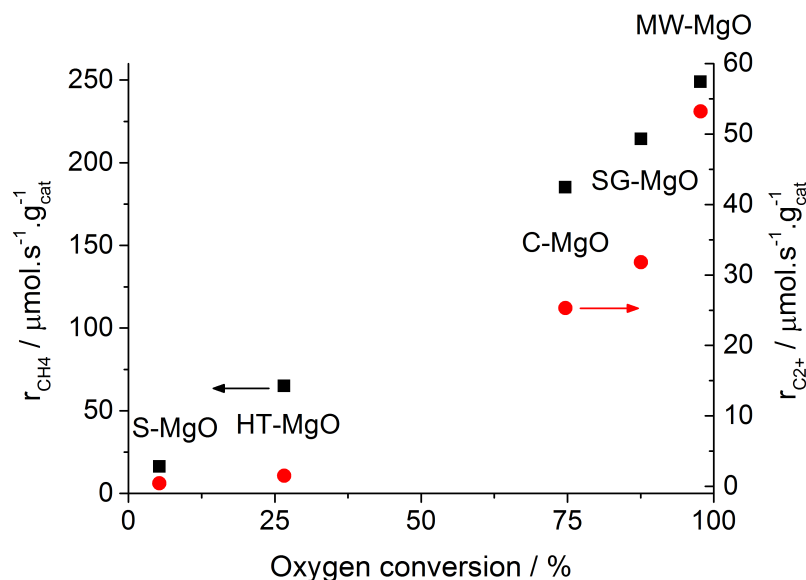
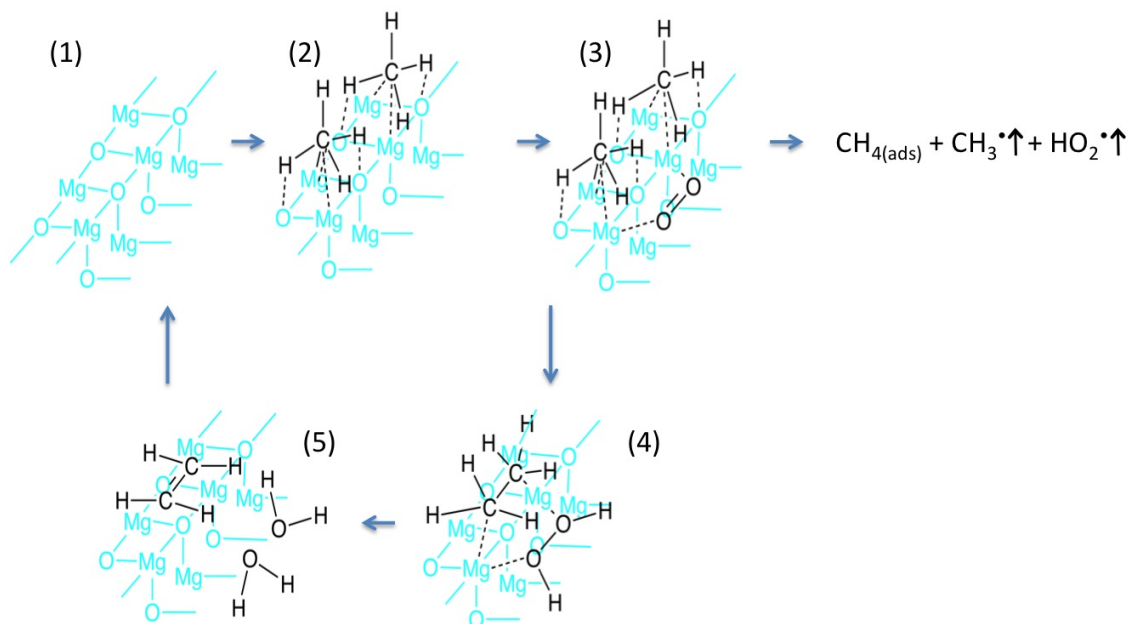


Figure 2.14: Effect of oxygen conversion on the rate of methane conversion and C_{2+} formation at time $t=0$ h. For reaction conditions, see Table 3

The experimentally observed fact that the oxygen partial pressure has a significant influence



Scheme 2.1: Proposed reaction mechanism of the formation of C₂₊ products in the oxidative coupling of methane over pure, freshly dehydroxylated MgO catalysts.

on the reaction rate indicates that methane and oxygen activation are strongly correlated. Therefore, we postulate a model for C₂₊ formation on the surface of pure, nano-structured, and dehydroxylated MgO that differs from the general picture of an Eley-Rideal mechanism, which involves activated O⁻ species adsorbed on the surface (which have so far not been verified experimentally under reaction conditions) and methane reacting from the gas phase. We assume that methane molecules are polarized by adsorption on MgO. These weakly adsorbed CH₄ molecules undergo a concerted reaction with weakly coadsorbed oxygen as illustrated in Scheme 1. On the surface of the fresh, dehydroxylated catalyst, many steps occur (1). Two methane molecules adsorb simultaneously at such a step (2). At the same time, an oxygen molecule approaches the surface close to the adsorbed methane molecules and is polarized as well (3). Next, in a concerted process, one hydrogen atom is abstracted from each of the methane molecules by oxygen forming at the same time hydrogen peroxide and ethane adsorbed at the MgO surface by creating two O-H and one

C-C bond (4). Hydrogen peroxide is able to oxidize directly the formed ethane resulting in ethylene and water (5). Finally ethylene and water desorb leaving a clean MgO surface (1). Alternatively, a methyl radical can be formed in step (3) by interaction of an adsorbed oxygen molecule with only one methane molecule, resulting in the formation of an O_2^- radical and a proton, which can combine to perhydroxyl radicals HO_2^- that may contribute together with the methyl radical to the gas phase chemistry.

The mechanistic concept proposed in Scheme 1 provides an explanation for the high reaction temperatures that are required, which is, apparently, in conflict with the observation that methane can be activated already at room temperature on the surface of MgO. [58] Perhydroxyl radicals are precursors for the formation of hydroxyl groups and water, and water itself may hydroxylate MgO, which may lead to deactivation of the MgO catalysts by sintering. Once the surface is covered with adsorbed hydroxyl groups, methane cannot adsorb anymore, unless high reaction temperatures are applied to assure a partially dehydroxylated surface under reaction conditions. In addition, Ito et al. reported that methyl radicals from the gas phase could react with surface oxygen under formation of strongly bonded methoxide species. Lunsford et al. confirmed that the sticking coefficient of methyl radicals on metal oxide surfaces drastically increase in the presence of oxygen in the gas phase due to the formation of methoxide ions. [80] Methoxide species can be transformed into carbonates at room temperature and decompose only at high temperature ($T > 700$ K) to produce either syngas or carbon dioxide and water.

There are several common characteristics between the reactivity in the OCM reaction on the fresh catalyst at time $t=0$ and the kinetics at steady state. The most important similarity is the strong correlation between methane consumption and oxygen conversion (Fig. 2.14, Table 2.3). High methane conversion is accompanied by high oxygen consumption and, consequently, high C_{2+} selectivity. The same correlation is observed between the $\text{C}_2\text{H}_4/\text{C}_2\text{H}_6$ and CO_2/CO ratios and the activity (Fig. 2.3). Several arguments support the surface mediated ethylene formation mechanism as proposed in Scheme 1, casting the commonly accepted Eley-Rideal-type mechanism involving O^- species over Li/MgO into doubt. These experimental observations are the following:

- The observation that ethane formation is rather independent of the contact time, but ethylene selectivity increases with increasing contact time (Fig. 2.6, Figs. S 2.2- S 2.5) excludes that a consecutive mechanism occurs (formation of ethylene by oxidative dehydrogenation of desorbed and re-adsorbed ethane), and implies that two different mechanisms occur in parallel: (i) methane reacts according to Scheme 1 preferentially to ethylene; (ii) However, during step 3, a methyl radical can be formed by intermolecular charge transfer between a polarized adsorbed methane molecule

on the surface and only one oxygen molecule forming a methyl radical, a superoxide species, and a proton. The methyl radical desorb than to the gas phase. In this case, ethane is formed through gas phase coupling of two methyl radicals in the classical way. The latter process does not depend on the contact time or only in a limited manner.

- The surface mediated coupling mechanism proposed in Scheme 1 explains also the formation of propene and propane. At longer contact times (higher conversions), a third methane molecule has time to adsorb near the ethylene (or ethane, resp.) *in statu nascendi* and form a C-C bond with the C₂ intermediate through further oxidation by reaction of another oxygen molecule with this intermediate. (Fig. 2.7 B)
- A concerted formation of C₂₊ hydrocarbons is further supported by the comparison between the OCM reactivity over MgO and SiC. Over SiC at very low conversions, C₂H₆ is formed selectively and further oxidation is prevented, since oxygen activation is difficult or impossible on SiC. At higher conversion, mainly pyrolysis of C₂H₆ occurs. In contrast, over MgO, the catalytic surface facilitates oxygen activation. At low conversion, pyrolysis of the desorbed reaction product C₂H₆ in the gas phase predominates (mainly CO as product), while at higher conversion, the surface mediated reaction prevails (more C₂H₄ and CO₂ in the products) and the contribution of C₂H₆ pyrolysis decreases.
- The oxidative dehydrogenation of auxiliary ethane added to the OCM feed does not follow the reactivity patterns of OCM indicating that ethylene is not a consecutive product of desorbed and re-adsorbed ethane. (Fig. 2.11 B).
- Addition of CO₂ has no poisoning effect. This indicates that point defects are not responsible for methane activation since CO₂ forms rapidly CO₂⁻ or CO₃⁻ in contact with V or F centers. It also indicates that the corners that represent the most basic centers on the surface are not involved in the activation of methane since these sites form also rapidly carbonates in the presence of CO₂.
- The low or zero apparent reaction order toward methane is in contradiction to the abstraction of a hydrogen atom by an O⁻ center and a Eley-Rideal-type mechanism. In the case of pure MgO catalysts the limiting steps appears to be the activation of oxygen, *i.e.* the formation of perhydroxyl radicals.

With the reaction mechanism presented in Scheme 1 we establish a hypothesis that is based on the analysis of the kinetic data, and electron microscopy, which shows that the most reactive catalysts exhibit small cubic primary particles terminated by {100} planes

with steps on their surface. Since it is energetically not probable that methane adsorbs on plane $\{100\}$ terrace sites and since we ruled out point defects as active centers, the OCM reaction probably takes place on steps present on freshly activated, dehydroxylated MgO $\{100\}$ surfaces. The nature of these catalytically active morphological defects will be analyzed by spectroscopic techniques and described in detail in Part II of this work.

2.5 Conclusion

At this point, we postulate that two different mechanisms occur in the oxidative coupling of methane over MgO catalysts: (i) The surface mediated coupling characterized by high methane conversion and high C_2H_4 selectivity; and (ii) The gas phase coupling involving gas phase combination of methyl radicals to C_2H_6 and the subsequent pyrolysis of C_2H_6 . Over fresh MgO catalysts, the surface mediated coupling mechanism is predominant. During the reaction, the primary catalyst particles sinter and the amount of active site decreases drastically, which is reflected in catalyst deactivation.. While the number of active sites decreases, the contribution of gas phase chemistry increases leading to decreasing selectivity and lower activity. However the surface mediated coupling can still be observed in the deactivated stationary state, especially at long contact time (high conversion).

2.6 Supporting information

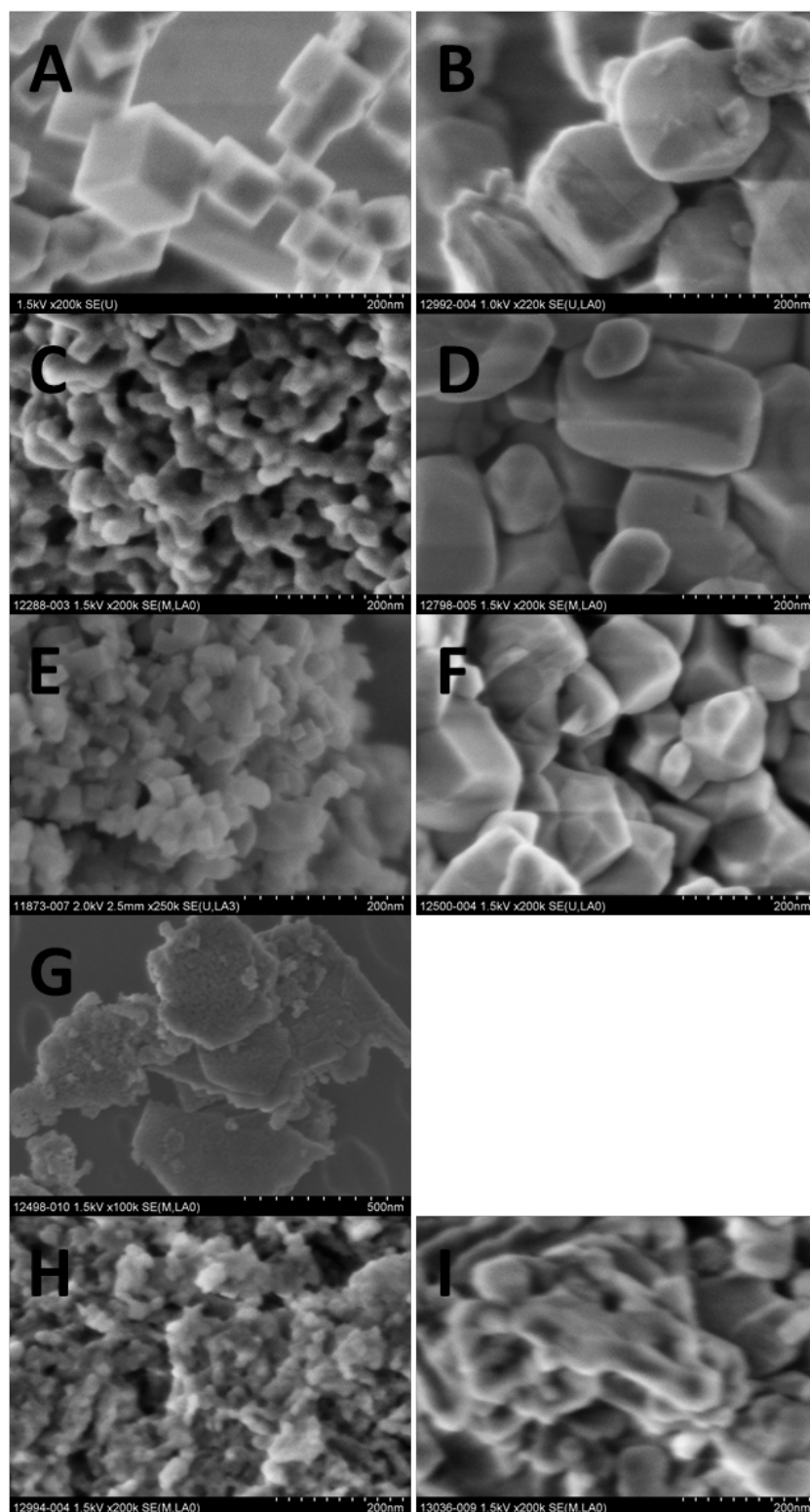


Figure S 2.1: SEM images of calcined MgO (left side) and MgO after oxidative coupling of methane for 300 hours time on stream ($\text{CH}_4/\text{O}_2/\text{N}_2=3/1/1$, $\text{W/F}=0.15 \text{ g}\cdot\text{s}\cdot\text{ml}^{-1}$, $T=1073 \text{ K}$). From top to bottom: S-MgO (A,B), C-MgO (C,D), SG-MgO (E,F), HT-MgO (G), and MW-MgO (H,I).

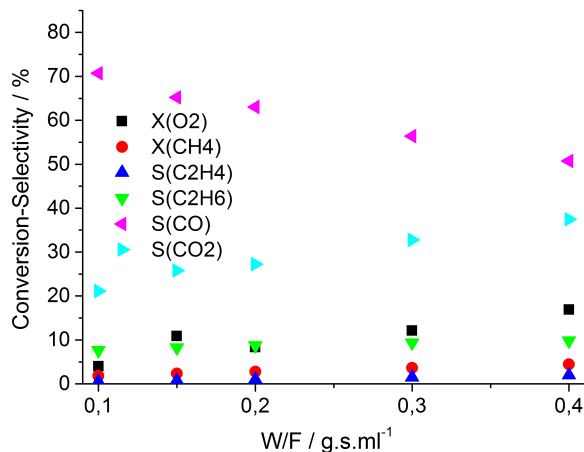


Figure S 2.2: Conversion and selectivity for S-MgO as a function of the contact time at T=1023 K, using a catalyst mass of $m_{cat}=150$ mg, and a feed composition of CH₄/O₂/N₂=3/1/1.

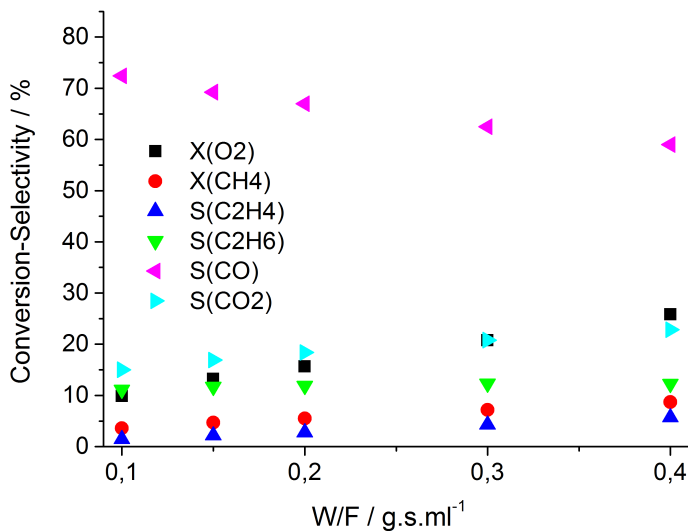


Figure S 2.3: Conversion and selectivity for SG-MgO as a function of the contact time at T=1023 K, using a catalyst mass of $m_{cat}=150$ mg, and a feed composition of CH₄/O₂/N₂=3/1/1.

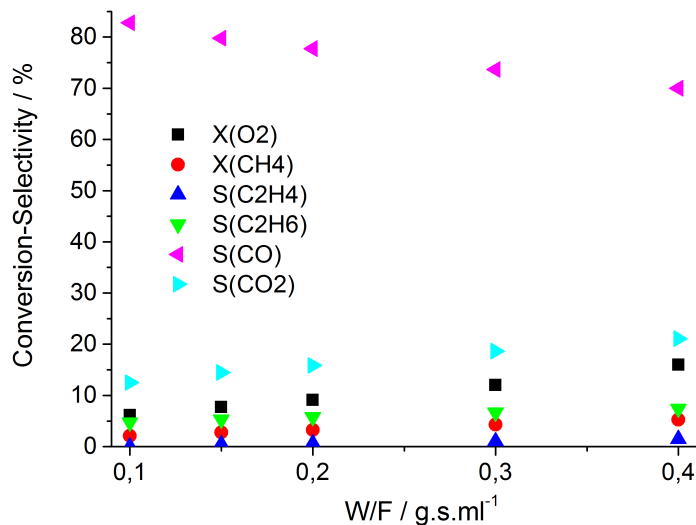


Figure S 2.4: Conversion and selectivity for HT-MgO as a function of the contact time at $T=1023$ K, using a catalyst mass of $m_{cat}=150$ mg, and a feed composition of $CH_4/O_2/N_2=3/1/1$.

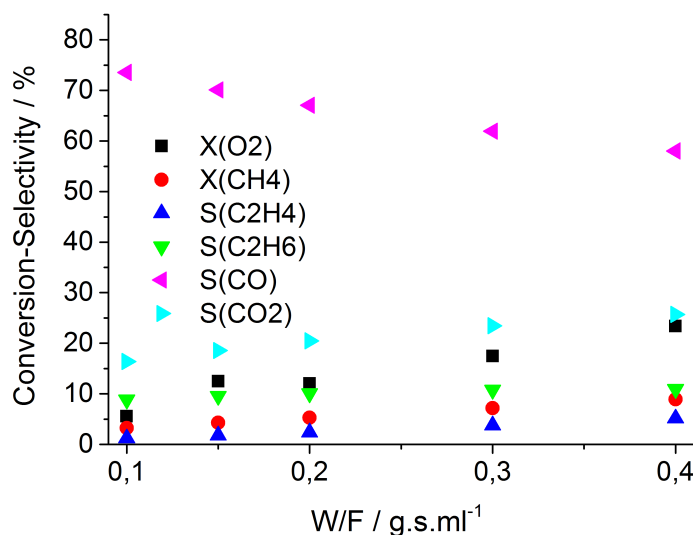
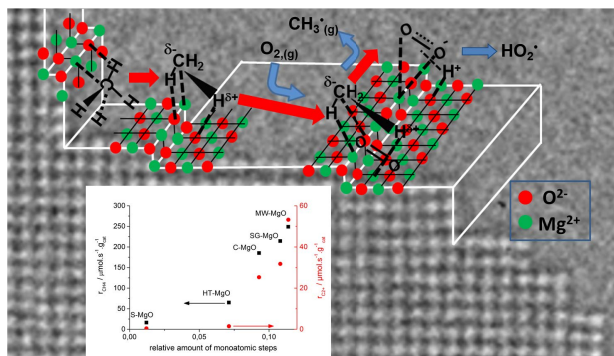


Figure S 2.5: Conversion and selectivity for MW-MgO as a function of the contact time at $T=1023$ K, using a catalyst mass of $m_{cat}=150$ mg, and a feed composition of $CH_4/O_2/N_2=3/1/1$.

3. Structure sensitivity of the oxidative activation of methane over MgO model catalysts: II. Nature of active sites and reaction mechanism ²

Pierre Schwach, Neil Hamilton, Lukas Thum, Thomas Lunkenbeim, Maik Eichelbaum, Robert Schlögl, Annette Trunschke



Abstract: A series of pure, nano-structured magnesium oxides prepared by different synthesis techniques that show different initial, but similar steady state activity in the oxidative coupling of methane (OCM) [55] has been studied by FTIR, and photoluminescence spectroscopy in the dehydroxylated state before the reaction and after catalysis. The abundance of structural defects, in particular mono-atomic steps, on the dehydroxylated MgO surface characterized by a band in the infrared spectrum of

adsorbed CO at 2146 cm^{-1} and Lewis acid/base pairs probed by co-adsorption of CO and CH_4 correlate with the initial rates of both methane consumption and C_{2+} hydrocarbon formation. Infrared spectroscopy evidences strong polarization of C-H bonds due to adsorption of methane on dehydroxylated MgO surfaces that contain a high number of mono-atomic steps. It is postulated that these sites effectively promote intermolecular charge transfer between adsorbed methane and weakly adsorbed oxygen that leads to the dissociation of one C-H bond in the methane molecule and simultaneous formation

²The following chapter is adapted from [56]

of a superoxide species. Heterolytic splitting of C-H bonds in the presence of oxygen at the surface of dehydroxylated MgO already at room temperature has been proven by the appearance of an EPR signal associated with superoxide species that are located in close vicinity to a proton. With time on stream, MgO sinters and loses activity. The deactivation process involves the depletion of mono-atomic steps and the reconstruction of the MgO termination under formation of polar and faceted surfaces.

Keywords: MgO; oxidative coupling; methane; infrared; photoluminescence; EPR; CO adsorption; defects; reaction mechanism.

Acknowledgement: This work was conducted in the framework of the COE UniCat (www.unicat.tu-berlin.de) of the German Science Foundation. The authors thank Jutta Krhnert, Dr. Maik Eichelbaum and Dr. Kazuhiko Amakawa for the discussion and their help with the conduction of experiments.

3.1 Introduction

Activation of C-H bonds in the chemically rather inert methane molecule is an academically challenging goal with prospective industrial significance in view of the demands to make new resources, like natural gas, accessible for the manufacture of base chemicals and intermediates. In a kinetic study, [55] we investigated the oxidative coupling of methane (OCM) over pure magnesium oxide involving five differently prepared model catalysts that differ in particular in the nanostructure of the surface. The performance of dehydroxylated MgO at the beginning of the reaction (at $t=0$) and the kinetics of catalyst deactivation strongly depend on initial particle morphology and surface texture, whereas similar catalyst properties are finally approached in the stationary state. The MgO inherent steady-state activity is, however, rather low. [55] Therefore, it appears desirable to identify the nature of the highly active surface sites on the surface of freshly dehydroxylated MgO and to stabilize this productive state of the catalyst. Tuning the catalyst performance using rational design approaches also requires knowledge about the deactivation mechanism to decide whether stabilization strategies may have any reasonable prospects.

The kinetic investigation of MgO in OCM (Part I of this work) [55] implies a dynamic change of the reaction mechanism(s) with time on stream. Electron microscopy indicates an impact of structural defects on the surface of MgO on reactivity, and evidences significant changes in morphology and termination of the primary catalyst particles with time. [55] Hence, the current part of the work (Part II) is devoted to the characterization of type and relative abundance of structural defects, i.e., coordinatively unsaturated

sites, at the surface of freshly dehydroxylated MgO prepared by different synthesis techniques. FTIR spectroscopy of adsorbed probe molecules, [43, 81] photoluminescence, and EPR spectroscopy [37, 45, 82, 83] have been proven beneficial in the analysis of MgO, and have been applied in the present investigation. The results of the spectroscopic analysis will be linked to the kinetic data acquired in Part I. [55] Based on sound spectroscopic evidence we postulate that weakly adsorbed methane and oxygen undergo a concerted reaction mechanism that involves direct electron transfer from a C-H bond of the methane to the oxygen molecule. The dehydroxylated MgO surface assists the polarization of the methane molecule by providing highly specific adsorption sites at mono-atomic steps and the underlying terrace that facilitates the reaction of methane with weakly adsorbed oxygen effectively. These sites, however, disappear with time on stream under reaction conditions of oxidative methane coupling. Possible mechanistic scenarios in the deactivated state of MgO under steady state conditions will be discussed.

3.2 Experimental

3.2.1 Catalysts and chemicals

The present study was performed on the same catalysts that have been analyzed in the kinetic investigation in Part I [55] including commercially available ultra pure MgO from Alfa Aesar (C-MgO), hydrothermally treated C-MgO applying ambient pressure (HT-MgO) or elevated pressure using a microwave autoclave (MW-MgO), MgO prepared by sol-gel synthesis (SG-MgO), and MgO prepared by combustion of metallic Mg in air (S-MgO). The synthesis methods and the microstructural properties of the catalysts determined by nitrogen adsorption, X-ray diffraction, and electron microscopy have been described in detail in Part I. [55]

The purity of nitrogen, argon, and oxygen (Westfalen AG) used for spectroscopic characterization of the catalysts was 99.999 %. Methane and CO for the FTIR experiments (purity 99.999 %) were delivered by Messer. Methane-d₄ (purity 99.98 %) was purchased by Sigma-Aldrich.

3.2.2 Infrared spectroscopy

FTIRS measurements were carried out using a Perkin-Elmer Spectrum 100 spectrometer equipped with a MCT detector. The spectra were recorded at a resolution of 4 cm⁻¹ accumulating 64 scans. Self-supported wafers were obtained by pressing the powdered catalysts under a pressure of 123 MPa. The wafers were transferred into an IR cell that is connected to a vacuum system, which allows to achieve a residual pressure of ca. $1 \cdot 10^{-5}$ Pa. Prior to the adsorption of gases, the catalysts were heated under dynamic vacuum at

1128 K (heating rate $10\text{ K} \cdot \text{min}^{-1}$) for 6 h. For low-temperature adsorption experiments, the sample was subsequently cooled in vacuum to room temperature. Then, the sample chamber was charged with 200 Pa partial pressure of He used as heat transfer agent and cooled to 77 K with liquid nitrogen. At first, a background spectrum was recorded in 200 Pa of He by removing the wafer from the beam. This spectrum deals as background for the spectrum of the pure, freshly pretreated catalyst. The adsorption measurements were performed in the following order: (1) addition of CH_4 at various pressures up to an equilibrium pressure of 200 Pa CH_4 (total pressure 400 Pa $\text{CH}_4 + \text{He}$) (2) evacuation at 77 K until the baseline was fully recovered; (3) addition of 200 Pa He and stepwise adsorption of CO up to partial pressure of 200 Pa (total pressure 400 Pa $\text{CO} + \text{He}$); (4) subsequent adsorption of CH_4 up to partial pressure of 200 Pa (total pressure 600 Pa $\text{CO} + \text{CH}_4 + \text{He}$). Difference spectra were obtained through subtraction of the absorbance spectrum of the catalyst in 200 Pa He from the absorbance spectrum of the sample in presence of the gases. All presented spectra have been normalized to the post-measurement areal density of the sample wafer.

3.2.3 EPR spectroscopy

Continuous wave (c.w.) X-band EPR spectra were recorded at liquid nitrogen temperature on a Bruker ESP 300 E spectrometer equipped with an X-band microwave bridge Bruker ER 042 MRH E. A Bruker ER 4116 DM resonator operating in the TE 102 mode ($\nu \sim 9.5\text{ GHz}$) was used. The spectra were recorded with a modulation frequency of 100 kHz and a microwave power of 2 mW. The frequency and g values were calibrated using the ^{52}Cr line at $g=1.9796$ of Cr^{3+} -doped MgO as internal standard placed inside the resonator. The catalyst samples were filled in a quartz cell equipped with Teflon Duran® valves and connected to a vacuum system that allows the dosing of gases. Before EPR measurements, the MgO catalysts were activated at 1073 K under dynamic vacuum ($10^{-4} - 10^{-5}\text{ Pa}$) for 6 hours. Methane ($p=1 \cdot 10^4\text{ Pa}$) and oxygen ($p=5000\text{ Pa}$) were subsequently dosed at room temperature and equilibrated for 30 min. Then, the cell was evacuated, the Teflon Duran® valves were closed, and the evacuated cell was put into the EPR resonator equipped with a quartz dewar vessel containing liquid N_2 to cool the sample to 77 K and perform the EPR measurement. EPR spectra were simulated using the Matlab® implementation Easyspin [84] in order to obtain a best fit for g-tensors and hyperfine coupling constants.

3.2.4 Diffuse reflectance spectroscopy

The *in situ* UV-VIS experiments were performed in the range between 200 and 800 nm using a Perkin Elmer Lambda 650 spectrometer equipped with a diffuse reflectance accessory (Praying Mantis, Harrick) complete with an environmental chamber attachment (Harrick

HVC-VUV-4) using Spectralon® as white standard. The catalysts were pretreated in situ at 923 K for 30 min under vacuum (lower than 10^{-3} Pa). Subsequently, the chamber was cooled in dynamic vacuum and the spectra were recorded at 313 K.

3.2.5 Electron microscopy

High resolution transmission electron microscopy (HRTEM) images were recorded on a Cs-corrected FEI Titan 80-300 at an acceleration voltage of 300 kV

3.2.6 Photoluminescence

Photoluminescence spectra were recorded on a Perkin-Elmer LS-55 spectrometer at room temperature under dynamic vacuum, at a pressure lower than $1 \cdot 10^4$ Pa. The spectrometer was equipped with a red sensitive photomultiplier R928 from Hamamatsu Photonics that allows detection of emissions in the range between 200 and 900 nm. The spectra were recorded with an emission and excitation slit opening of 2.5 nm, a scanning speed of 20 nm/min and an emission filter of 350 nm in order to suppress direct light scattering from excitation. The catalyst powder was located in a flat SUPRASIL® quartz cell from Hellma-Analytics with a path length of 2 mm. The cell was connected to a vacuum and gas dosing line. Before measurement the catalysts were heated at 1073 K in dynamic vacuum for 6 hours. The samples before catalytic testing were measured as powder and the samples after catalysis were pressed into pellets of the size of the photoluminescence cell.

3.3 Results

The magnesium oxide catalysts studied in oxidative coupling of methane in Part I differ in their morphology. [55] The trend in specific surface area is not directly related to the mean crystallite size determined by XRD indicating that surface texturing contributes substantially to the surface area measured by nitrogen adsorption. However, sintering phenomena are observed for all catalysts after use in the oxidative coupling of methane at 1073 K for approximately 300 hours time on stream. The domain size determined by XRD increases substantially except in the case of S-MgO, that shows a slight size reduction of the initially very large particles. [55] In agreement with a similar size of the coherently scattering domains in the used catalysts, the specific surface area of all used catalysts is similar and varies between 7 and $12 \text{ m}^2 \cdot \text{g}^{-1}$. Sintering is also visible by TEM and SEM. [55] After catalysis, the morphology of the primary particles is much more rounded. The characteristic sharp edges and corners of the cubic structure have disappeared and pseudo {110} and {111} faces consisting of stepped edges between {100} planes and numerous corners have formed. The sintering is accompanied by catalyst deactivation. With the

aim to learn more about potential active sites on the surface of MgO and their depletion under reaction conditions, transmission infrared spectroscopy was used. CO adsorption at 77 K provides information on coordinatively unsaturated Mg^{2+} adsorption sites (Lewis acid sites), while adsorption of methane probes both acidic (cationic) and basic (anionic) sites. Co-adsorption of both methane and carbon monoxide reveals the relative abundance of each site.

3.3.1 IR spectroscopy

3.3.1.1 Calcined MgO

3.3.1.1.1 CO adsorption Adsorption of carbon monoxide at low temperatures results in the appearance of carbonyl bands that are shifted to higher energy compared to the C-O stretching mode of the free CO molecule at 2143 cm^{-1} due to formation of σ -donor bonds via the carbon atom of the CO molecule to coordinatively unsaturated surface cations. [85] Additional bands arising below 2000 cm^{-1} are attributed to carbonite anions or similar polymeric structures reflecting the strong basic character of the MgO surface. [86,87] These species are formed by interaction of the CO molecule with coordinatively unsaturated oxygen ions. [86]

Fig. 3.1 exemplarily presents infrared spectra of CO adsorbed on C-MgO at 77 K and shows the development of C=O stretching bands as a function of increasing CO pressure. At this low adsorption temperature, only negligible traces of carbonite species were observed. In the following, the spectra are, therefore, presented and analyzed exclusively in the range between 2100 and 2200 cm^{-1} . At low pressures, *i.e.* up to ca. 7 Pa, a broad feature due to superimposed contributions of bands at 2146 , 2156 , and 2164 cm^{-1} is discernible (Fig. 3.1B). With increasing equilibrium pressure of CO, the bands at 2146 cm^{-1} and 2164 cm^{-1} are more and more obscured by the most intense band that shifts from 2157 cm^{-1} to 2152 cm^{-1} .

Spoto *et al.* [43] discussed two sets of bands located at 2150 - 2145 cm^{-1} , and 2180 - 2160 cm^{-1} formed upon adsorption of CO on the MgO surface at 60 K. The 2150 - 2145 cm^{-1} bands exhibit a maximum located at ca. 2150 cm^{-1} with a shoulder at 2140 cm^{-1} , which are similar to the features observed at 2156 and 2146 cm^{-1} in Fig. 3.1B. Such signals are reported to be strongly attenuated as the MgO crystals become more ordered and are found to be completely absent from spectra of nearly perfect well-ordered MgO cubelets prepared by combustion of metallic Mg (smoke synthesis). [43] Upon adsorption, the CO stretching modes of adsorbed CO are observed to shift to higher wavenumber positions relative to gas phase CO, which is a result of the Stark effect associated with the positive electric field of the adsorptive cation. When no d-electrons are involved, the shift is proportional to the

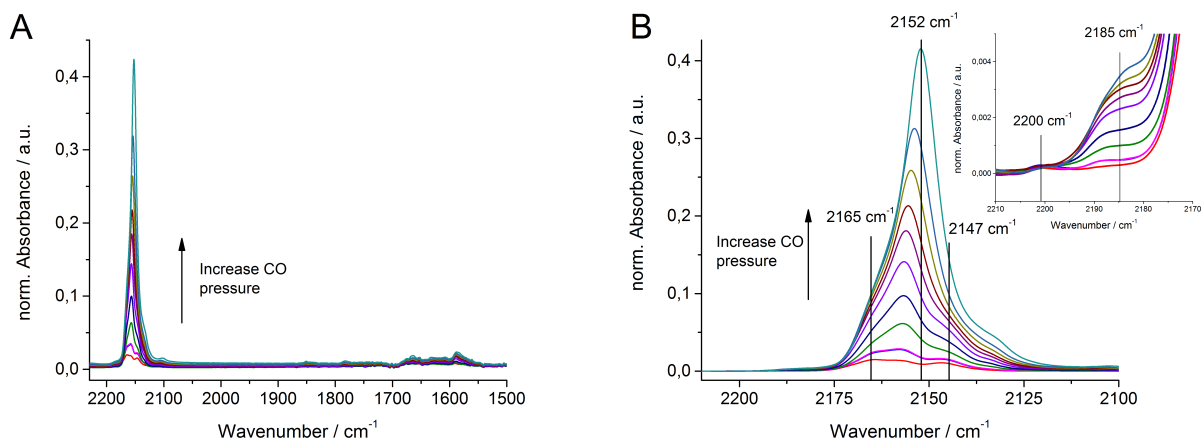


Figure 3.1: IR spectra of CO adsorbed on C-MgO at $T=77\text{K}$ with increasing pressure from $p=2.9\text{ Pa}$ to $p=210\text{ Pa}$. (A) Range of carbonyl and carbonite vibrations (B) Evolution of carbonyl bands as a function of the CO equilibrium pressure. Inset: Enlarged representation of carbonyl bands assigned to CO adsorbed on 3-fold coordinated Mg^{2+} cations.

strength of the electric field sensed by CO. [88,89] As a reasonable first approximation, the effective electric field experienced by CO adsorbed on a cationic site is a result of the contribution of the cation and the anions of the first coordination sphere. Thus, when the number of anions surrounding a Mg^{2+} adsorption site decreases, the negative contribution to the electric field decreases and, hence, the effective positive field experienced by the adsorbed CO increases.

On this basis, the signal located at 2146 cm^{-1} should be assigned to a CO species experiencing only a weak positive field. However, on the basis of adsorption enthalpy and the fact that this band is present at very low CO pressure, Spoto *et al.* assigned this band to CO bonded to $\text{Mg}_{4\text{C}}^{2+}$ - $\text{Mg}_{5\text{C}}^{2+}$ pairs at mono-atomic step edges, either through both the carbon end coordinated to a $\text{Mg}_{4\text{C}}^{2+}$ site at the edge and the oxygen end coordinated to a $\text{Mg}_{5\text{C}}^{2+}$ site located at the subjacent terrace or through the carbon end only as bridged species. [43] A computational study by Soave *et al.* indicates that CO coordination via carbon only in form of a bridged complex is more likely. [90] Trionfetti *et al.* observed this band also after CO adsorption on Li/MgO catalysts, but with increasing Li content the contribution of the step sites decreases, [91] which is in agreement of the ironing effect of alkali additives. [32]

The band located at $2157\text{-}2149\text{ cm}^{-1}$ has previously been assigned to $\text{Mg}_{5\text{C}}^{2+}$ on (100) terrace

sites. [43] Note that the feature observed at ca. 2146 cm^{-1} in Fig. 3.1 is swallowed up and finally completely obscured by the band associated with terrace sites located at 2158 cm^{-1} at higher equilibrium pressures. This observation is consistent with the findings of Spoto *et al.*, [43] who interpreted this behavior as CO adsorbed to pairs of Mg^{2+} cations at low pressures in bridged configuration, while at higher pressure this configuration is displaced by a 1:1 ratio between Mg^{2+} centres and adsorbed CO. Features located in the range between $2180\text{--}2160\text{ cm}^{-1}$ are typically assigned to terminal CO adsorbed on Mg_{4C}^{2+} centres, [43,91] which occur at the surface as edges either of mono-atomic or multi-atomic steps, respectively. We therefore assign the band located at 2164 cm^{-1} in Fig. 3.1 to CO adsorbed on edge sites. Spoto *et al.* reported a band located at $2205\text{--}2200\text{ cm}^{-1}$ at low CO pressure that shows a red shift towards 2185 cm^{-1} at higher CO pressure. [43] They tentatively assigned this band to CO adsorbed on Mg_{3C}^{2+} species (corners). A shoulder around 2185 cm^{-1} was detected with all MgO samples, however the band at 2200 cm^{-1} was observed only for C-, SG-, and MW-MgO (for instance see inset in Fig. 3.1A).

In summary, the spectra presented in Fig. 3.1 are consistent with nano-structured MgO that exposes coordinatively unsaturated Mg^{2+} sites in fivefold, fourfold, and threefold coordination at the surface. The fourfold coordinated Mg cations comprise edges at mono-atomic as well as multi-atomic steps.

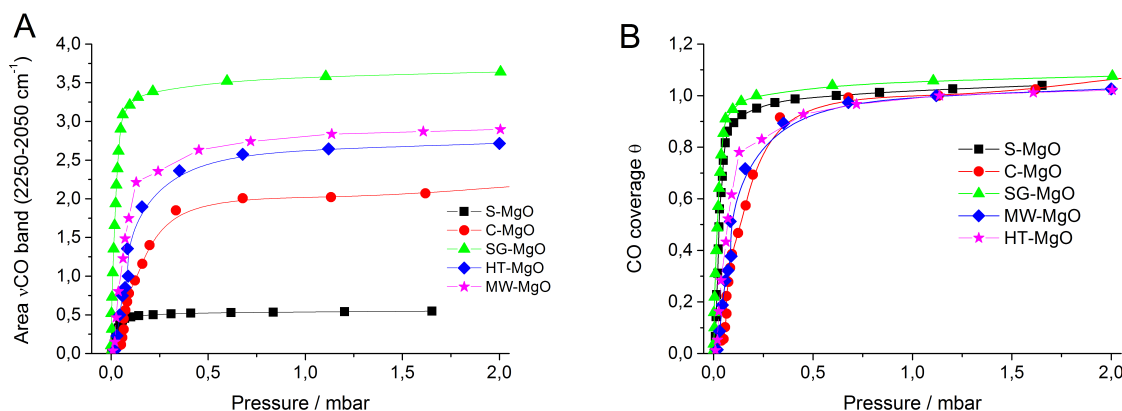


Figure 3.2: Integrated area of the peaks of adsorbed CO as a function of the equilibrium CO pressure at 77 K (A) and the derived adsorption isotherms (B). The integrated area was determined using spectra normalized with respect to the mass of the wafer.

Fig. 3.2 presents CO adsorption isotherms determined by plotting the integrated area of the entire ν_{CO} band as a function of the CO equilibrium pressure at 77 K. The differences in the maximum integrated area reflect both the surface area and surface nanostructure

of the differently prepared MgO catalysts. Assuming that the knee in each isotherm (Fig. 3.2A) corresponds to monolayer coverage, *i.e.* $\theta=1$, the y-axis on each isotherm may be replaced by surface coverage, θ (Fig. 3.2B). In this manner, the equilibrium pressure of CO required to achieve a specific surface coverage was determined. Since, as established by Fig. 3.1B, the coordination of adsorbed CO is dependent on surface coverage, this procedure allows a more reliable comparison of the differently prepared MgO catalysts.

In Fig. 3.3 the spectra of adsorbed CO at $\theta=0.15$ are compared for all catalysts. At such a low coverage we expect that coupling effects between neighboring CO molecules are negligible. The difference in the total peak area follows the trend of the specific surface area. For example, S-MgO exhibits the lowest total integrated intensity and has the lowest surface area of only $11 \text{ m}^2 \cdot \text{g}^{-1}$, whereas MW-MgO, which exhibits the largest intensity, has the highest surface area of $111 \text{ m}^2 \cdot \text{g}^{-1}$ indicating that the overall intensity is not strongly affected by the relative abundance of different Mg^{2+} sites exposed at the catalyst surface, *i.e.*, the extinction coefficients of CO adsorbed on different Mg^{2+} sites seem to be similar.

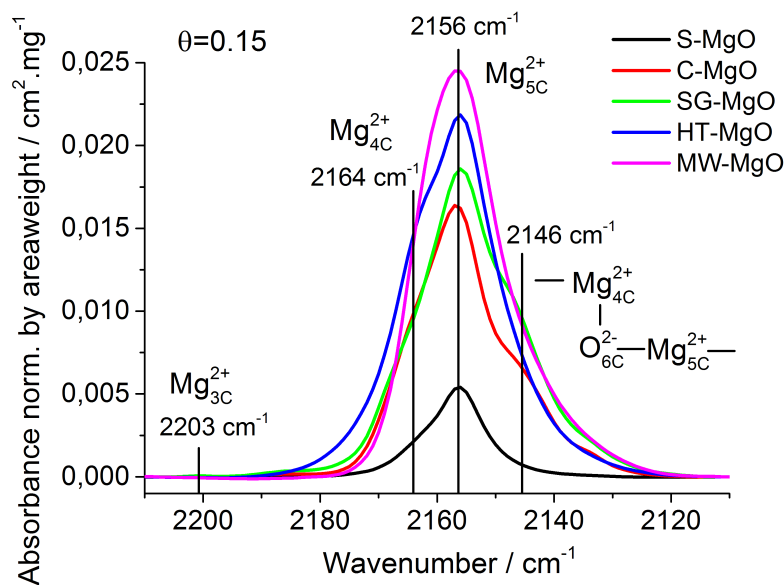


Figure 3.3: Spectra of CO adsorbed on MgO at $T=77\text{K}$ at a coverage of $\theta = 0.15$

The MgO sample prepared by smoke synthesis, S-MgO, exhibits the simplest spectrum, which is dominated by a signal at 2156 cm^{-1} that is associated with $\text{Mg}_{5\text{C}}^{2+}$ terrace sites. A weak shoulder located at 2164 cm^{-1} is attributed to $\text{Mg}_{4\text{C}}^{2+}$ centres located at cubelet edges and/or multi-atomic step defects. The spectrum of CO adsorbed on commercially acquired MgO, C-MgO, exhibits generally greater intensity and is dominated by terrace sites

(2156 cm^{-1}), however the relative contribution of features associated with mono-atomic steps (2146 cm^{-1}) is enhanced with respect to S-MgO. Sol-gel prepared MgO, SG-MgO, exhibits more terrace sites and mono-atomic steps, while the contribution from edges at multi-atomic steps (2164 cm^{-1}) is similar to that of C-MgO. Hydrothermally treated MgO, HT-MgO, features a major contribution from terrace sites (2156 cm^{-1}) with a visible shoulder located at 2164 cm^{-1} due to edge sites at multi-atomic step defects. The contribution from mono-atomic step defects is reduced relative to both C-MgO and SG-MgO. Finally, MgO prepared by hydrothermal microwave post-treatment, MW-MgO, exhibits a rather broad band with a maximum located at 2156 cm^{-1} indicating the predominance of terrace sites. However, due to the width of the band the presence of signals associated with edge sites and mono-atomic step defects cannot be excluded. Indeed, inspection of the associated TEM image of MW-MgO (Fig. 3.4) indicates that edge sites are indeed present.

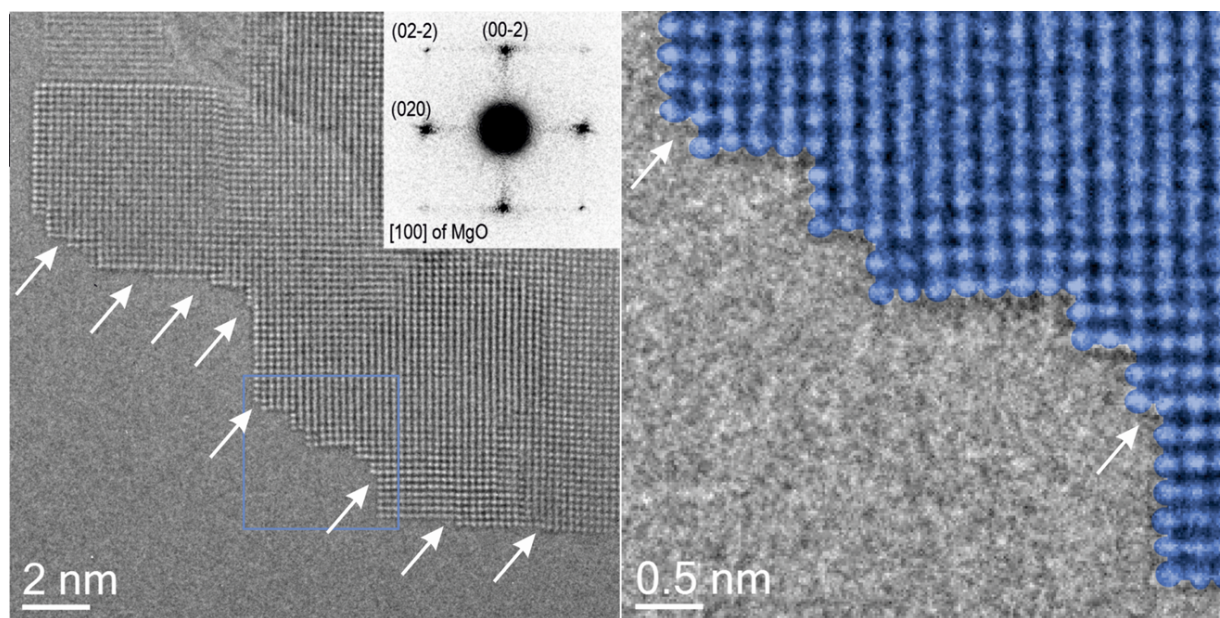


Figure 3.4: High resolution TEM images of MW-MgO viewed along [100]. The inset in (A) shows a power spectrum, which allows to identify the orientation of the MgO crystal. (B) represents a higher magnified micrograph of (A) taken at the marked region of interest. The mono-atomic steps at the surface are clearly visible and marked by arrows.

In summary, the differently prepared and freshly calcined magnesium oxides differ in the total concentration of coordinatively unsaturated Mg^{2+} surface sites at the surface. The total number of cationic sites probed by CO adsorption displays the same trend as the total surface area determined by nitrogen adsorption. More important, the relative abundance of the different types of sites differs. S-MgO, for instance, shows no mono-atomic steps, while the concentration of the latter seems to be the highest on MW-MgO.

3.3.1.1.2 Methane adsorption The IR spectrum of the free CH₄ molecule is characterized by the triply degenerate antisymmetric stretching mode ν_3 at 3020 cm⁻¹ and the twofold degenerate H-C-H deformation mode ν_4 at 1306 cm⁻¹. [81,92,93] The infrared spectrum of CH₄ adsorbed at 77 K on C-MgO (Fig. 3.5, red line) shows bands at 3003, 2896, 2827 cm⁻¹ in the region of C-H stretching vibrations and a band at 1304 cm⁻¹ in the region of deformation vibrations. The shift of 17 cm⁻¹ compared to the gas phase ν_3 mode and the appearance of a band at 2896 cm⁻¹ due to the infrared-forbidden ν_1 stretching vibration (Raman band of the free molecule at 2914 cm⁻¹) [81], indicate that the methane molecule is considerably polarized upon adsorption, which goes along with a reduction of the T_d symmetry of the molecule. However, the ν_4 deformation mode located at 1304 cm⁻¹ is practically not shifted with respect to gas phase CH₄. The ν_2 mode (Raman band of the free molecule at 1526 cm⁻¹) remains IR inactive. The band located at 2827 cm⁻¹ may be assigned to a combination mode of ν_4 and ν_2 mode. The observed bands are attributed to methane interacting with coordinatively unsaturated sites at the surface of C-MgO. Methane adsorption on regular {100} MgO terrace sites has been excluded based on theoretical and experimental studies. [81] Methane can be adsorbed on MgO in either monodentate coordination on basic Lewis sites (coordinatively unsaturated O²⁻ at corners only), or in polydentate coordination on Mg²⁺ - O²⁻ Lewis acid/base pairs at edges (as shown in Scheme 3.1). [81,92] DFT calculations support the hypothesis that methane prefers polydentate coordination at edges. [81] Li *et al.* observed two ν_1 C-H stretching modes located at 2900 and 2890 cm⁻¹, respectively, which were attributed to methane strongly adsorbed on different acid-base pairs on the surface of MgO. [92] Furthermore, adsorption of methane on these sites is supposed to be responsible for a considerable red-shift of the ν_3 mode to 3000 cm⁻¹. In contrast, methane weakly adsorbed on coordinatively unsaturated oxygen anions at corners is assumed to result in a smaller red-shift of the ν_3 mode to about 3008 cm⁻¹ without significant reduction of the symmetry of the molecule. Accordingly, the forbidden ν_1 mode remains inactive for such a surface coordination of methane. [92] We noticed that for the samples considered here the band located at ca. 2890 cm⁻¹ was not observed unless a high pressure (ca. >700 Pa) of CH₄ was admitted. At such pressures, signals associated with gas phase CH₄ are already significant indicating that the corresponding surface species is rather weakly adsorbed. Irrespective of the specific assignment, the broadness (FWHM of ν_1 is ca. 15 cm⁻¹) and the red-shifts of the observed ν_3 and ν_1 C-H stretching modes, respectively, indicate that at least two coordination complexes of adsorbed methane are present on the surface of C-MgO and that the electronic structure of the methane molecule is strongly perturbed due to adsorption at 77 K. This deduction is entirely consistent with the different Mg²⁺ environments revealed by IR spectroscopy of adsorbed CO (Figs. 3.1 and 3.3).

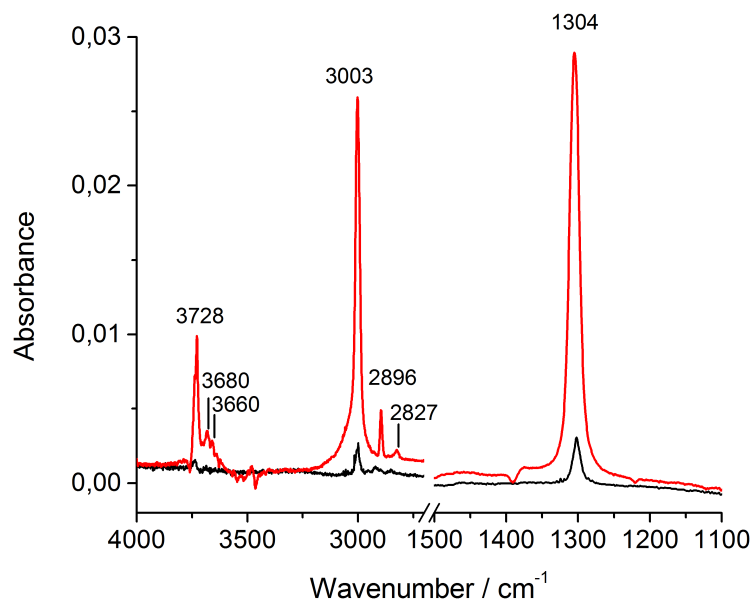
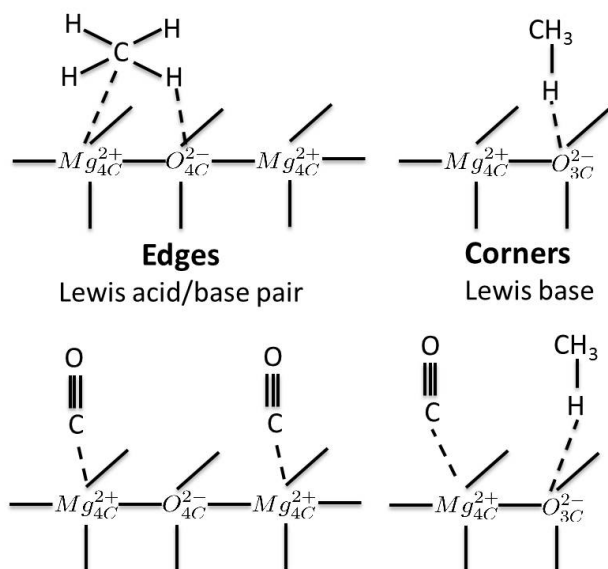


Figure 3.5: Adsorption of ca. 10 Pa methane at $T=77$ K on pretreated C-MgO (red line) and after pre-adsorption of 200 Pa CO (black line).



Scheme 3.1: Coordination of methane and CO at the MgO surface

The spectrum of adsorbed methane shows additional bands in the region of O-H stretching vibrations at 3728, 3680, and 3660 cm^{-1} (Fig. 5, red line). The wavenumbers are

characteristic of Mg-OH species in different coordination. [94] Interestingly, these bands that have to the best of our knowledge not yet been reported in the literature for methane adsorption on MgO, disappear along with the other methane bands upon evacuation at 77 K. This indicates that they are due to a very weakly bound surface species. The ν_{OH} signal could be caused by dissociative adsorption of methane, whereby new hydroxyl and methyl groups are formed on neighboring O^{2-} and Mg^{2+} sites, respectively. However the fact that the signals were completely removed by evacuation at 77 K, render this explanation rather unlikely. Therefore, these features are tentatively assigned to hydrogen-bonded moieties ($-Mg-O-H-CH_3$) present in di-hapto methane adsorption complexes. Apparently, adsorption sites on MgO are capable of polarizing the C-H bonds in such a way that not only IR inactive vibrations of CH_4 , but also discrete ν_{OH} signals due to hydrogen atoms of methane, which interact with O^{2-} sites at the MgO surface, become visible. The interaction geometry of methane with acid-base pair sites proposed by Li *et al.* [92] implies certainly an agostic interaction between C-H and the acid-base pair, which could then lead to a polarization of the adsorbed methane possibly resulting in an enhanced interaction between the neighboring basic O^{2-} and the methyl hydrogen. The fact that the $-Mg-O-H-CH_3$ features are not observed in the co-adsorption experiments, where Mg^{2+} centres are saturated by CO (Fig. 3.5, black line), indicates that they must be associated with acid-base pair sites only, because CO blocks these sites (Scheme 3.1 and discussion below).

To verify with certainty that the observed ν_{OH} signal is indeed caused by the polarization of a C-H bond and not, for example, by water impurities in methane, the adsorption of deuterated methane (CD_4) was studied by FTIR spectroscopy. Fig. 3.6 represents the infrared spectrum of CD_4 adsorbed on C-MgO at 77 K applying an equilibrium pressure of 100 Pa and after evacuation. The antisymmetric stretching mode ν_3 of free CD_4 is red shifted from 2259 cm^{-1} to 2248 cm^{-1} and the deformation mode ν_4 is shifted from 996 cm^{-1} to 992 cm^{-1} indicating polarization of the molecule like in case of CH_4 . Three new bands appear at 3234 , 3086 , and 2927 cm^{-1} (OD stretching region enlarged in Fig. 3.6B). The intensity of these bands increases with increasing CD_4 equilibrium pressure and decreases upon evacuation. In analogy to the CH_4 adsorption, we tentatively assign these bands to D-bonded OD moieties ($-Mg-O-D-CD_3$) of CD_4 adsorbed at different sites.

The absence of carbonite bands indicates that carbon monoxide interacts at 77 K only with acidic sites (Mg^{2+}). A decrease in the integrated absorbance of infrared bands of adsorbed methane in the presence of adsorbed CO compared to that in the absence of CO gives an indication of the number of Lewis acid/base pairs available for methane adsorption. As discussed above, methane adsorbs in absence of CO in a di-hapto coordination on $Mg^{2+} - O^{2-}$ acid-base pairs at edges and in a mono-hapto coordination on basic O^{2-} adsorption sites at corners. In contrast, in a co-adsorption measurement, where methane is adsorbed on the catalyst surface in the presence of pre-adsorbed CO (equal to a saturated overlayer),

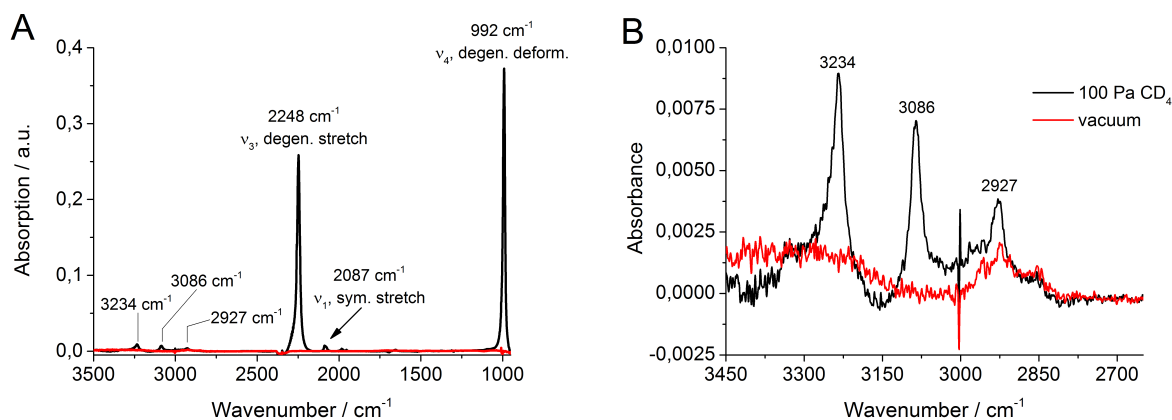


Figure 3.6: (A) Adsorption of CD_4 at $T=77\text{ K}$ at the surface of C-MgO dehydroxylated at 1073 K . (B) Enlarged representation of the spectra in the range of O-D stretching vibrations. Black line: after adsorption of 100 Pa CD_4 , red line: after evacuation up to $5 \cdot 10^{-4}\text{ Pa}$.

the band at 3000 cm^{-1} becomes less dominant allowing the observation of the weaker ν_{CH} band of methane adsorbed on basic O^{2-} sites (corners) located at 3008 cm^{-1} (Fig. 3.5). Clearly, this is due to the fact that the more basic CO molecule has occupied cationic sites, leaving only basic O^{2-} sites (corners) for methane adsorption. As shown in Fig. 3.5, also the intensity of the δ_{CH} band ν_4 located at 1304 cm^{-1} is severely diminished in the presence of an excess of CO (200 Pa , $\theta \geq 1$) due to the same reason. Thus, discrimination between cationic (acid) and anionic (basic) adsorption sites is possible by co-adsorption of CO and CH_4 . By comparing the integrated area of the ν_4 band in both the absence and presence of CO, the relative abundance of acid-base pair sites (edges) in the different MgO catalysts can be analyzed (Fig. 3.6). It becomes clear that the acid-base pairs at the edges are the predominant adsorption sites for all MgO preparations. The relative abundance of edges versus corners decreases in the following order: S-MgO = C-MgO > SG-MgO > MW-MgO > HT-MgO.

3.3.1.2 Used catalysts

In order to determine changes occurring to the catalyst surface during OCM we applied the methodology previously established for characterizing fresh catalysts to catalyst samples after several hundred hours time on stream (TOS) in the OCM reaction.

Fig. 3.8 shows a comparison of infrared spectra of CO adsorbed on commercially acquired MgO (C-MgO) before and after 300 h TOS in OCM at 1073 K . Both spectra have been

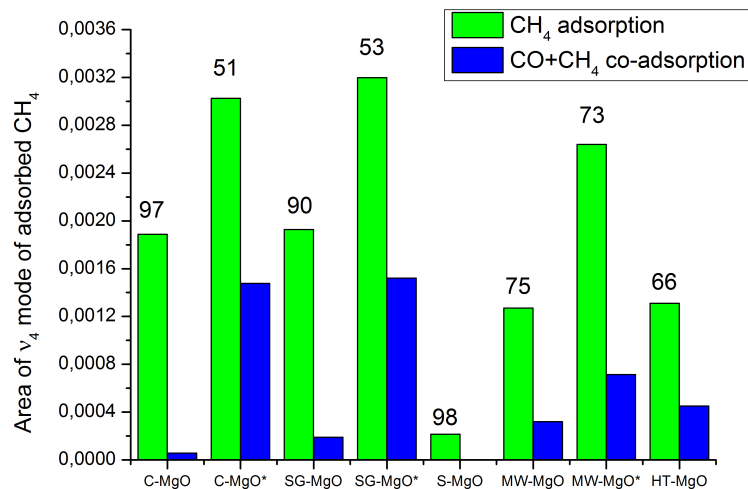


Figure 3.7: Integrated areas of the ν_4 mode of adsorbed CH_4 on outgassed MgO (green bars) and on MgO that has been pre-saturated with CO ($p_{eq} = 200$ Pa, *i.e.* $\theta=1$, blue bars) at $T=77\text{K}$. The green bars are a measure of the total number of adsorption sites of methane (di-hapto adsorption at $\text{Mg}^{2+} - \text{O}^{2-}$ acid-base pair sites at edges plus mono-hapto adsorption at basic O^{2-} sites (corners)), the blue bars indicate the number of the basic O^{2-} adsorption sites at corners only. The numbers presented on top of the bars indicate the relative content of acid-base pair sites for methane adsorption on the MgO surface in percentage.

recorded at CO coverage $\theta = 0.08$. The simplicity of the spectrum of CO adsorbed on used C-MgO is striking and indicates that the catalyst surface was significantly modified under OCM reaction conditions. The mono-atomic steps (band at 2146 cm^{-1}) have been practically disappeared. Features located at 2158 and 2164 cm^{-1} assigned to CO adsorbed on terrace and edge sites, respectively, are present, but significantly attenuated due to the reduction of the specific surface area from $19.1\text{ m}^2 \cdot \text{g}^{-1}$ in the fresh catalyst to $7.9\text{ m}^2 \cdot \text{g}^{-1}$ in the spent one. The most intense feature is observed at 2169 cm^{-1} , which corresponds to CO bound to multi-atomic step sites (edges). Two new bands for CO adsorbed at corners appear in the range between 2190 and 2210 cm^{-1} . Fig. 3.8 clearly demonstrates that OCM reaction conditions transform MgO surfaces rich in mono-atomic step sites and bridge defects into surfaces dominated by multi-atomic steps and corners.

The used catalysts generally adsorb more methane than the fresh ones (compare the green bars in Fig. 3.7). The reduction of the total specific surface area is apparently compensated by an increase in the number of defects where methane can be adsorbed and a

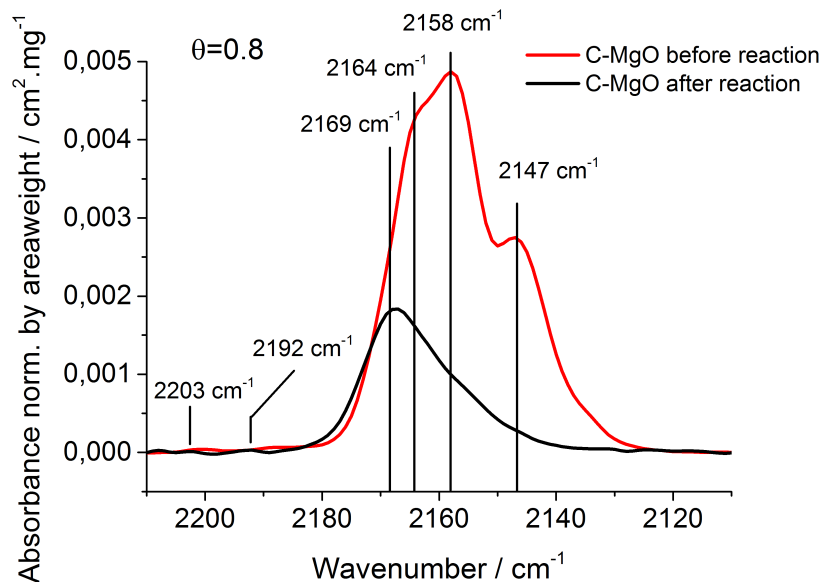


Figure 3.8: Spectra of CO adsorbed at $T=77\text{K}$ at $\theta=0.08$ on C-MgO after calcination (red line) and after application in oxidative coupling of methane (black line) under the following reaction conditions: $\text{CH}_4/\text{O}_2/\text{N}_2=3/1/1$, $W/F=0.15 \text{ g} \cdot \text{s} \cdot \text{ml}^{-1}$, $T=1073 \text{ K}$, $\text{TOS} = 300 \text{ h}$.

decrease in the fraction of terrace sites where methane does not adsorb. The fraction of acid-base pairs decreases drastically for C-MgO and SG-MgO from about 90 to about 50 %, but stays almost unchanged at about 70 % for MW-MgO. Fresh C-MgO and SG-MgO catalysts exhibit an almost ideal cubic nanostructure with well-defined structural defects present on their $\{100\}$ surfaces (see Fig. 1C-E in [55]). During the reaction, sintering of the particle causes a loss of the cubic structure and the formation of a highly defective structure, which explains the increase of corner sites, i.e. the decrease in the fraction of acid-base pairs at edges. In the case of MW-MgO, the structure of the fresh catalyst is already highly defective. Sintering during the OCM reaction leads to a decrease in the surface area and an increase in the mean particle size as determined by XRD, but the relative concentration of corners and acid-base pairs (edges) does not change.

In summary, the most striking differences between fresh and used catalysts are (i) the disappearance of mono-atomic steps, (ii) an increase in the fraction of O_{2-} corners sites, and (iii) in some cases a reduction of the relative amount of acid-base pairs (edges) indicating that substantial changes in the nature of morphological defects occur during catalysis.

3.3.2 Photoluminescence (PL) spectroscopy

Properties of morphological defects in alkaline earth oxides are of interest to the catalytic community since the mid 60s. Differences in the coordination number of surface ions modify their Madelung potential and result in changes in the local acceptor-donor (acid-base) behavior. Garrone *et al.* demonstrated based on the Levine-Mark model [95] that excitation energies reflect the local coordination number (and the Madelung potential, respectively) of surface ions of alkaline earth oxides. [19] In other words, the presence of morphological defects on the surface of alkaline earth oxides is responsible for the presence of intrinsic discrete energy levels within the band-gap, *i.e.* local acceptor-donor pairs, which can be probed by UV light. Hence, MgO was intensively investigated by diffuse reflectance spectroscopy. General consensus has been reached concerning the assignment of the absorption bands to the corresponding structural defects. [19] The UV-Vis spectrum of C-MgO reveals typical bands at 218 nm (5.69 eV) and 266 nm (4.66 eV) that are assigned to 4-fold and 3-fold coordinated oxygen atoms at edges and corners, respectively (Fig. 3.1). Light emission has also been observed for MgO powders in the UV and blue visible range after excitation with photons [96] or via electron injection from a scanning tunneling microscope tip. [97] Photoluminescence (PL) spectroscopy is, therefore, complementary used to sensitively probe defects and low-coordinated edge or corner sites (structural defects). [98] However, the interpretation of the emission spectra is not straightforward since several recombination and energy transfer phenomena may occur after the excitation. [45, 98, 99] The emission spectra depend on the energy of the light used for excitation. Generally, sets of excitation-emission ($\lambda_{exc} - \lambda_{em}$) wavelengths are provided in the literature. These couples are identified experimentally by recording emission spectra (recording the spectrum of the emitted light at a fixed excitation wavelength) and excitation spectra (changing the excitation wavelength and recording the emission at a fixed wavelength). In order to gain an improved spectral resolution and to achieve a clear determination of the excitation-emission sets, 2D photoluminescence spectroscopy was performed in the present study. Fig. 3.9 presents the 2D PL patterns of fresh and used C-MgO recorded in dynamic vacuum after annealing at 1073 K in vacuum for 6 hours. The conjugated excitation-emission ($\lambda_{exc}-\lambda_{em}$) wavelengths are summarized in Tab. 3.1 and compared with the results of a theoretical study. [45] The patterns of S-, and SG-MgO before and after catalysis are shown in the supporting information (Figs. S3.8-3.11).

Generally, five different species have been identified experimentally by one-dimensional PL spectroscopy at the surface of dehydroxylated MgO powders and assigned based on time-dependent DFT calculations; [45] Fourfold coordinated oxygen anions (O_{4C}^{2-}) at edges give rise to an excitation-emission couple at 240-380 nm. Two different species, namely 3-fold coordinated oxygen anions (O_{3C}^{2-}) at corners and O_{3C}^{2-} at kinks (corners are the crossing

points between three extended edges, whereas a kink comprises at least one short edge, *e.g.*, a kink is for example a corner at a mono-atomic step) together with O_{4C}^{2-} close to corners and kinks are characterized by the same excitation-emission wavelengths at 280-470 nm. The latter two species are distinguishable by different lifetimes. O_{3C}^{2-} at corners together with O_{4C}^{2-} close to Mg_{3C}^{2+} kinks are supposed to be responsible for an excitation-emission couple at 320-530 nm. A couple at 350-605 nm is attributed to O_{3C}^{2-} at kinks.

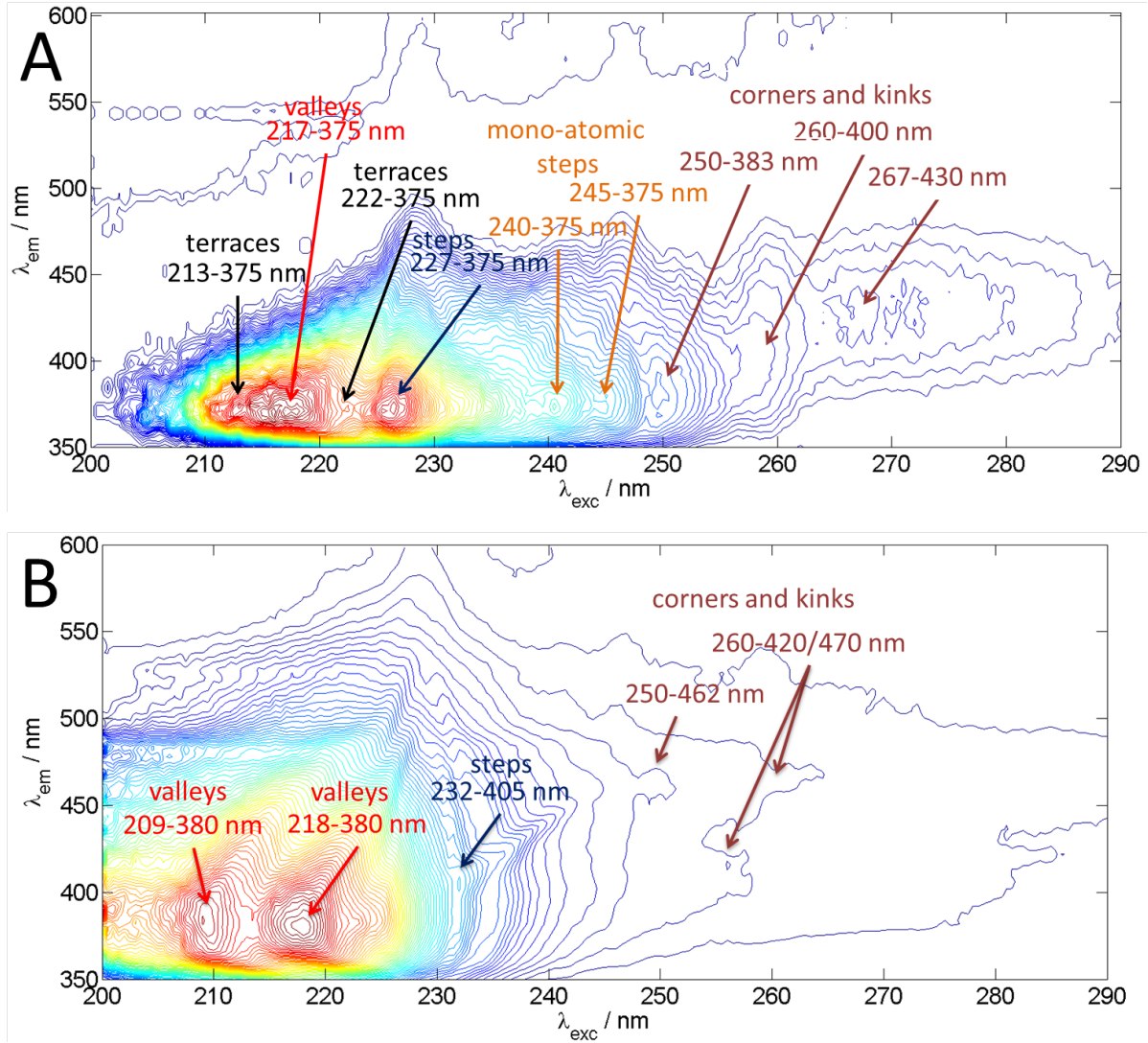


Figure 3.9: 2D photoluminescence patterns of fresh (A) and used (B) C-MgO normalized with respect to the intensity

Our experimental results are only in part compatible with the literature showing a single agreement in terms of the excitation-emission set at 240-380 nm. [45] The 2D PL patterns

of fresh C-MgO reveal that for six different excitations in the range between 213 and 245 nm, light is emitted exclusively at 375 nm irrespective of the energy of excitation. In addition, couples at 260-400, and 267-430 nm are observed (Fig. 3.9A, Table 3.1).

After extended time on stream in the OCM reaction, some features observed for the fresh catalyst disappear and some new features appear at higher emission wavelengths (Fig. 9B, Table 1). The two most intense couples for fresh MgO at 213-375 nm and 222-375 nm vanish almost entirely. The couples at 240-375 nm and 245-375 nm disappear completely. New couples at 250-462 nm and 260-465 nm appear, which have not been reported before.

The observed excitation bands are in good agreement with the IR spectroscopic results (Fig. 3.8) and theoretical calculations by Chizallet et al. (Table 1).[6] The fresh MgO surface exhibits mainly terraces that contain localized morphological defects. Six-fold and five-fold coordinated oxygen anions at terraces are excited at 213 and 222 nm, respectively, and emit light at 375 nm (Fig. 3.9B, Table 3.1). The corresponding species are extinguished by using the catalyst in the OCM reaction. Due to sintering, the catalyst surface becomes highly defective and exhibits almost no wide terraces anymore. At the same time, excitation bands assigned to valleys and edges at 209, 218, and 232 nm, respectively, become more intense (Fig. 3.9B). In accordance with IR spectroscopy (Fig. 3.8), the features at 240 and 245 nm observed only in the fresh catalyst, but not in the used one, are assigned to mono-atomic steps that disappear under OCM conditions. The weak features at 260 nm in the fresh catalyst, and at 250 nm in used C-MgO are attributed to corners and kinks, respectively, according to theoretical calculations (Table 3.1). [45] Charge transfer from the edges near the corners can occur, [37,45,83] which explains the slightly higher emission wavelength at 400 nm.

The 2D PL patterns of S-MgO and SG-MgO (Figs. S3.8 - S3.11) reflect the morphological differences between the different MgO catalysts. Features at 216-378 nm and 220-378 nm due to terrace sites are dominant in the patterns of S-MgO in accordance with the almost ideal cubic morphology of the catalyst particles. The patterns of SG-MgO are more complex and signals at 246-383 nm, and 265-407 nm that indicate the presence of mono-atomic steps and corners, respectively, appear more prominent due to the pronounced surface texturing of SG-MgO in agreement with the IR spectroscopic results (Fig. 3.3) and electron microscopy. [55]

As aforementioned, the 2D PL spectra of nanostructured MgO exhibit several different excitation peaks, which are associated with the same emission energy at approximately 375 nm. This peculiarity is tentatively attributed to charge transfer phenomena based on structural considerations. Fresh C-MgO is terminated mainly by non-polar {100} planes.

Edges, corners, kinks, and other topological forms at the $\{100\}$ surface of C-MgO can be regarded as localized structural defects. Since the neighborhood of all these defects is similar, charge transfer from different excited states into the same excited state, which is provided by the surrounding area of the defects, and from which the light is emitted, could occur. Accordingly, although different energy is required to excite the diverse structural defects (depending on their coordination number and configuration), the emitted light is of the same energy (375 nm) for most of them.

Table 3.1: Excitation-emission couples experimentally observed for fresh and used C-MGO in comparison with calculated components of excitation energy maxima. [45]

experiment (this work)				theory [45]		general assignment involving various local configurations
λ_{exc} (nm)		λ_{em} (nm)		main components of calculated excitation bands (nm)		
fresh	used	fresh	used			
	209		380	208	$O_{5C}^{2-} \rightarrow Mg_{4,5,6C}^{2+}$	valleys (V)
217	218	375	380	217	$O_{4,5,6C}^{2-} \rightarrow Mg_{4,5,6C}^{2+}$	
213		375		212	$O_{6C}^{2-} \rightarrow Mg_{6C}^{2+}$	terraces (T)
222		375		221	$O_{5C}^{2-} \rightarrow Mg_{6C}^{2+}$	
227	232	375	405	234	$O_{4C}^{2-} \rightarrow Mg_{5,6C}^{2+}$	edges and steps
				234	$O_{4,5C}^{2-} \rightarrow Mg_{4,5,6C}^{2+}$	
240		375		237-253	$O_{4C}^{2-} \rightarrow Mg_{6C}^{2+}$	monoatomic steps (S1)
245		375				
250	250	383	462	252-260	$O_{4C}^{2-} \rightarrow Mg_{3,5C}^{2+}$	Corners and kinks
260	260	402	470	455-465	$O_{3,4C}^{2-} \rightarrow Mg_{4,5,6C}^{2+}$	

After several hundreds hours under OCM reaction condition, the MgO surface becomes highly defective and exposes higher index planes, thus, the electric dipole moment of the surface changes considerably and in this case, the relaxation process of excited ion pairs changes too. An increase in the emission wavelength can be observed that goes along with the supposed increase in the polarity of the planes. The species on the surface of the used catalyst that absorbs at about 230 nm emits light at 405 nm, which corresponds to a shift of 0.25 eV referred to 375 nm for the fresh catalyst. This shift could be explained by the reconstruction of $\{100\}$ planes into $\{110\}$ planes under reaction condition of OCM. Similarly, the shift of the emission for the excitation band at 250 nm from 375 to 462 nm (=0.6 eV) can be explained by transformation of $\{100\}$ planes into $\{111\}$ planes. The differences in the termination of differently prepared magnesium oxides C-MgO, S-MgO, and SG-MgO are, accordingly, also sensitively reflected in differing excitation-emission patterns (Figs. S3.8 - S3.11).

In summary, the energy needed to excite an electronic transition in a species that belongs to a structural defect at the surface of MgO depends on the intrinsic electronic properties of this species, i.e., on the coordination number and the local topology. [45] Photolumines-

cence, i.e., the energy of the emitted light, however, seems to probe sensitively the dipolar moment of the microfacets where the corresponding defect is located. PL spectroscopy of fresh and used MgO catalysts documents, therefore, impressively the reconstruction of the MgO surface under OCM conditions.

3.3.3 ESR spectroscopy

Activation of methane or oxygen can lead to the formation of paramagnetic species like CH_3^\bullet or O_2^- radicals, which can be probed by electron spin resonance (ESR) spectroscopy.

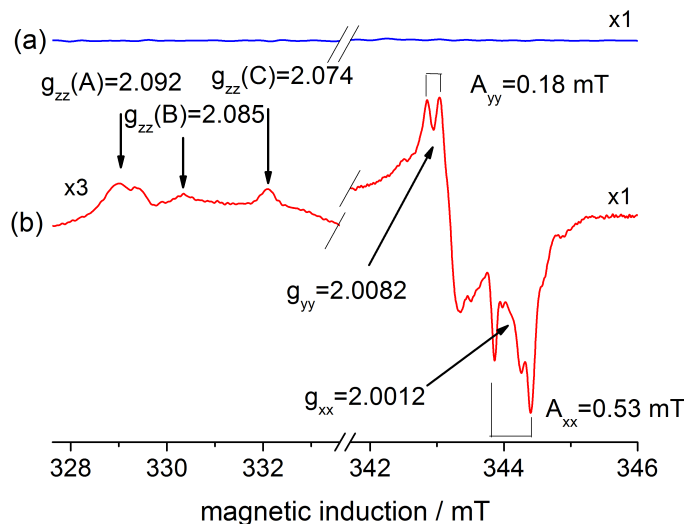


Figure 3.10: EPR spectra of C-MgO after evacuation at 1023 K in vacuum followed by (a) adsorption of and $5 \cdot 10^3$ Pa O_2 at room temperature, and subsequent evacuation, and (b) co-adsorption of $9 \cdot 10^3$ Pa CH_4 and $2 \cdot 10^3$ Pa O_2 at room temperature and subsequent evacuation. The spectra are recorded at 77 K, at a pressure of about $1 \cdot 10^{-4}$ Pa

Addition of molecular oxygen at room temperature after activation of C-MgO at 1023 K in vacuum gives no signal in the ESR spectrum (Fig. 3.10a). However, simultaneous dosing of methane and oxygen at room temperature produces a new signal in the spectrum (Fig. 3.10b). The values of the anisotropic g tensor correspond to a superoxide oxygen species. [100] The superoxide O_2^- is characterized by an orthorhombic symmetry with three principal g values g_{xx} , g_{yy} and g_{zz} with the z direction being that of the O_2^- intermolecular axis. The orthorhombic symmetry is due to the removal of the degeneracy between the two π^* oxygen orbitals. [101] In the g_{zz} region three species are observed. The g_{zz} value

is very sensitive to the electrostatic field of the surrounding. Giamello *et al.* [102] found a direct linear correlation between the Madelung potential of the adsorbing cation and the g_{zz} value of the superoxide. The high g_{zz} value at 2.092 (denoted by $g_{zz}(A)$) and the lower g_{zz} value at 2.074 ($g_{zz}(B)$) are generally assigned to superoxide formed at corners and monoatomic steps, respectively. [102] The g_{zz} signal at 2.085 was measured by Murphy *et al.*, but was not assigned to any morphological site. [103] The four well defined resonance lines in the g_{xx} and g_{yy} region are due to hyperfine coupling caused by the interaction of the superoxide ion with a proton in close vicinity and their hyperfine constants A_{xx} (0.56 mT) and A_{yy} (0.18 mT) are in agreement with the literature. [100] The formation of superoxide species may occur in an electron transfer reaction by dissociation of the polarized, and, therefore, slightly C-H acidic adsorbed methane molecule under formation of a hydroxyl group and methyl radical. [100] According to Diwald *et al.*, superoxide species formed by charge transfer between hydrogen and molecular oxygen are located either on monoatomic steps, or on oxygen vacancies situated at corners. [104]

EPR signatures of methyl radicals were not found in our spectra, probably due to a fast desorption of these products already at room temperature.

Paganini *et al.* reported about heterolytic C-H bond dissociation of saturated hydrocarbons including methane on the dehydroxylated CaO surface at room temperature, but on MgO, dissociation was not observed. [105] The formed CH_3^- carbanion is able to transfer an electron either to co-adsorbed oxygen or to the CaO surface if irradiated by UV-Vis light, thus forming superoxide O_2^- species or $F_s(H)^+$ colour centers, respectively, and a methyl radical. In our experiments, no colour centers were formed when MgO was irradiated in presence of adsorbed CH_4 . This result is in agreement with the IR spectroscopic experiments of CH_4 adsorption on MgO that reveal a significant polarization of the C-H bonds in methane, but no dissociation. Consequently, no electron transfer occurs at the surface of MgO in absence of oxygen. Instead, the adsorption of CH_4 on MgO that contains structural defects with proper configuration weakens the C-H bond, which allows the electrophilic attack by an oxygen molecule.

In summary, complementary EPR and FTIR measurements indicate that the MgO surface polarizes the C-H bond in the adsorbed methane molecule (forming $H_3C-H-O-Mg$), but that molecular oxygen is needed to finally break the bond via electron transfer from the polarized CH_4 molecule to O_2 . It is remarkable, that this process occurs already at room temperature.

3.4 Discussion

3.4.1 Structural changes of the MgO surface during the OCM reaction

The surface of MgO calcined at high temperature exhibits localized defects at the $\{100\}$ surface that contain coordinatively unsaturated sites (cus). Such structural defects comprise edges (at steps of different height) and corners. Their total concentration and relative abundance depend on the synthesis method. Differences in the synthesis technique are reflected in different initial activities and variations in the rate of catalyst deactivation [55] indicating that structural defects might be related to the catalytic activity of MgO in OCM. The strong deactivation of the catalyst under OCM conditions involves drastic changes in the primary particle morphology as observed by electron microscopy and spectroscopic techniques (Figs. 3.8, 3.9, S3.8 - S3.11). [55] There is clear evidence for the disappearance of the $\{100\}$ cubic structure and the formation of high index crystal planes, like $\{110\}$ or $\{111\}$, or microfaceted structures due to sintering of the primary MgO particles. The sintering is caused by the reaction of the unavoidable reaction product water with the catalyst surface and leads to a dynamic change in the nature of the active sites, and, consequently, in the reaction mechanism with time on stream. The results of photoluminescence spectroscopy are in agreement with surface reconstructions under reaction conditions. The red shift (by 0.6 eV) in the emission signal assigned to corners after use of C-MgO indicates that the formation of polar, *e.g.*, $\{111\}$ surfaces that exhibit an increased surface dipole moment in comparison to the $\{100\}$ surface, happens (Fig. 3.9). Water formed in the OCM reaction may stabilize polar surfaces via the formation of Mg-OH groups. [106] Since dehydroxylation of MgO is not yet complete at reaction temperature, the MgO surface in the stationary state is either totally or partially covered by hydroxyl groups. The OH groups formed under reaction conditions can also be regarded as impurity or dopant changing the Lewis acid-base properties of the catalyst surface. The presence of $\{111\}$ higher index planes on the surface of used C-MgO is also supported by IR spectroscopy. The number of corners determined by co-adsorption of CO and CH₄ increases by using the material as catalyst (compare Figs. 3.6).

In addition, the results of photoluminescence spectroscopy can furthermore interpreted in terms of the formation of microfaceted surfaces. The $\{110\}$ surface can be regarded as an infinite array of monoatomic steps in the $\langle 110 \rangle$ direction of the crystal that cause signals at 241 and 247 nm in the excitation spectra of the fresh catalyst. By using C-MgO in OCM, extinction of these signals and an increase in the signals due to polyatomic steps and valleys is observed. The formation of microfaceted surfaces is driven by thermodynamics. Based on the Born model of solids, de Leeuw *et al.* calculated that microfaceted

$\{110\}$ surfaces have a lower surface energy than the planar $\{110\}$ surface. [106]

The drastic changes of the catalyst surface with time on stream imply changes in the reaction mechanism. In the following, the catalytic properties of MgO in OCM will be discussed in the following in two parts dealing at first with the fresh MgO surface (3.4.2) and secondly with the MgO surface under stationary conditions (3.4.3).

3.4.2 Activation of methane on the dehydroxylated MgO surface

In the following, we combine the spectroscopic results reported above with kinetic data summarized in [55] to develop a model for methane activation at the surface of dehydroxylated MgO. The spectroscopic characterization of the fresh catalyst surface describes a situation, which comes across the reactants at the very beginning of the reaction. The magnesium oxides involved in the present study are comparatively rich in edges and corners present on the $\{100\}$ surface that have been quantified by FTIR spectroscopy of adsorbed CO and methane. The edges expose $\text{Mg}^{2+}\text{-O}^{2-}$ acid-base pairs, which are considered as dihapto adsorption sites for methane (Scheme 3.1), while on corners, the methane molecule is adsorbed on a single oxygen or magnesium ion. By plotting the rate of methane consumption and the rate of C_{2+} formation at $t=0$ as a function of the relative abundance of edges related to the total number of adsorption sites (edges plus corners) on the surface of the freshly pretreated catalysts, a clear correlation is observed showing the relevance of edges (Lewis acid-base pairs) for selective activation of methane on MgO with the exception of S-MgO (Fig. 3.11). In the latter catalyst that was prepared by combustion of magnesium, the abundance of steps is very low and the edges basically represent the edges of the regular cubic particles. Here the peculiar situation happens that the relative amount of edges is very high in comparison to the amount of corners, but the total amount of edges, which belong to steps, is very low due to the quite regular surface structure of the S-MgO particles. Mono-atomic steps do practically not exist on the surface of S-MgO. In a series of recent theoretical papers, Metiu *et al.* emphasized the importance of strong Lewis acid-base pairs in the activation of methane through heterolytic C-H bond dissociation and stabilization of the products on the surface of basic oxides. [107–109]

When the rate of methane consumption is plotted as a function of the abundance of mono-atomic steps, a clear trend is observed indicating that steps with a height that comprises one Mg-O distance play an important role in the activation of methane (Fig. 3.12). The underlying analysis of the corresponding FTIR spectra is shown in Figs. S3.1 - 3.6 and Tab. S4.1. Interestingly, Trionfetti *et al.* reported in agreement with our observations that the presence of step sites in MgO increases the number of active centers able to activate propane, however, in case of the propane molecule in an unselective way that leads to the

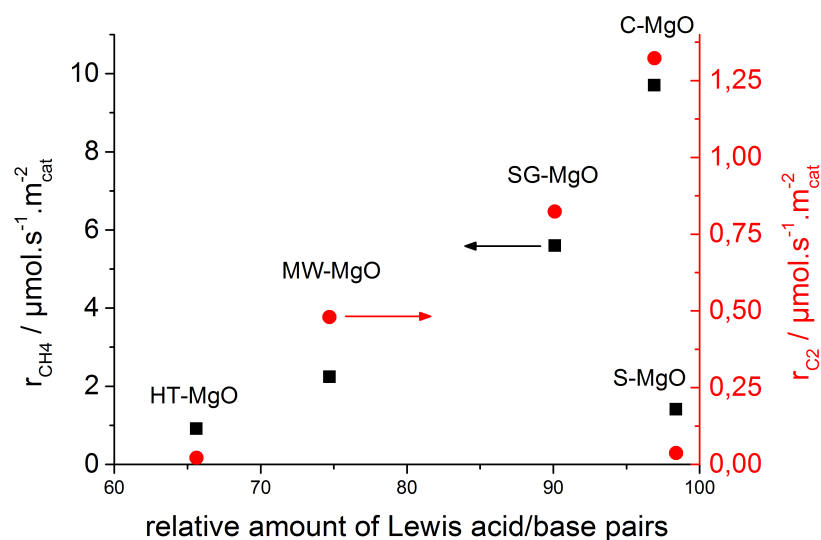


Figure 3.11: Rate of methane consumption and C_{2+} formation at $t=0$ as a function of the relative amount of acid-base pairs (edges) on the surface of the catalysts.

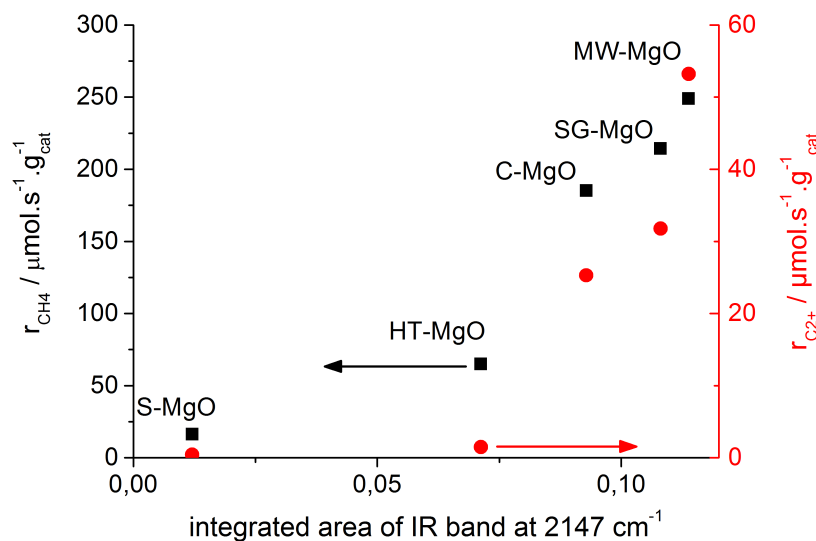


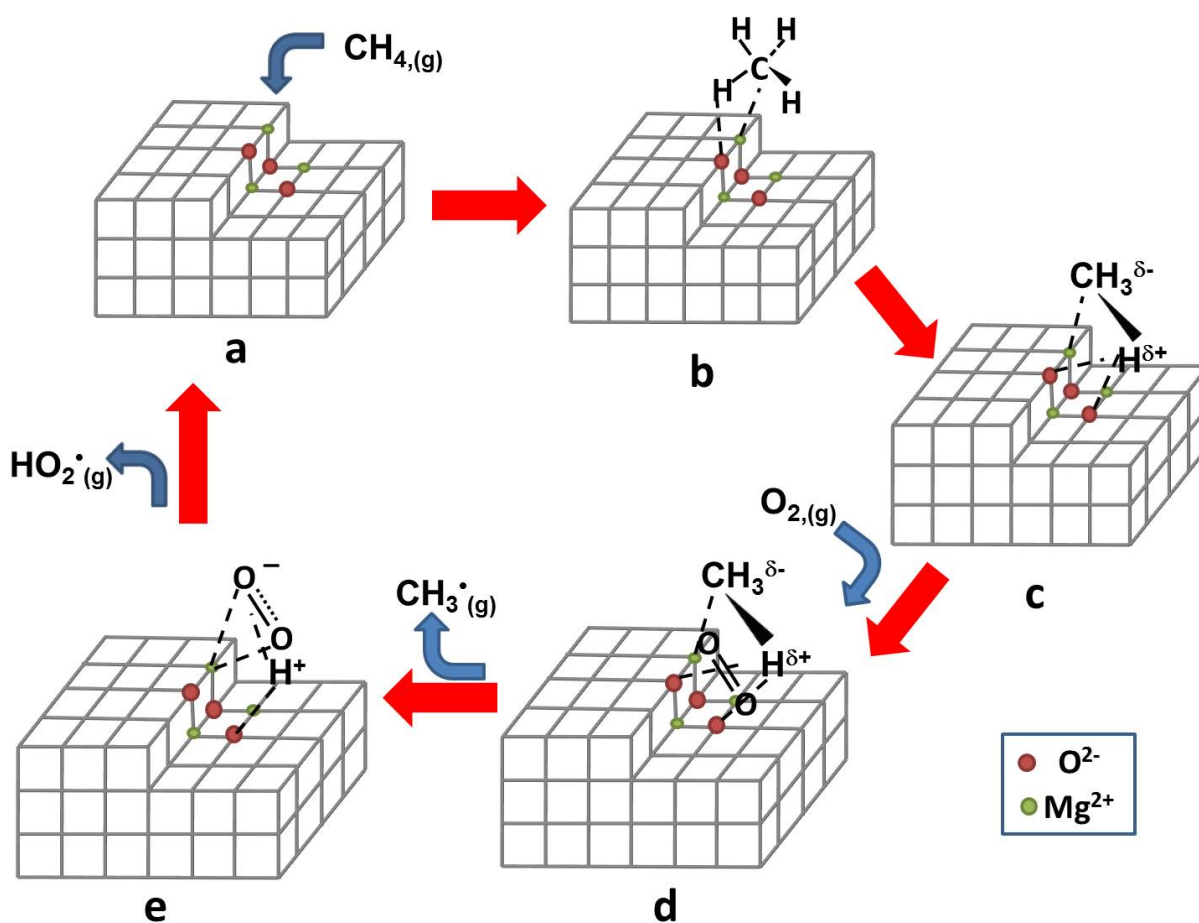
Figure 3.12: Rate of methane consumption plotted versus the integrated area of the CO adsorption peak at 2147 cm^{-1} that indicates the abundance of mono-atomic steps (steps in the dimension of a unit cell).

formation of carbon oxides. [91] In calculations that model the surface of Na-doped CaO, Sun *et al.* [109] have shown that the dissociation energy of the C-H bonds are lowered when methane adsorption takes place on monoatomic steps rather than on terrace sites or any

other defect that contains lower coordinated ions.

Taking into account the experimental findings of the present kinetic and spectroscopic studies that (i) oxygen partial pressure has a significant influence on the reaction rate, and (ii) Lewis acid/base pairs on edges of mono-atomic steps are related to methane activation, a model for methane activation on the surface of pure, nano-structured and dehydroxylated MgO is proposed that differs from the general picture of an Eley-Rideal mechanism that involves activated O^- species adsorbed on the surface (which have so far not been verified experimentally under reaction conditions) and methane reacting from the gas phase. The catalytic cycle is presented in Scheme 3.2. Thus, gas phase methane is adsorbed in a dihapto configuration on Lewis acid/base pairs located on mono-atomic steps on the surface of MgO (Steps a, and b). Co-adsorption of carbon monoxide and methane reveals that CH_4 adsorbs more strongly in dihapto than in a monohapto configuration (Fig. 3.5 and Scheme 3.2). In the second step, a C-H bond of the methane molecule is polarized as observed by IR spectroscopy of adsorbed CH_4 and CD_4 on MgO. The adsorbed methane molecule bends towards the terrace at the bottom of the mono-atomic step, which allows the interaction of H atoms of methane with basic lattice oxygen resulting in C-H bond elongation, *i.e.*, strong polarization of C-H bonds (Step c). The interaction of hydrogen atoms of adsorbed methane and oxygen atoms at the terrace is reflected in the appearance of bands due to O-H (or O-D) stretching vibrations after adsorption of (deuterated) methane at 77 K (Figs. 3.5, and 3.7). The underlying interaction is weak, since the adsorption at 77 K is reversible and no heterolytic dissociation was observed by adsorption of methane on MgO alone. This is in contrast to the properties of the stronger base CaO. At the surface of calcium oxide methane dissociates heterolytically already at room temperature. [110] The dissociation of the C-H bond on MgO is, however, possible when molecular oxygen approaches and weakly adsorbs at the MgO surface near the adsorbed methane molecule (Step d). The C-H bond is broken in a concerted mechanism forming simultaneously a methyl radical and a superoxide O_2^- species (Step e). Apparently, the oxygen molecule is able to accept an electron from the adsorbed methane molecule. The methyl radical formed is not stable at the surface of MgO and is released to the gas phase. Alternatively (or in parallel), a surface mediated coupling of two simultaneously activated methane molecules adsorbed at neighboring sites and the subsequent formation of the C_2 product ethane and hydrogen peroxide may happen without desorption of methyl radicals. [55] The latter option may prevail at the high reaction temperature, whereas the occurrence of O_2^- species after contact of C-MgO with a reaction mixture of methane and oxygen at room temperature has been confirmed by ESR spectroscopy (Fig. 3.10). Hyperfine coupling of the superoxide anion with a proton in close proximity suggests heterolytic C-H bond dissociation on monoatomic steps of MgO at least at room temperature. The active site is regenerated by desorption of the perhydroxyl radical HO_2^\bullet , which may initiate further homogeneous reactions by,

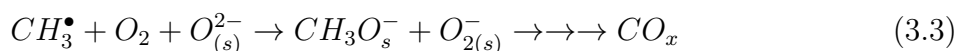
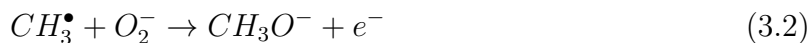
e.g., hydrogen abstraction from methane molecules in the gas phase. [111] The increasing CO_2/CO ratio observed with increasing methane conversion [55] could be attributed to the formation of HO_2^\bullet radicals in the gas phase according to reaction 3.1. Reaction 3.1 would also explain the strong decrease in the CO_2/CO ratio with time on stream that goes along with the fast disappearance of monoatomic steps, on which the mechanism proposed in Scheme 3.2 is predominant.



Scheme 3.2: Proposed mechanism of methane activation on dehydroxylated MgO

The mechanistic concept proposed in Scheme 3.2 provides an explanation for the high reaction temperatures that are required, which is, apparently, in conflict with the observation that methane can be activated already at room temperature on the surface of MgO (Figs. 3.5, 3.7, and 3.10). Perhydroxyl radicals are precursors for the formation of hydroxyl groups and water, which may lead to deactivation of MgO by sintering. Once the surface is

covered with adsorbed hydroxyl groups, methane cannot adsorb anymore, unless high reaction temperatures are applied to assure a partially dehydroxylated surface under reaction conditions. In addition, Ito *et al.* reported that methyl radicals from the gas phase could react with surface oxygen under formation of strongly bonded methoxide species according to eq. 3.2. Lunsford *et al.* confirmed that the sticking coefficient of methyl radicals on metal oxide surfaces drastically increase in the presence of oxygen in the gas phase due to the formation of methoxide ions according to eq. 3.3. [80] Methoxide species can be transformed into carbonates at room temperature and decompose only at high temperature ($T > 700$ K) to produce either syngas or carbon dioxide and water. Equation 3.3 is the route to total oxidation during the OCM reaction.



3.4.3 Active sites under stationary conditions

Mono-atomic steps disappear in the used catalysts (Figs. 3.8, and 3.9). The decrease in specific surface area, the increase in MgO domain size, as well as the degradation of the cubic {100} structure evidence sintering processes of the primary MgO particles during time on stream under conditions of the OCM reaction. [55]

Water vapor at reaction temperature induced the stabilization of high index plane surface terminations (Fig. 3.9). Theoretical calculations show that MgO experiences surface reconstruction at high water coverage forming thermodynamically stable hydroxylated {111} surfaces. [106, 112] Water is preferentially adsorbed on mono-atomic steps or {310} like planes. [106, 113] In this respect, water vapor acts as a catalyst poison destroying the highly active monoatomic steps identified on the surface of the freshly pretreated MgO catalysts. Under reaction conditions of the oxidative coupling of methane, pure MgO is transformed into a dynamic phase mixture of MgO and Mg(OH)₂. By electron microscopy, the formation of more rounded particles, which are terminated by higher index planes, is observed for all MgO catalysts. [55] The closely related particle morphology of the used catalysts is in agreement with similar methane conversions in the stationary state over the differently prepared magnesium oxides. Consequently, the nature of the active sites and, accordingly, the reaction mechanism changes with time on stream.

The interaction of water vapor with MgO is the driving force for the formation of point defects either on the surface or in the bulk of the oxide. Point defects, involving hydroxyl groups adjacent to a magnesium vacancy (V_{OH} -like centers or $(V''_{Mg}OH^\bullet)'$ -equivalent cen-

ters) are presumably important for the catalytic activity of MgO in the stationary state, since they are the precursors for the formation of O^- sites (positive holes bound to an oxygen lattice O_2^- ion ($O^{2-} + h^\bullet = O^-$)), which, perhaps, are present as triangular O^- arrays of the $\{111\}$ planes. [26] The O^- centers have been taken into account as sites for the activation of small alkane molecules or hydrogen. [4, 69] In the same way, the incorporation of excess oxygen into MgO leads to the formation of cation vacancies and O^- anions ($Mg^{2+}O^{2-} + \delta O_2 = Mg^{2+}O_{1-\delta}^{2-}(O^-)_{2\delta}$). [25] The formation of Mg vacancies and positive holes were experimentally confirmed by conductivity measurements of MgO in the presence of oxygen at high temperature. [114, 115] However the addition of carbon dioxide to the OCM feed does not affect the reactivity at steady state. CO_2 is known to react strongly with O^- species to form carbonate species. In the case of Li doped MgO, CO_2 is considered as a poison for the catalyst. [7, 116] Again, the high reaction temperatures may be responsible for maintenance of activity due to the decomposition of carbonates.

Hence, the situation at steady state is much more complicated than on fresh MgO catalysts. The cubic $\{100\}$ structure and monoatomic steps have vanished and the surface of the catalyst exhibits higher index planes or microfacets. At the same time, different species are adsorbed on the catalysts surface changing its reactivity and electronic properties. For instance, adsorbed protons on lattice oxygen change the basicity of the MgO surface as emphasized by Metiu *et al.* [107, 108] Activated oxygen (like superoxide) adsorbed on the surface may also be reactive in the OCM reaction. At the same time, the change in the MgO morphology due to water vapor induces the formation of point defects that can also change the reactivity.

It appears that at steady state the OCM reaction over MgO is less structure sensitive than on fresh MgO catalysts, explaining the relative similar activity of the five differently prepared pure MgO catalysts despite difference in the surface structure (Figs. 3.9B, S3.9, S3.11). [55] The surfaces of the higher index planes offer strong adsorption sites for methane allowing perhaps different mechanisms of C-H bond polarization. Based on the current experimental results, however, only speculations are possible. A deeper understanding of the situation under stationary conditions requires further investigations.

3.5 Conclusion

Oxidative coupling of methane on the surface of magnesium oxide is a dynamic and structure sensitive process. With time on stream the nature of active sites changes and different reaction pathways that differ in the mode of activating methane and oxygen may happen

in parallel.

On the freshly activated, nano-structured and dehydroxylated magnesium oxide surface, methane coupling happens through intermolecular charge transfer between methane adsorbed on acid-base pairs located at edges of mono-atomic steps and weakly adsorbed oxygen approaching from the gas phase. Mono-atomic steps offer an optimal configuration for the adsorption of methane and the polarization of its C-H bonds. The mechanism is in accordance with the semi-quantitative correlation between active site concentration determined by FTIR spectroscopy and reaction rate, and supported by the detection of O_2^- species by ESR spectroscopy, as well as the strong relation between methane consumption rate and oxygen partial pressure observed in the kinetic study. [55] The outcome of the present study implies a design concept of highly active sites for methane activation. However, the corresponding sites are not stable, since the mechanism is self-inhibited by formation of the by-product water and the destruction of the active sites, which are preferentially attacked by water vapor at the high reaction temperatures.

The MgO particles sinter due to the presence of water and the high temperature. The sintering process occurs through the formation of magnesium vacancies. Once the surface energy of the MgO is minimized under OCM reaction condition in the stationary state, the formation of magnesium vacancies due to water incorporation is supposed to be marginal since the OCM feed becomes increasingly oxidizing. The high concentration of oxygen may lead to the formation of V^- centers due to the excess of oxygen incorporation and formation of $\{111\}$ microfacets. Systematic studies of the deactivation and sintering process are, however, required to deliver more detailed insight into the activation of methane and oxygen and the nature of the active sites under stationary conditions.

Since water is an unavoidable reaction product, the stabilization of mono-atomic steps is not trivial. Therefore, alternative strategies should also be considered in the design of stable catalysts for OCM. Recently, the formation of strongly bound O_2^- species, the precursors of dissociatively adsorbed O_2 , has been observed on single-crystal CaO films doped with Mo^{2+} ions. [54] Such an electronic doping does not require any surface structural defects. The concept, which is also applicable to powder catalysts, [54, 117] provides another promising approach to active and stable OCM catalysts.

3.6 Supporting information

3.6.1 UV-vis spectroscopy

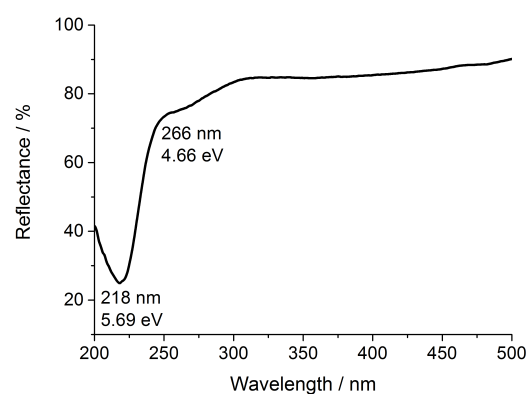


Figure S 3.1: UV-vis spectra of C-MgO catalyst measured in vacuum at 293 K after pretreatment in vacuum at 923 K.

3.6.2 Photoluminescence spectroscopy

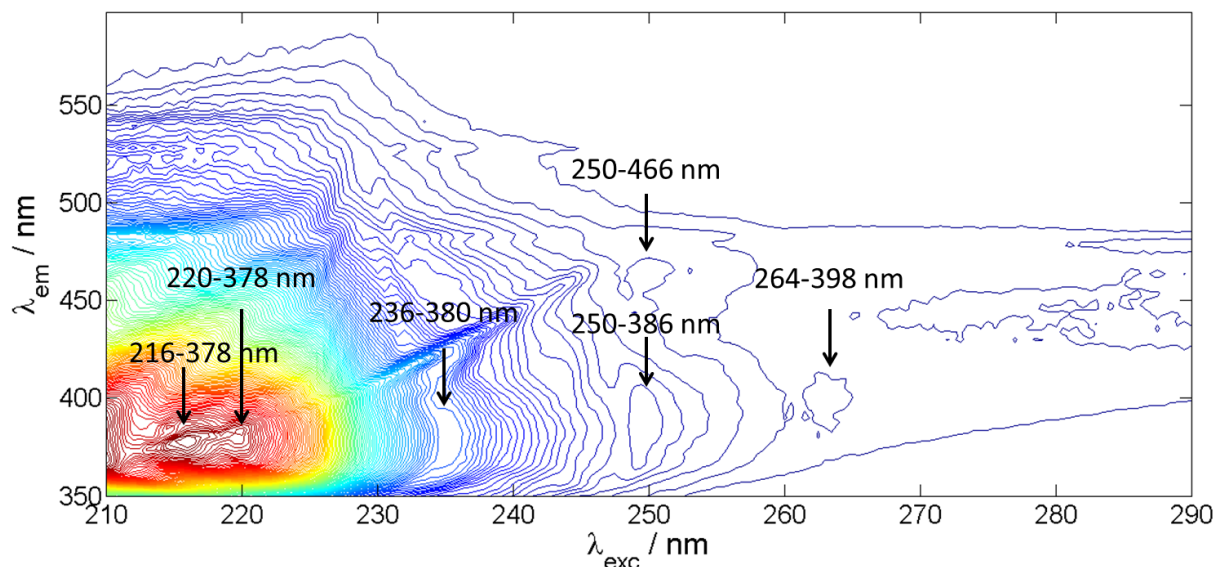


Figure S 3.2: 2D photoluminescence of fresh S-MgO (#12817) recorded at 300 K in dynamic vacuum after activation at 1073 K in vacuum.

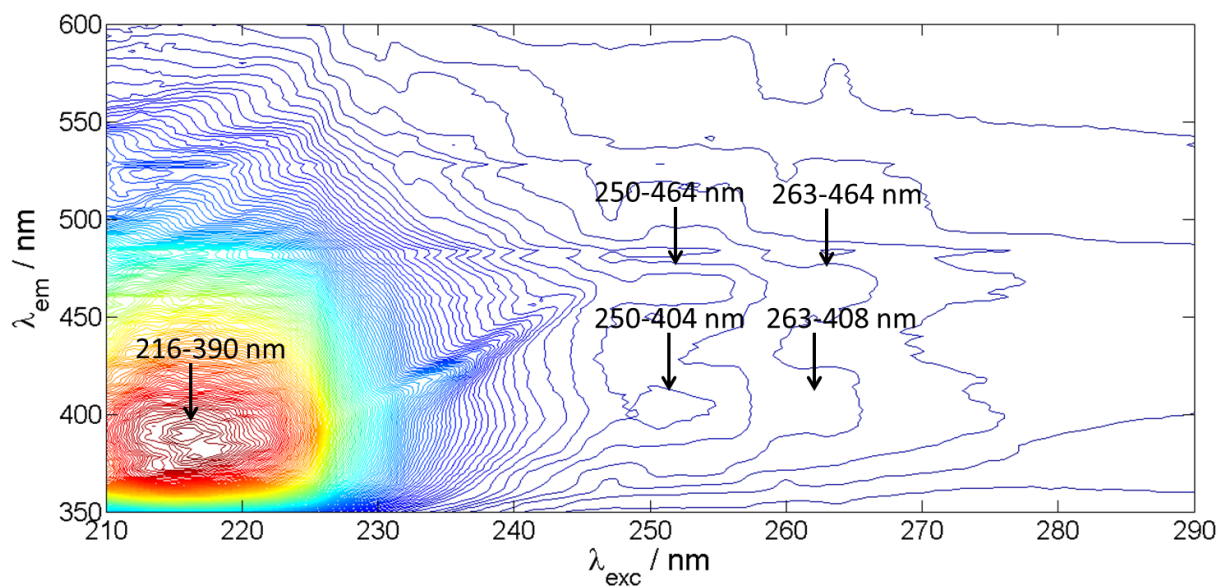


Figure S 3.3: 2D photoluminescence of used S-MgO (#12992) recorded at 300 K in dynamic vacuum after activation at 1073 K in vacuum.

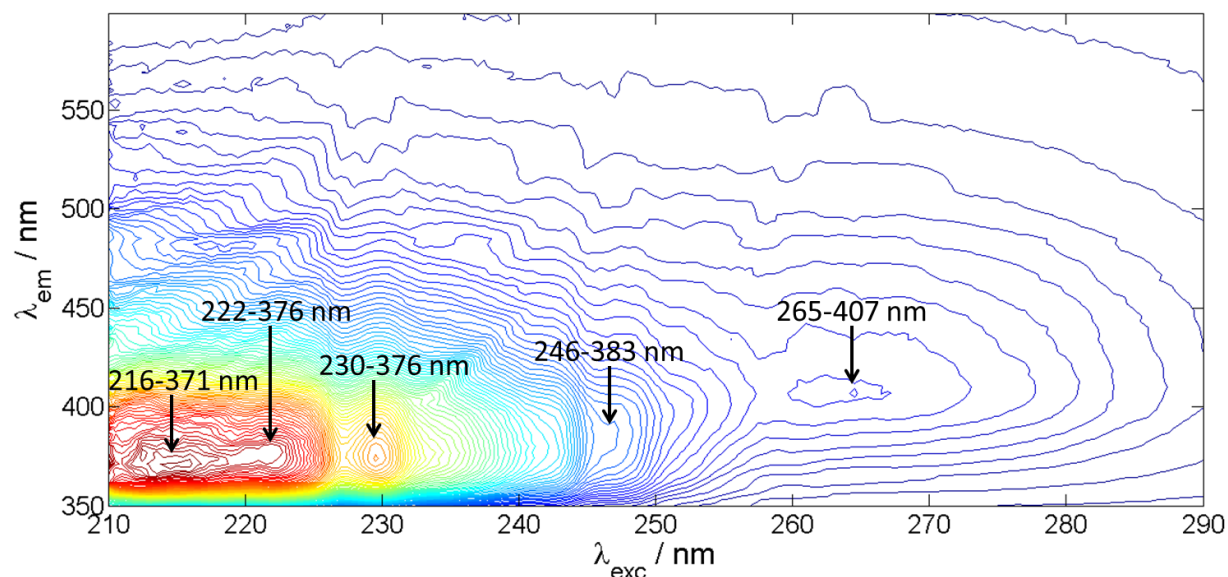


Figure S 3.4: 2D photoluminescence of fresh SG-MgO (#12342) recorded at 300 K in dynamic vacuum after activation at 1073 K in vacuum.

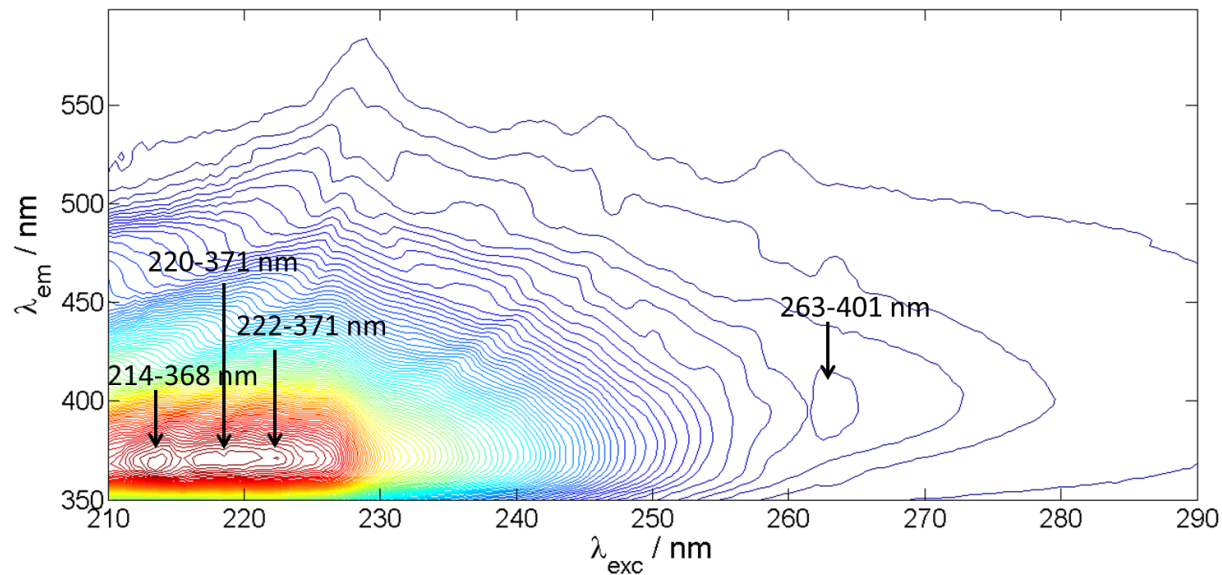


Figure S 3.5: 2D photoluminescence of fresh HT-MgO (#12498) recorded at 300 K in dynamic vacuum after activation at 1073 K in vacuum.

3.6.3 IR spectra deconvolution

For a semi-quantitative analysis of the IR spectroscopy of adsorbed CO on MgO surface, the spectra were fitted by gaussian shaped curve. For this purpose the wavenumber of five bands at 2188, 2165, 2155, 2147, 2134 cm^{-1} described in the literature were kept fixed. The assignment of these bands is reported extensively in the main text of this article. A coverage of 15 % were used for the IR spectra deconvolution.

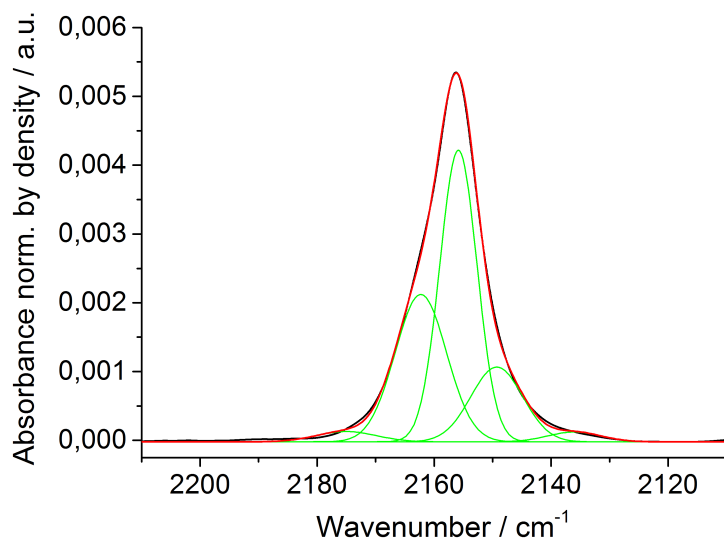


Figure S 3.6: Spectrum of CO adsorbed on S-MgO at T=77 K and a coverage of $\theta=0.15$. Black curve: experimental data, red curve: fitting, green curves: individual Gaussian component.

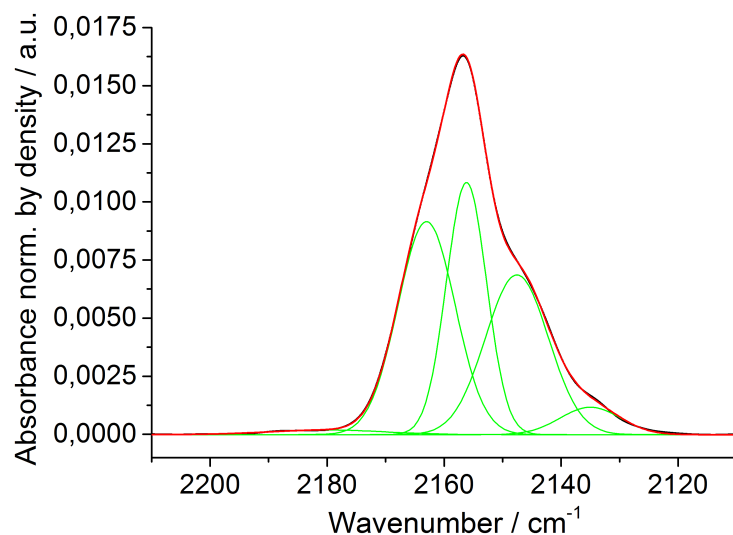


Figure S 3.7: Spectrum of CO adsorbed on C-MgO at T=77 K and a coverage of $\theta=0.15$. Black curve: experimental data, red curve: fitting, green curves: individual Gaussian component.

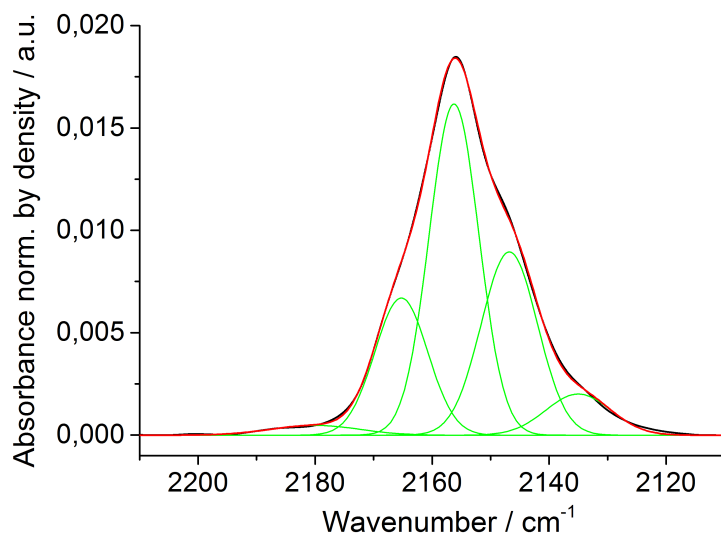


Figure S 3.8: Spectrum of CO adsorbed on SG-MgO at T=77 K and a coverage of $\theta=0.15$. Black curve: experimental data, red curve: fitting, green curves: individual Gaussian component.

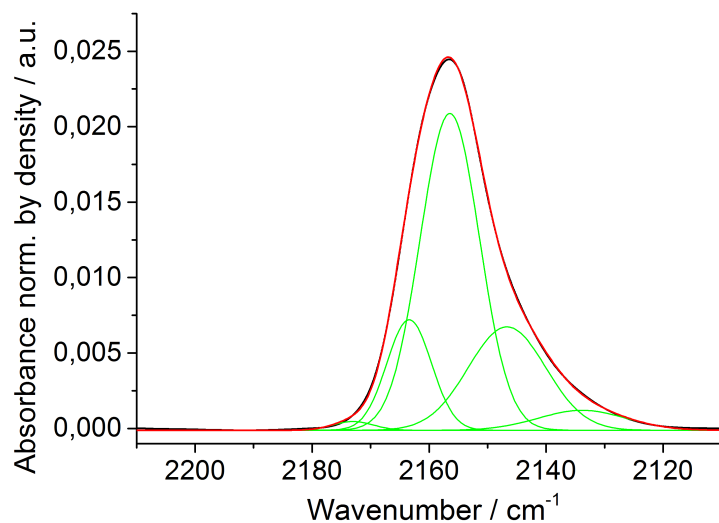


Figure S 3.9: Spectrum of CO adsorbed on MW-MgO at T=77 K and a coverage of $\theta=0.15$. Black curve: experimental data, red curve: fitting, green curves: individual Gaussian component.

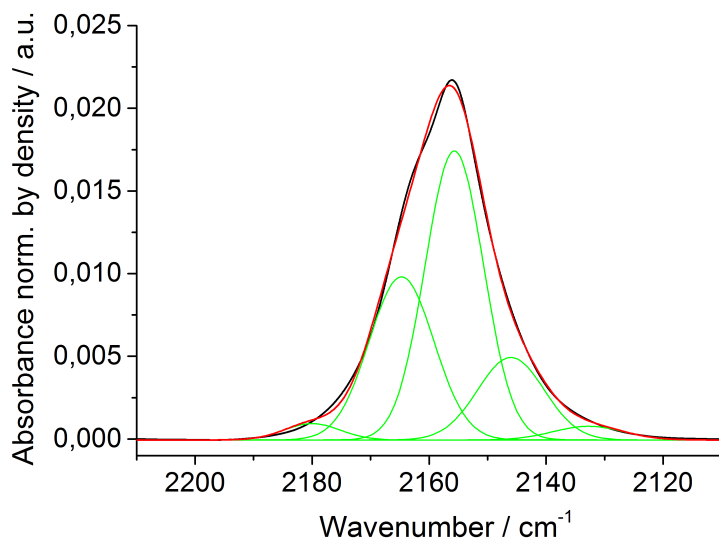


Figure S 3.10: Spectrum of CO adsorbed on HT-MgO at T=77 K and a coverage of $\theta=0.15$. Black curve: experimental data, red curve: fitting, green curves: individual Gaussian component.

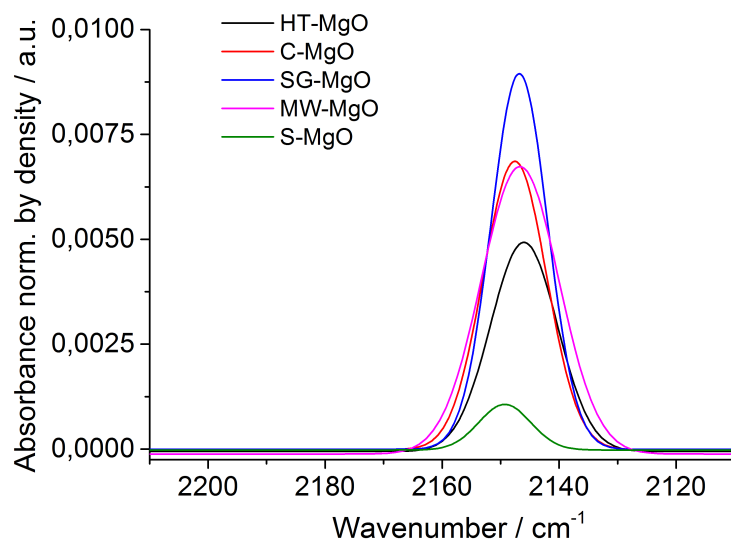


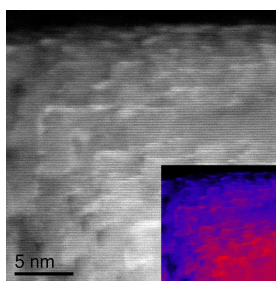
Figure S 3.11: Comparison of the fitted Gaussian component for the contribution of the 2147 cm^{-1} band for the five MgO catalysts.

Table S 3.1: Integration of the Gaussian components in arbitrary unit.

	2147 cm^{-1}	2155 cm^{-1}	2165 cm^{-1}
S-MgO	0.01207	0.03393	0.02362
C-MgO	0.09284	0.09345	0.11258
SG-MgO	0.10808	0.17251	0.07613
MW-MgO	0.11382	0.26707	0.07008
HT-MgO	0.07122	0.21813	0.13682

4. Methane coupling over magnesium oxide: how doping can work ³

Pierre Schwach, Marc-Georg Willinger, Annette Trunschke, Robert Schlögl



Abstract: Electronic doping of magnesium oxide catalysts has an effect on the oxidative coupling of methane. Highly active sites can be created by co-modification of MgO with iron and gold in ppm quantities.

Keywords: alkaline earth oxides; defects; doping; heterogeneous catalysis; oxidative coupling

Acknowledgment: We thank M. Hashagen, F. Rybicki, Dr. F. Girgsdies, Dr. M. Eichelbaum, and Dr. O. Timpe for experimental support and scientific discussions. This work was conducted in the framework of the COE UniCat (www.unicat.tu-berlin.de) of the German Science Foundation.

4.1 Introduction

Functionalization of methane remains a challenging target from academic as well as industrial points of view. [118,119] New concepts in catalytic activation of C-H bonds are needed [118] to overcome the current limitations in selectivity, which hamper the broad

³The following chapter is adapted with permission from [117] [Methane coupling over magnesium oxide: how doping can work; P. Schwach, M. G. Willinger, A. Trunschke, R. Schlögl; *Angewandte Chemie International Edition*; 52 (43); 11381-11384. Copyright ©2013 WILEY-VCH Verlag GmbH & Co. KGaA, Weinheim. <http://onlinelibrary.wiley.com/doi/10.1002/anie.201305470/abstract>]

application of methane coupling in the production of olefins as important platform chemicals from sustainable resources like natural gas or organic waste. Among the various inorganic materials that have been evaluated as heterogeneous catalysts for oxidative coupling of methane (OCM), alkaline earth oxides doped with alkali elements or transition metal ions received particular attention. [8] High reaction temperatures (973-1273 K) are needed. However, the temperature is not required for C-H activation that may be aided by coordinatively unsaturated sites already at low temperature, [58] but rather for recovery of an active catalyst surface free of hydroxides and carbonates. Under the harsh reaction conditions, oxide catalysts, like Li-MgO, undergo fast deactivation due to sintering promoted by water as an unavoidable reaction product. [32,34] Oxygen or magnesium vacancies ($V_{\text{O}}^{\bullet\bullet}$, $V_{\text{Mg}}^{\bullet\bullet}$) are involved in the sintering of MgO by facilitating reconstructions due to enhanced diffusion of lattice ions, which is fast in any case at such high temperatures. [120] On the other hand, vacancies may have an impact on activity and selectivity in catalysis. However, point defects were so far never detected under realistic OCM working conditions over MgO.

In a recent study, Freund et al. provide evidence that strongly bound O_2^- species as precursor of dissociatively adsorbed O_2 are formed on highly ordered CaO films doped with Mo^{2+} . The results indicate that molecular activation on doped oxides does not require any surface structural defects. [54] Accordingly, it is suggested that activation of methane on smooth surfaces of transition-metal-doped wide-gap oxides may involve such activated oxygen species.

In the present work, we put the concept to test and synthesized powder catalysts, working at $T=1023$ K. We used doped magnesium oxide as it was frequently investigated in OCM. [70] Pure magnesium oxide deactivates at this temperature quite fast and reaches a stationary state after a few minutes to several hours depending on the applied contact time and the initial nano-structure of the magnesium oxide. In the stationary state, a low, but constant yield of the coupling products ethane and ethene is obtained over smooth, rounded MgO particles. [57]

In this contribution, we introduced Fe in ppm quantity into MgO. The synthesis of Fe-doped polycrystalline magnesium oxide in which the Fe dopant is homogeneously distributed over the entire bulk is, however, quite challenging and requires highly sensitive analytical techniques for verification. The issue is dissolving the dopant in such a way into the bulk of the MgO that no precipitates or segregated nanostructured dopant phases occur during the drastic reaction conditions. Only then the validity of the electronic doping concept put forward by Freund et al. can be tested without interference for other catalytic actions of secondary phases.

The presence of Fe atoms on the surface may introduce additional redox chemistry into

the activation mechanism of methane, but, even in an ideal solid solution, terminating Fe atoms cannot be avoided. Therefore, the Fe-MgO catalyst was modified by subsequent adsorption of highly dispersed gold on the surface. An Au-MgO catalyst [121] was included in the study for reference.

4.2 Results and discussion

The catalysts were synthesized by hydrothermal treatment of MgO in presence of aqueous solutions of FeSO_4 , HAuCl_4 , or a mixture of the two solutions, respectively, in a microwave autoclave at 483 K and 10 bar for 3 hours, followed by annealing in flowing Ar at 1173 K for 3 hours. In order to remove potentially segregated transition metal and metal oxide particles, the obtained solids were subjected to a treatment with aqua regia or nitric acid, respectively, and annealed again in Ar at 1123 K for three hours. X-ray diffraction reveals that the lattice constants of the three doped catalysts do not vary significantly, but the size of the coherently scattering domains (reported from full patterns XRD analysis as volume weighted mean column length based on integral breadth (LVol-IB)) differs, showing the largest crystalline domains for Au-Fe-MgO, which is also reflected in the lowest specific surface area (Tab. 4.1). Structural investigation by TEM reveals typical small aggregates consisting of cubic shaped particles that are intergrown and connected mainly along shared faces (Fig. 4.1). The domain size determined by XRD is similar for Fe-MgO and Au-MgO (Tab. 4.1) and ranges between 5 and 100 nm according to TEM (Fig. 4.1). The slightly lower specific surface area of Au-MgO indicates a smoother surface of the gold-covered MgO compared to Fe-MgO.

Table 4.1: General characteristics of the doped MgO catalysts and normalized formation rates of coupling products ethane and ethene in OCM of methane.

Catalyst	Fe-MgO	Au-Fe-MgO	Au-MgO
ID ^[a]	14696	14593	14588
$c_{\text{Fe}}^{[b]}$ [ppm]	654	402	-
$a^{[c]}$ [Å]	4.214(1)	4.213(1)	4.214(1)
$L_{\text{Vol-IB}}^{[c]}$ [nm]	46(1)	67(1)	47(1)
$A^{[d]}$ [$\text{m}^2 \cdot \text{g}^{-1}$]	32.0	19.9	25.6
$r_{\text{C}_{2+}}^{[e]}$ [$\mu\text{mol} \cdot \text{s}^{-1} \cdot \text{g}_{\text{cat}}^{-1}$]	5.12	13.55	0.68
$r_{\text{C}_{2+}}^{[e]}$ [$\mu\text{mol} \cdot \text{s}^{-1} \cdot \text{m}^{-2}$]	0.16	0.68	0.03
Redox active Fe ^[f]	6%	7%	-

^a Catalyst ID for clear identification of the batch.

^b Measured by AAS.

^c Determined by XRD.

^d Specific surface area calculated applying the BET equation.

^e Measured after 4 hours time on stream; Reaction conditions: $T=1023 \text{ K}$, $W/F=0.033 \text{ g} \cdot \text{s} \cdot \text{ml}^{-1}$, $\text{CH}_4/\text{O}_2/\text{N}_2=3/1/1$.

^f Percentage of Fe that is accessible at the surface as estimated by temperature-programmed reduction (see Tab.4.1)

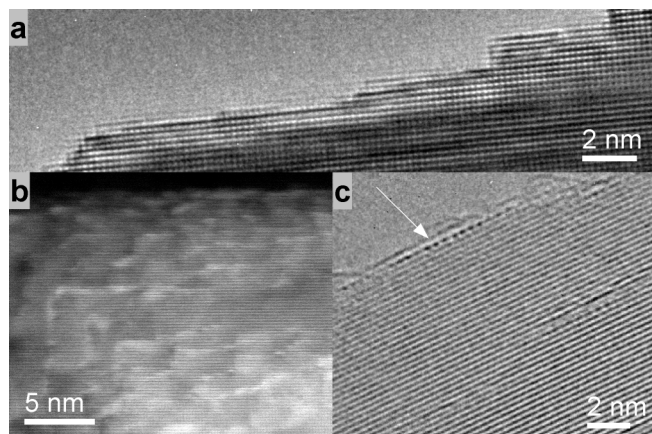


Figure 4.1: a) HRTEM image showing the stepped surface of Au-Fe-MgO. b) HAADF STEM image with characteristic bright contrast at steps and edges due to decoration with heavy atoms. c) Columns of heavy atoms can also be seen in thin regions in HRTEM.

The UV-vis spectra of Fe-MgO and Au-Fe-MgO are dominated by an intense absorption in the range of ligand to metal charge transfer (LMCT) bands (Fig. 4.1). The absorption maximum near 288 nm (34723 cm^{-1}) is attributed to isolated Fe^{3+} ions in octahedral coordination, i.e., on Mg^{2+} lattice positions. [122] EPR spectroscopy confirms the occurrence of Fe^{3+} in cubic symmetry sites in MgO (Fig. 4.2). Contributions of oligomeric species and iron oxide nano-particles to the UV-vis spectra cannot be excluded due to the complex fine structure and the extended tail of the bands towards decreasing energy. However, no aggregates of iron have been detected by TEM, indicating high Fe dispersion. Since the Fe concentration is low, the weak absorption due to d-d transitions in the range between 330 nm (30000 cm^{-1}) and 1000 nm (10000 cm^{-1}) gives featureless, very weak and broad bands that do not allow an unambiguous interpretation with respect to the coordination environment of Fe^{3+} (d5) ions, and potentially appearing Fe^{2+} (d6) ions. The spectra of the gold-containing catalysts exhibit the characteristic surface Plasmon mode around 520 nm (19230 cm^{-1}) that is ascribed to gold nano-particles. [123] The broad appearance of the band suggests that Au occurs in different particle sizes ranging from atomic dimensions to Au particles with a diameter of about 10 nm. [124] Indeed, very rare and scarcely distributed isotropic gold nanoparticles can be found on the surface of the MgO particles by TEM.

Temperature-programmed reduction (TPR) oxidation (TPO) cycles have been performed to analyze the redox properties of the Fe-containing MgO catalysts (Figs. 4.3-4.4). In the first run, the catalysts were heated in inert gas and evolution of hydrogen was observed in a temperature range between 573 and 673 K and under isothermal conditions at 1073 K indicating the formation of point defects in the bulk of Fe-MgO and Au-Fe-MgO during the

thermal pretreatment. [125] The hydrogen-consumption profile of the first TPR run differs from the second and third run that have been performed in each case after intermediate temperature-programmed oxidation. In contrast, the second and third TPR profiles are identical revealing high reversibility, stability and absence of segregation processes after initial stabilization during the first cycle. This applies to Fe-MgO (Fig. 4.3) as well as to Au-Fe-MgO (Fig. 4.4) indicating that the catalysts are well comparable, in particular, because the bulk oxide properties, which have been sensed by redox probing, are quite similar in agreement with the XRD results. The first TPR run reveals a dopant-induced difference between the two catalysts. In addition to the two high-temperature peaks around 810-840 K and 1050-1060 K, Fe-MgO exhibits an additional hydrogen consumption peak at low temperature (513 K) arising from easily reducible Fe species. The peak does not appear again in following cycles indicating the dissolution of the species into the bulk where it is protected from re-oxidation. The amount of consumed hydrogen proves that only a minor fraction of the low-level iron doping is susceptible to reduction on the surface (Tab. 4.1) and Tab. 4.1) indicating the homogeneous distribution of the dopant within the bulk of magnesium oxide. The fraction of reducible iron is initially higher in Fe-MgO compared to Au-Fe-MgO, indicating that surface iron species are shielded by topping gold species.

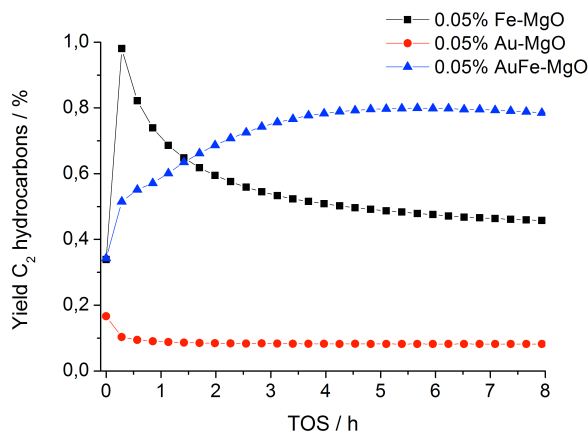


Figure 4.2: Yield of ethane and ethene in the oxidative coupling of methane as a function of time on stream (TOS) at $T=1023$ K; $W/F= 0.0167 \text{ g} \cdot \text{s} \cdot \text{ml}^{-1}$, $\text{CH}_4/\text{O}_2/\text{N}_2=3/1/1$.

The low yield of coupling products in OCM as presented in Fig. 4.2 was deliberately measured at short contact times to prevent full oxygen conversion and thus to allow a meaningful kinetic comparison. Gold seems to block the active sites on the surface of MgO since Au-MgO shows only negligible activity. This is ascribed to the propensity of gold to adsorb at step edges of the MgO and thus covering the active sites related to edges. [126] Fe-MgO is more active (Figs. 4.5-4.6) and selective (Fig. 4.7) resulting in higher yield.

The start-up behaviour of Fe-MgO is attributed to the presence of surface redox-active iron species in accordance with the observations made by TPR. Further increase in methane conversion and selectivity is achieved by co-doping with Fe and Au. Such a synergistic effect of the two transition metal additives becomes even more obvious by comparing the rate of C₂ formation normalized to the specific surface area of the catalyst (Tab. 4.1). After a formation period with increasing activity, Au-Fe-MgO shows stable activity at the time scale of the present experiment. This behaviour is surprising and novel for alkaline earth metal oxide-based catalysts.

An explanation may be provided by electron microscopy. HAADF STEM, which is sensitive to variations in atomic weight, allows locating the heavier dopant atoms in the MgO matrix. As can be seen in Figures 4.1, corners and edges are characterized by brighter contrast, indicating the presence of either Au or Fe. This is confirmed by HRTEM images recorded from thin regions of MgO crystals, where rows of strongly scattering atoms are detected at surface steps even after catalytic testing (Fig. 4.1c and Fig. 4.8). These atoms will suppress the action of steps as active sites and thus poison the Au-MgO catalyst that does not have sites caused by electronic doping. In addition, investigation of the bulk structure by HAADF STEM and TEM reveals the presence of local strain, causing particular contrast variations such as indicated in Figures 4.3a and b, respectively. Analysis of the lattice fringes [127] shows doping induced strain and lattice rotation, as visualized in Figures 4.3c and d, respectively. Due to the low concentration, EDX elemental analysis is not sensitive enough to clarify whether the defects are caused by gold or iron incorporation into the MgO lattice.

The sintering behaviour of Au-Fe-Mg O is similar compared to un-doped MgO. Initially, the surface of the cube-shaped particles exposed stepped and atomically flat planes (Fig. 4.1). Steps are usually in the range of half (one atom) and single unit cell height (Fig. 4.1a). During catalytic reaction, the abundance of such small steps decreases forming larger steps. Despite these sintering phenomena, the catalytic activity of the Au-Fe-MgO catalyst shows appreciable stability. This is a clear indication that the lasting activity is not due to the conversion of methane at steps but rather at sites located at terraces. Doping has changed the nature of the active sites as indicated clearly by the temporal evolution of the catalytic activity shown in Figures 4.2 and 4.5-4.7. The inverse trend for the co-doped system as compared to the other systems points to the formation of active sites for oxygen activation in Au-Fe-MgO during time on stream whereas the other systems deactivate through the loss of monatomic step sites following surface transformation caused by the reaction products water and CO₂. The stable minimal activity of the Au-MgO system marks the intrinsic activity of active sites in the present MgO that are not associated with step edges. Compared to this activity (see Table 4.1) the electronic doping by Fe increases

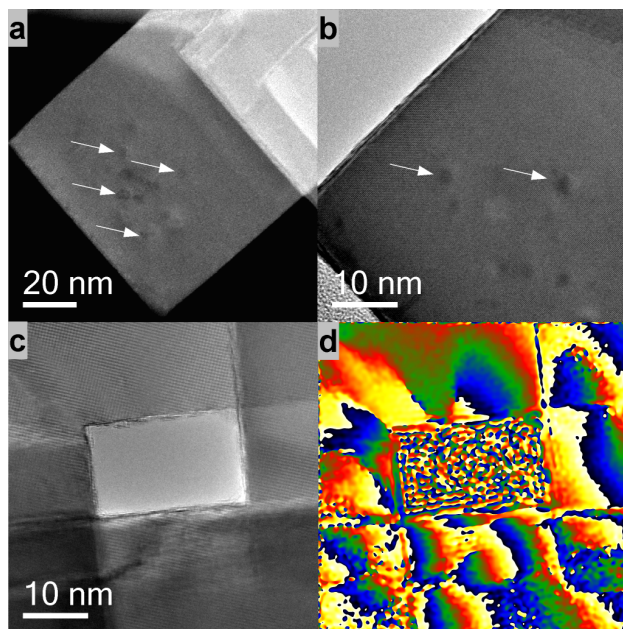


Figure 4.3: a) HAADF STEM and b) TEM image with localized contrast variations due to defects caused by bulk doping as indicated by arrows. c) HRTEM image of doped MgO particles for which the lattice rotation due to strain is shown in d).

the rate of C_2 formation by over an order of magnitude.

For the classical Au-MgO system it was found that small doping levels produce metallic and some chemically active gold species decorating steps and thus reducing the activity of parent MgO exactly as found in the present study. [121] Only at much higher doping levels catalytic effects were described and associated with Au particles and defect formation in MgO. In the present study two types of gold were evidenced based on the catalytic results: In single doped Au-MgO only the step-decorating poisoning effect was found. Through the presence of sub-surface iron species in the co-doped system the edge decorating effect was massively overruled by a beneficial effect of creating structurally stable novel active sites at terraces of the MgO without introducing vacancies that may destabilize the system at longer time on stream. This second gold species apparently arises from a significant gold-support interaction achieved by the strain in the MgO due to iron doping. The possible effects of isotropic unstrained gold particles are negligible in the present study due to their very low abundance as a consequence of the synthesis strategy. Electronic doping of MgO terraces is also achieved through iron dissolution only, but with significant lower effectiveness. It is tempting to conclude that the co-doping creates highly active sites for oxygen activation into a peroxy-species [128] whereas iron doping ends up with sites creating oxo species being less active in creating methyl radicals for OCM.

4.3 Conclusion

The purpose of the present work was to elucidate much along the demand of Hutchings [129] how electronic promoters may change the reaction pathway of the OCM reaction. Stimulated through the clear-cut model observation of Freund et al. we synthesized a polycrystalline form of model compound exhibiting the same sub-surface doping as evidently achieved in the model system of Freund. By carefully avoiding the formation of nanoparticles of the transition metal oxide we observed the predicted doping effect without interference from deep oxidation of the methane molecule. It was not our intention to explore the potential of this electronic effect with respect to selectivity and yield. We rather wanted to demonstrate by a catalytic experiment that as from chemical physics predicted an electronic doping effect exists for alkali earth oxides affecting oxygen activation. Its amplification by gold being activated through a specific interaction with MgO at iron-modified sites is an additional benefit. As the doping procedure is reproducible and the levels of doping species are low it is conceivable that the concept of homogeneous electronic doping of alkali earth oxides may find application for stabilization of realistic systems.

4.4 Experimental Section

Detailed information on catalyst synthesis, characterization, and catalytic tests is provided in the Supporting Information.

4.5 Supporting information

4.5.1 Experimental Details

4.5.1.1 Catalyst synthesis

4.5.1.1.1 Fe-MgO: Two Teflon autoclaves with a volume of 100 mL were filled each with 3 g MgO (Alfa Aesar 99.998 m.b. (ID#14564, batch number 24686) suspended in 69.5 mL distilled water. Subsequently, 0.537 mL of a 0.05 M FeSO_4 (Sigma) solution was added. The suspension was heated to 483 K for 3 hours in a microwave oven (Speedwave MWS-3+, Berghof Products + Instruments GmbH) at a pressure of 10 bar. The resulting material was isolated by filtration, washed with distilled water, and dried at 393 K in air for 12 h. For thermal treatment, the dried product was placed into a quartz crucible, which was located inside a quartz tube, and annealed in flowing Ar (150 mL/min) at 1173 K (heating rate 10 K/min) for 3 hours using a tube furnace (Carbolite). To remove segregated iron oxide particles, the resulting solid was washed in a mixture of 5 mL 0.1 M HNO_3 and 25 mL H_2O by stirring at 293 K for 1 hour. The washed and dried product was annealed again in flowing Ar (150 mL/min) at 1123 K (heating rate 5 K/min) for 3 hours.

4.5.1.1.2 Au-MgO: Two Teflon autoclaves with a volume of 100 mL were filled each with 3 g MgO (Alfa Aesar 99.998 m.b. (ID#14564, batch number 24686) suspended in 69.5 mL distilled water. Subsequently, 0.51 mL of a 0.015 M $\text{HAuCl}_4 \cdot x\text{H}_2\text{O}$ (Sigma) solution was added. The suspension was heated to 483 K for 3 hours in a microwave oven (Speedwave MWS-3+, Berghof Products + Instruments GmbH) at a pressure of 10 bar. The resulting material was isolated by filtration, washed with distilled water, and dried at 393 K in air for 12 h. For thermal treatment, the dried product was placed into a quartz crucible, which was located inside a quartz tube, and annealed in flowing Ar (150 mL/min) at 1173 K (heating rate 10 K/min) for 3 hours using a tube furnace (Carbolite). To remove segregated Au particles, the resulting solid was washed in a mixture of 5 mL 0.1 M aqua regia and 25 mL H_2O by stirring at 293 K for 1 hour. The washed and dried product was annealed again in flowing Ar (150 mL/min) at 1123 K (heating rate 5 K/min) for 3 hours. The resulting catalyst was stored under argon and freshly pre-treated before analysis or catalysis.

4.5.1.1.3 Au-Fe-MgO: Two Teflon autoclaves with a volume of 100 mL were filled each with 3 g MgO (Alfa Aesar 99.998 m.b. (ID#14564, batch number 24686) suspended in 69 mL distilled water. Subsequently, 0.508 mL of a 0.015 M $\text{HAuCl}_4 \cdot x\text{H}_2\text{O}$ (Sigma) solution, and 0.538 mL of 0.05 M FeSO_4 (Sigma) solution were added. The suspension was heated to 483 K for 3 hours in a microwave oven (Speedwave MWS-3+, Berghof Products + Instruments GmbH) at a pressure of 10 bar. The resulting material was isolated by

filtration, washed with distilled water, and dried at 393 K in air for 12 h. For thermal treatment, the dried product was placed into a quartz crucible, which was located inside a quartz tube, and annealed in flowing Ar (150 mL/min) at 1173 K (heating rate 10 K/min) for 3 hours using a tube furnace (Carbolite). To remove segregated iron oxide and Au particles, the resulting solid was washed in a mixture of 10 mL 0.1 M aqua regia and 20 mL H₂O by stirring at 293 K for 1 hour. The washed and dried product was annealed again in flowing Ar (150 mL/min) at 1123 K (heating rate 5 K/min) for 3 hours. The resulting catalyst was stored under argon and freshly pre-treated before analysis or catalysis.

The resulting catalysts were stored under argon and freshly pre-treated before analysis or catalysis.

4.5.1.2 X-ray diffraction

XRD was measured on a STOE STADI-P transmission diffractometer with a focusing primary Ge(111) monochromator and a linear PSD applying Cu K α ₁ radiation ($\lambda = 1.5406$ Å). The XRD data were analyzed by full pattern fitting using the TOPAS software (version 3, copyright 1999, 200 Bruker AXS).

4.5.1.3 Nitrogen adsorption

The surface area determination was carried out in a volumetric N₂ physisorption set-up (Autosorb-6-B, Quantachrome) at the temperature of liquid nitrogen. The sample was degassed in dynamic vacuum at a temperature of 473 K for 2 h prior to adsorption. The relative N₂ pressure was varied ($p/p_0=0.050.3$), and 11 data points were measured. The linear range of the adsorption isotherm was considered to calculate the specific surface area according to the BET method.

4.5.1.4 Atomic Absorption Spectroscopy (AAS)

The iron content was determined by Atomic Absorption Spectroscopy (AAS). Experiments were performed on a Perkin Elmer AAS 4100 spectrometer using a N₂O-acetylene flame and a wavelength of 271.9 nm. 250 mg of the catalyst were dissolved in 25 mL HNO₃ (65 % p.a.) and backfilled to 250 mL with distilled H₂O. Zero, 50 and 100 μ g iron were added to 25 mL of this solution, respectively, and backfilled to 50 mL with a solution of 5% HNO₃ in water.

4.5.1.5 Diffuse reflectance spectroscopy (DRS)

The in situ UV-VIS experiments were performed in the range between 200 and 800 nm using a Perkin Elmer Lambda 650 spectrometer equipped with a diffuse reflectance accessory (Praying Mantis, Harrick) complete with an environmental chamber attachment (Harrick

HVC-VUV-4) using Spectralon® as white standard. The catalysts were pretreated in situ at 923 K for 30 min in flowing Ar (20 mL/min), and measured in the same argon flow at room temperature.

4.5.1.6 Electron Paramagnetic Resonance (EPR)

EPR spectra were recorded at liquid nitrogen temperature on a Bruker ESR 300 E spectrometer equipped with a microwave bridge Bruker ER 042 MRH E. A Bruker ER 4116 DM resonator operating in the TE 102 mode (resonance frequency ≈ 9.5 GHz) was used. The spectra were recorded with a modulation frequency of 100 kHz and a microwave power of 2 mW. The frequency and g values were calibrated using the signal of Mn_{2+} ions ($g = 2.0007$, $A = -244$ MHz, $a = 55$ MHz) [130] present as impurity in MgO (3 ppm as determined by ICP-OES analysis). A small signal assigned to Cr^{3+} can also be observed with a g tensor of 1.98 (0.2 ppm as determined by ICP-OES analysis). [131] The samples were placed in a quartz cell equipped with Teflon Duran® valves and connected to a vacuum system that allows the dosing of gases. Before the EPR measurements, the MgO samples were activated at 1073 K under dynamic vacuum (10_{-6} – 10_{-7} mbar) for 3 hours.

4.5.1.7 Temperature-Programmed-Reduction-Oxidation (TPR-O) experiments

Temperature-programmed oxidation and reduction experiments were performed in a fixed-bed quartz reactor placed inside a tube furnace (Carbolite). The position of the catalyst inside the reactor was fixed applying a frit. The temperature was measured in the catalyst bed using a thermocouple (K-type). The feed was composed of 0.5 % O_2 or H_2 , respectively, in He and Ar, respectively. A flow rate of $90 \text{ mL}\cdot\text{min}^{-1}$ was applied. A mass of 600 mg of the catalyst with a 200–300 μm sieved fraction was used and diluted with 3 g SiC in order to improve the thermal conductivity in the catalyst bed. The measurements were performed applying a heating rate of $10 \text{ K}\cdot\text{min}^{-1}$. Hydrogen concentration in the gas phase was analyzed using a TCD detector (Rosemount Analytical) after the off-gas passed a molecular sieve trap to remove water. Before measurements, the catalysts were pretreated in $90 \text{ mL}\cdot\text{min}^{-1}$ Ar at 1073 K with a heating rate of $10 \text{ K}\cdot\text{min}^{-1}$ for 1 h to remove adsorbed water molecules and other adsorbates.

4.5.1.8 Catalytic measurements

The catalytic measurements were carried out in a laboratory quartz U-tube fixed bed reactor (4 mm inner diameter, 6 mm outer diameter, 26 cm length) applying reaction conditions as indicated in the main text. Gas analysis was performed by online gas chromatography (GC 6890A, Agilent). Nitrogen was used as internal standard to account for volume effects due to the high temperature.

4.5.1.9 Electron microscopy

Electron microscopy was carried out using a Cs-corrected FEI Titan 80-300 instrument operating at 300 kV in bright field high-resolution transmission electron microscopy (HRTEM) and high angle annular dark field scanning transmission electron microscopy (HAADF STEM) mode, respectively.

4.5.2 Diffuse reflectance spectroscopy

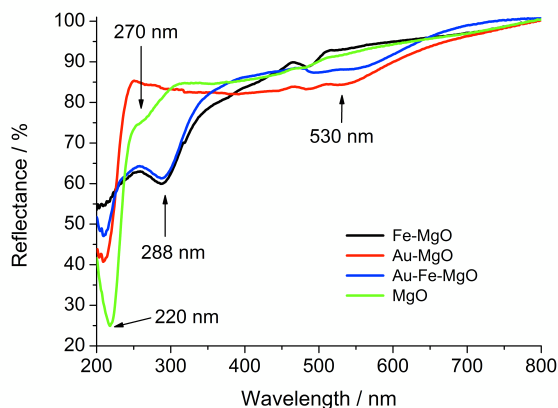


Figure S 4.1: UV-vis spectra of the doped catalysts measured in Ar at 293 K after pretreatment in Ar at 923 K.

4.5.3 EPR spectroscopy

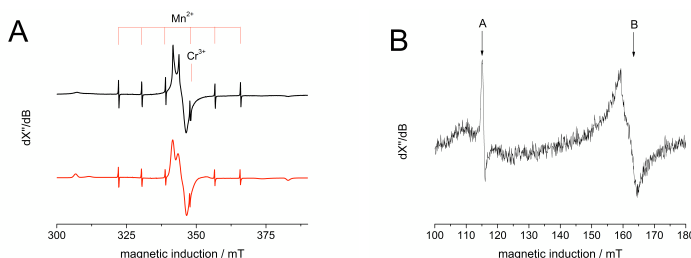


Figure S 4.2: EPR spectrum of Au-Fe-MgO after pretreatment at 1073 K under high vacuum, measured at 77 K, A) Experimental (black line) and simulated [84] spectrum (red line). B) Experimental spectra of Fe^{3+} at lower magnetic field. Both spectra are measured at a frequency of 9.63637 GHz.

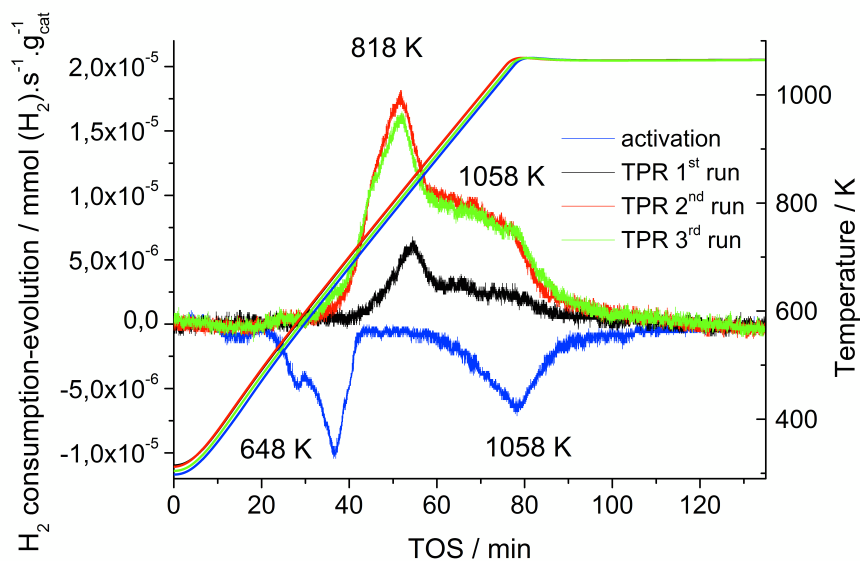
The experimental signal (Fig.4.2A, black line) at $g=2.0037$ is attributed to Fe^{3+} ions present in a cubic symmetry field, [132] which is also well reflected by the simulation of the spectrum ($g=2.0037$, $a=640$ MHz, $lwpp=1$ mT, and $D=-100$ MHz) using the Easypin package in MATLAB. [84] The species A and B at low fields (Fig. 4.2B) are assigned to Fe^{3+} ions in a coordination geometry of lower symmetry. These signals are usually assigned to Fe^{3+} in orthorhombic or tetragonal symmetry sites in MgO. [133] No sign of point defect can be found in the Au-Fe-MgO sample by EPR. [134,135]

4.5.4 Temperature-programmed-reduction-oxidation (TPR-TPO)

Table S 4.1: Hydrogen consumption in TPR (H_2 evolution during activation (negative values)).

	Hydrogen consumption (evolution) $/\mu\text{mol}(\text{H}_2)/(\text{s}\cdot\text{g}_{\text{cat}})$	Fraction of total Fe /%
Au-Fe-MgO	Fe content*: 7.20 $\mu\text{mol/g}$	
Activation	-0.25	-
TPR1	0.13	1.8
TPR2	0.48	6.7
TPR3	0.48	6.7
Au-Fe-MgO	Fe content*: 11.71 $\mu\text{mol/g}$	
Activation	-0.56	-
TPR1	0.81	6.9
TPR2	0.75	6.4
TPR3	0.74	6.3

* Analyzed by AAS.

**Figure S 4.3:** TPR-O of Fe-MgO. The blue line was measured during pretreatment in 90 $\text{mL}\cdot\text{min}^{-1}$ Ar applying a heating rate of 10 $\text{K}\cdot\text{min}^{-1}$.

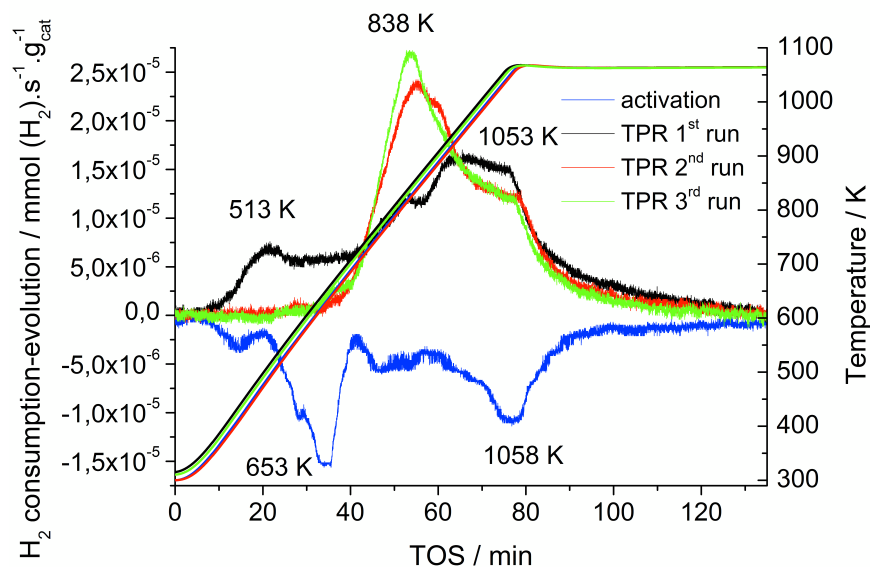


Figure S 4.4: TPR-O of Au-Fe-MgO. The blue line was measured during pretreatment in $90 \text{ mL} \cdot \text{min}^{-1}$ Ar applying a heating rate of $10 \text{ K} \cdot \text{min}^{-1}$.

4.5.5 Oxidative coupling of methane

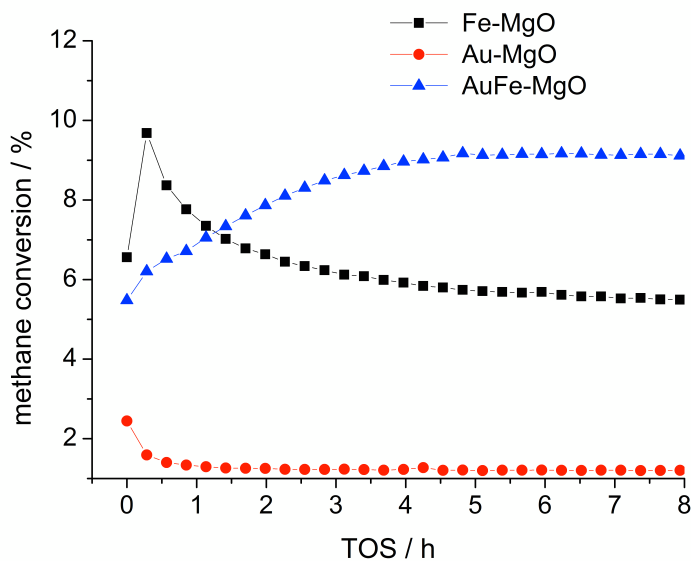


Figure S 4.5: Methane conversion in the oxidative coupling of methane as a function of time on stream (TOS) at $T=1023 \text{ K}$; $W/F= 0.0167 \text{ g} \cdot \text{s} \cdot \text{ml}^{-1}$; $\text{CH}_4/\text{O}_2/\text{N}_2=3/1/1$.

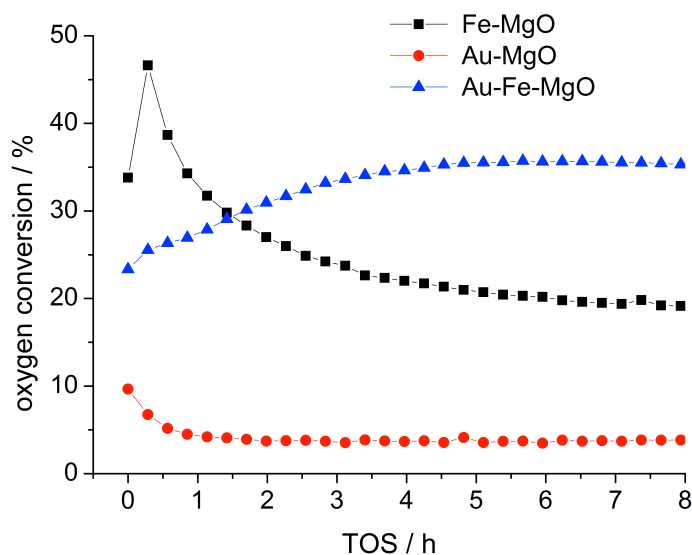


Figure S 4.6: Oxygen conversion in the oxidative coupling of methane as a function of time on stream (TOS) at $T=1023$ K; $W/F= 0.0167$ g·s·ml⁻¹; $CH_4/O_2/N_2=3/1/1$.

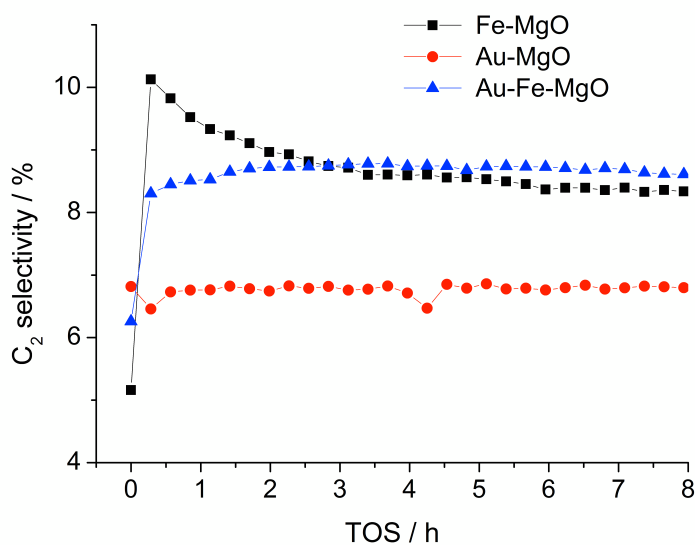


Figure S 4.7: Selectivity of the sum of ethane and ethene (C₂) in the oxidative coupling of methane as a function of time on stream (TOS) at $T=1023$ K; $W/F= 0.0167$ g·s·ml⁻¹; $CH_4/O_2/N_2=3/1/1$.

4.5.6 Electron microscopy

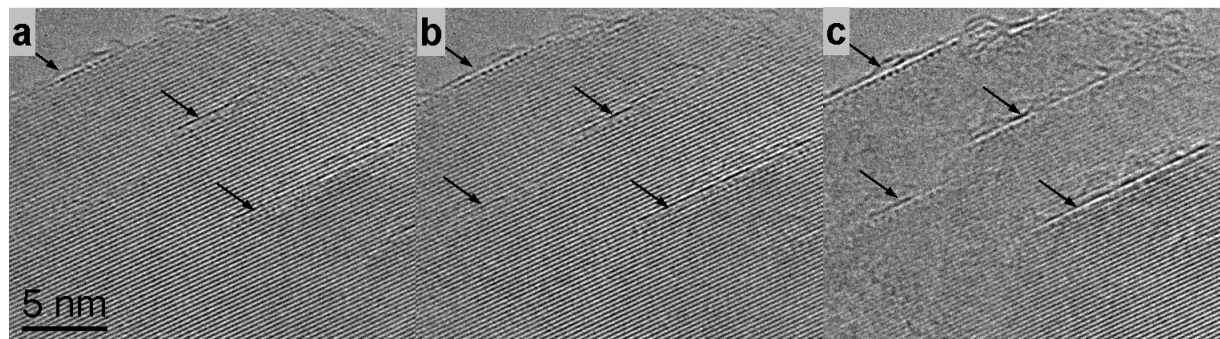


Figure S 4.8: Series of HRTEM images recorded at different defocus reveal the presence of strongly scattering atoms located at the steps in the Au-Fe-MgO catalyst after catalysis.

5. Conclusions

This thesis addresses the issue of structure-performance relationship of oxidative methane activation over a model MgO catalyst. The use of a well-defined and characterized model catalyst helped to gain new insight into the mechanism of the OCM reaction over alkaline earth metal oxides and we were able to clarify some open question still present in the literature.

In the selective oxidation of light alkanes, the key feature resides in the activation of the alkane itself, *i. e.* C-H bond breaking, whereby activated oxygen plays a major role. Activation steps require electron transfer, generally accepted or donated by the oxide catalyst in a redox mechanism. However in the case of alkaline earth oxides charge transfer between adsorbate and the catalyst is difficult due to the intrinsic properties of the oxide.

The surface structure of pure MgO offers specific configuration for the adsorption of methane. The di- or poly-hapto coordination of methane on strong acid-base pairs (generated from morphological defects) leads to the elongation of a C-H bond and therefore its polarization. Polarized adsorbed methane species are then able to transfer an electron to molecular oxygen approaching its vicinity. Molecular oxygen acts now as electron acceptor entity required for methane activation.

Depending on the state of the oxide surface and the predominant type of morphological defect, two different scenarios may occur for the methane activation. (i) On fresh MgO, a surface mediated coupling process leads to the direct formation of ethylene between two activated methane molecules adsorbed on the MgO surface next to each other, whereby two O-H and one C-C bond are created simultaneously. (ii) On densified MgO, *i. e.* after sintering, the active sites for the surface mediated coupling vanish and the surface configuration does not allow the direct formation of ethylene on the MgO surface. Polarized methane leads to the release of methyl radical in the gas phase in presence of molecular oxygen. Ethane is formed from the coupling of two methyl radicals in the gas phase. However ethane is not stable in the reaction conditions and the pyrolysis of ethane leads to the formation of carbon monoxide, while subsequent formation of ethylene through oxidative

dehydrogenation of ethane is only a minor side reaction if existent.

Acid-base methane activation can be changed to redox activation by doping with transition metal. Dilute solid solutions with high-valence dopant in ppm quantity like Fe^{3+} create a so-called electronic doping effect, whereby the dopant-induced charge transfer is relevant for the activation of methane and oxygen. This effect is duplicated by the presence of dispersed atomic gold on the MgO surface, where atomic gold act as an electron acceptor. In the case of electronic doping effect, the structure-performance dependency disappears and the reactivity is stable with TOS.

Activation of methane may occur through electronic doping effect involving charge transfer between the adsorbate and the surface. On pure alkaline earth oxide, methane is activated through heterolytic hydrogen atom abstraction. The main pathway for ethylene formation is a heterolytic surface-mediated-coupling of two activated methane molecules on the surface of the catalyst. In absence of active sites for ethylene formation, activated methane molecules are released in the gas phase as methyl radicals and ethane is formed through gas phase coupling. Ethane oxidative dehydrogenation is not the main pathway for the formation of ethylene.

The control of oxygen activation is likely to be the main challenge in the activation of methane. On pure MgO, activation of methane and activation of oxygen are codependent, and not as efficient as desired. On the opposite, on doped magnesium oxide, oxygen is activated too lightly and its total consumption limits the performance of the OCM reaction. A better control of oxygen activation is most probably the key point for a better methane conversion and C_{2+} selectivity in the oxidative coupling of methane. This issue could be tackled from an engineering point of view, for example by distributing oxygen feed along the catalytic bed using either a stage reactor or an oxygen permeable membrane.

Bibliography

- [1] G. J. Macdonald. The future of methane as an energy resource. *Annual Review of Energy*, 15:53–83, 1990 1990.
- [2] G. E. Keller and M. M. Bhasin. Synthesis of ethylene via oxidative coupling of methane : I. determination of active catalysts. *Journal of Catalysis*, 73(1):9–19, 1982.
- [3] W. Hinsén and M. Baerns. Oxidative coupling of methane to C₂-hydrocarbons in the presence of different catalysts. *Chemiker-Zeitung*, 107(7-8):223–226, 1983.
- [4] D. J. Driscoll, W. Martir, J. X. Wang, and J. H. Lunsford. Formation of gas-phase methyl radicals over magnesium oxide. *Journal of the American Chemical Society*, 107(1):58–63, 1985.
- [5] T. Ito and J. H. Lunsford. Synthesis of ethylene and ethane by partial oxidation of methane over lithium-doped magnesium oxide. *Nature*, 314(6013):721–722, 1985.
- [6] T. Ito, J. Wang, C. H. Lin, and J. H. Lunsford. Oxidative dimerization of methane over a lithium-promoted magnesium oxide catalyst. *Journal of the American Chemical Society*, 107(18):5062–5068, 1985.
- [7] E. V. Kondratenko and M. Baerns. *Oxidative Coupling of Methane*. Wiley-VCH Verlag GmbH & Co. KGaA, 2008.
- [8] U. Zavyalova, M. Holena, R. Schlögl, and M. Baerns. Statistical analysis of past catalytic data on oxidative methane coupling for new insights into the composition of high-performance catalysts. *ChemCatChem*, 3(12):1935–1947, 2011.
- [9] Z. Zhang, X. E. Verykios, and M. Baerns. Effect of electronic-properties of catalysts for the oxidative coupling of methane on their selectivity and activity. *Catalysis Reviews-Science and Engineering*, 36(3):507–556, 1994.

- [10] H. Schwarz, M. Geske, C. Franklin G., R. Schlögl, and R. Horn. Fuel-rich methane oxidation in a high-pressure flow reactor studied by optical-fiber laser-induced fluorescence, multi-species sampling profile measurements and detailed kinetic simulations. *Combustion and Flame*, 161(7):1688–1700, 2014.
- [11] L. Mleczko and M. Baerns. Catalytic oxidative coupling of methane-reaction engineering aspects and process schemes. *Fuel Processing Technology*, 42(23):217–248, 1995.
- [12] D. Schweer, L. Mleczko, and M. Baerns. OCM in a fixed-bed reactor: limits and perspectives. *Catalysis Today*, 21(2-3):357–369, 1994.
- [13] N. W. Cant, E. M. Kennedy, and P. F. Nelson. Magnitude and origin of the deuterium kinetic isotope effect during methane coupling and related reactions over lithium/magnesium oxide catalysts. *The Journal of Physical Chemistry*, 97(7):1445–1450, 1993.
- [14] C. Shi, M. Xu, M. P. Rosynek, and J. H. Lunsford. Origin of kinetic isotope effects during the oxidative coupling of methane over a lithium(1+)/magnesia catalyst. *The Journal of Physical Chemistry*, 97(1):216–222, 1993.
- [15] P. M. Couwenberg, Q. Chen, and G. B. Marin. Kinetics of a gas-phase chain reaction catalyzed by a solid: The oxidative coupling of methane over Li/MgO-based catalysts. *Industrial & Engineering Chemistry Research*, 35(11):3999–4011, 1996.
- [16] C. Shi, M. Hatano, and J. H. Lunsford. A kinetic model for the oxidative coupling of methane over Li/MgO catalysts. *Catalysis Today*, 13(23):191–199, 1992.
- [17] V. R. Choudhary and V. H. Rane. Acidity/basicity of rare-earth oxides and their catalytic activity in oxidative coupling of methane to C₂-hydrocarbons. *Journal of Catalysis*, 130(2):411–422, 1991.
- [18] A. M. Maitra, I. Campbell, and R. J. Tyler. Influence of basicity on the catalytic activity for oxidative coupling of methane. *Applied Catalysis A: General*, 85(1):27–46, 1992.
- [19] E. Garrone, A. Zecchina, and F. S. Stone. Anionic intermediates in surface processes leading to O₂⁻ formation on magnesium oxide. *Journal of Catalysis*, 62(2):396–400, 1980.
- [20] E. Knoezinger, O. Diwald, and M. Sterrer. Chemical vapour deposition - a new approach to reactive surface defects of uniform geometry on high surface area magnesium oxide. *Journal of Molecular Catalysis A: Chemical*, 162(1-2):83–95, 2000.

- [21] J.-L. Dubois and C. J. Cameron. Common features of oxidative coupling of methane cofeed catalysts. *Applied Catalysis*, 67(1):49–71, 1990.
- [22] O. V. Buyevskaya, M. Rothaemel, H. W. Zanthoff, and M. Baerns. Transient studies on the role of oxygen activation in the oxidative coupling of methane over Sm_2O_3 , $\text{Sm}_2\text{O}_3/\text{MgO}$, and MgO catalytic surfaces. *Journal of Catalysis*, 150(1):71–80, 1994.
- [23] K. P. Peil, J. G. Goodwin, and G. Marcelin. An examination of the oxygen pathway during methane oxidation over a lithium/magnesia catalyst. *The Journal of Physical Chemistry*, 93(16):5977–5979, 1989.
- [24] H. Borchert and M. Baerns. The effect of oxygen-anion conductivity of metal-oxide doped lanthanum oxide catalysts on hydrocarbon selectivity in the oxidative coupling of methane. *Journal of Catalysis*, 168(2):315–320, 1997.
- [25] H. Kathrein, F. Freund, and J. Nagy. O^- -ions and their relation to traces of H_2O and CO_2 in magnesium oxide an EPR study. *Journal of Physics and Chemistry of Solids*, 45(11-12):1155–1163, 1984.
- [26] M. Boudart, A. Delbouille, E. G. Derouane, V. Indovina, and A. B. Walters. Activation of hydrogen at 78.deg.K on paramagnetic centers of magnesium oxide. *Journal of the American Chemical Society*, 94(19):6622–6630, 1972.
- [27] R. Martens, H. Gentsch, and F. Freund. Hydrogen release during the thermal decomposition of magnesium hydroxide to magnesium oxide. *Journal of Catalysis*, 44(3):366–372, 1976.
- [28] H. B. Zhang, G. D. Lin, H. L. Wan, Y. D. Liu, W. Z. Weng, J. X. Cai, Y. F. Shen, and K. R. Tsai. Active-oxygen species on non-reducible rare-earth-oxide-based catalysts in oxidative coupling of methane. *Catalysis Letters*, 73(2-4):141–147, 2001.
- [29] M. Sterrer, T. Berger, S. Stankic, O. Diwald, and E. Knozinger. Spectroscopic properties of trapped electrons on the surface of MgO nanoparticles. *Chemphyschem*, 5(11):1695–1703, 2004.
- [30] J. L. Boldu, E. Munoz, X. Bokhimi, O. Novaro, T. Lopez, and R. Gomez. Spectroscopic studies of sol-gel Li/MgO catalysts. *Langmuir*, 15(1):32–35, 1998.
- [31] C. L. Bothe-Almquist, R. P. Ettireddy, A. Bobst, and P. G. Smirniotis. An XRD, XPS, and EPR study of Li/MgO catalysts: Case of the oxidative methylation of acetonitrile to acrylonitrile with CH_4 . *Journal of Catalysis*, 192(1):174–184, 2000.

- [32] U. Zavyalova, M. Geske, R. Horn, G. Weinberg, W. Frandsen, M. Schuster, and R. Schlögl. Morphology and microstructure of Li/MgO catalysts for the oxidative coupling of methane. *ChemCatChem*, 3(6):949–959, 2011.
- [33] U. Zavyalova, R. Horn, F. Girgsdies, T. Risse, H. J. Freund, K. P. Dinse, and R. Schlögl. Hierarchically structured mesoporous defect rich Li/MgO materials prepared by gel combustion synthesis as catalysts for oxidative coupling of methane. *Advanced Functional Materials*, submitted, 2010.
- [34] U. Zavyalova, G. Weinberg, W. Frandsen, F. Girgsdies, T. Risse, K. Peter Dinse, R. Schlögl, and R. Horn. Lithium as a modifier for morphology and defect structure of porous magnesium oxide materials prepared by gel combustion synthesis. *ChemCatChem*, 3(11):1779–1788, 2011.
- [35] E. Lucas, S. Decker, A. Khaleel, A. Seitz, S. Fultz, A. Ponce, W. F. Li, C. Carnes, and K. J. Klabunde. Nanocrystalline metal oxides as unique chemical reagents/sorbents. *Chemistry-a European Journal*, 7(12):2505–2510, 2001.
- [36] J. V. Stark, D. G. Park, I. Lagadic, and K. J. Klabunde. Nanoscale metal oxide particles/clusters as chemical reagents. unique surface chemistry on magnesium oxide as shown by enhanced adsorption of acid gases (sulfur dioxide and carbon dioxide) and pressure dependence. *Chemistry of Materials*, 8(8):1904–1912, 1996.
- [37] R. Hacquart, J.-M. Krafft, G. Costentin, and J. Jupille. Evidence for emission and transfer of energy from excited edge sites of MgO smokes by photoluminescence experiments. *Surface Science*, 595(1-3):172–182, 2005.
- [38] T. Tashiro, T. Watanabe, M. Kawasaki, K. Toi, and T. Ito. Partial oxidation of methane with oxygen over magnesium-oxide at low-temperatures. *Journal of the Chemical Society-Faraday Transactions*, 89(8):1263–1269, 1993.
- [39] T. Ito, T. Tashiro, T. Watanabe, M. Kawasaki, K. Toi, and H. Kobayashi. Adsorption of methane on magnesium-oxide surfaces under ultraviolet-irradiation. *Journal of the Chemical Society-Faraday Transactions*, 86(24):4071–4075, 1990.
- [40] J. S. J. Hargreaves, G. J. Hutchings, R. W. Joyner, and C. J. Kiely. The relationship between catalyst morphology and performance in the oxidative coupling of methane. *Journal of Catalysis*, 135(2):576–595, 1992.
- [41] I. M. Mellor, A. Burrows, S. Coluccia, J. S. J. Hargreaves, R. W. Joyner, C. J. Kiely, G. Martra, M. Stockenhuber, and W. M. Tang. Probing possible structure sensitivity in the exchange of isotopic oxygen with the surface of MgO. *Journal of Catalysis*, 234(1):14–23, 2005.

- [42] J. H. Lunsford, M. D. Cisneros, P. G. Hinson, Y. Tong, and H. Zhang. Oxidative dimerization of methane over well defined lithium-promoted magnesium oxide catalysts. *Faraday Discussions of the Chemical Society*, 87:13–21, 1989.
- [43] G. Spoto, E. N. Gribov, G. Ricchiardi, A. Damin, D. Scarano, S. Bordiga, C. Lamberti, and A. Zecchina. Carbon monoxide MgO from dispersed solids to single crystals: a review and new advances. *Progress in Surface Science*, 76(3-5):71–146, 2004.
- [44] E. Garrone, A. Zecchina, and F. S. Stone. An experimental and theoretical evaluation of surface-states in MgO and other alkaline-earth oxides. *Philosophical Magazine B-Physics of Condensed Matter Statistical Mechanics Electronic Optical and Magnetic Properties*, 42(5):683–703, 1980.
- [45] C. Chizallet, G. Costentin, H. Lauron-Pernot, J.-M. Krafft, M. Che, F. Delbecq, and P. Sautet. Assignment of photoluminescence spectra of MgO powders: TD-DFT cluster calculations combined to experiments. part I: Structure effects on dehydroxylated surfaces. *The Journal of Physical Chemistry C*, 112(42):16629–16637, 2008.
- [46] M.-L. Bailly, G. Costentin, H. Lauron-Pernot, J. M. Krafft, and M. Che. Physicochemical and in situ photoluminescence study of the reversible transformation of oxide ions of low coordination into hydroxyl groups upon interaction of water and methanol with MgO. *The Journal of Physical Chemistry B*, 109(6):2404–2413, 2004.
- [47] M.-L. Bailly, G. Costentin, J.-M. Krafft, and M. Che. Discrimination of MgO ions by means of an improved in situ photoluminescence cell and of propyne as probe molecule. *Catalysis Letters*, 92(3):101–105, 2004.
- [48] Petra Käßner and Manfred Baerns. Comparative characterization of basicity and acidity of metal oxide catalysts for the oxidative coupling of methane by different methods. *Applied Catalysis A: General*, 139(1-2):107–129, 1996.
- [49] M. C. Wu, C. M. Truong, K. Coulter, and D. W. Goodman. Role of F centers in the oxidative coupling of methane to ethane over lithium-promoted magnesium oxide catalysts. *Journal of the American Chemical Society*, 114(19):7565–7567, 1992.
- [50] P. L. Gai, J. M. Montero, A. F. Lee, K. Wilson, and E. D. Boyes. In situ aberration corrected-transmission electron microscopy of magnesium oxide nanocatalysts for biodiesels. *Catalysis Letters*, 132(1-2):182–188, 2009.
- [51] M. C. Paganini, M. Chiesa, E. Giamello, S. Coluccia, G. Martra, D. M. Murphy, and G. Pacchioni. Colour centres at the surface of alkali-earth oxides. a new hypothesis on the location of surface electron traps. *Surface Science*, 421(3):246–262, 1999.

- [52] Y. Osada, S. Koike, T. Fukushima, S. Ogasawara, T. Shikada, and T. Ikariya. Oxidative coupling of methane over $\text{Y}_2\text{O}_3\text{CaO}$ catalysts. *Applied Catalysis*, 59(1):59–74, 1990.
- [53] E. N. Voskresenskaya, V. G. Roguleva, and A. G. Anshits. Oxidant activation over structural defects of oxide catalysts in oxidative methane coupling. *Catalysis Reviews: Science and Engineering*, 37(1):101–143, 1995.
- [54] Y. Cui, X. Shao, M. Baldofski, J. Sauer, N. Nilius, and H.-J. Freund. Adsorption, activation, and dissociation of oxygen on doped oxides. *ANGEWANDTE CHEMIE-INTERNATIONAL EDITION*, 52(43):11385–11387, OCT 18 2013.
- [55] P. Schwach, W. Frandsen, M. G. Willinger, R. Schlögl, and A. Trunschke. Structure sensitivity of the oxidative activation of methane over MgO model catalysts: I. kinetic study. *Journal of Catalysis*, submitted, 2014.
- [56] P. Schwach, N. Hamilton, L. Thum, T. Lunkenbein, M. Eichelbaum, R. Schlögl, and A. Trunschke. Structure sensitivity of the oxidative activation of methane over MgO model catalysts: II. nature of active sites and reaction mechanism. *Journal of Catalysis*, submitted, 2014.
- [57] J. S. J. Hargreaves, G. J. Hutchings, R. W. Joyner, and C. J. Kiely. The relationship between catalyst morphology and performance in the oxidative coupling of methane. *Journal of Catalysis*, 135(2):576–595, 1992.
- [58] T. Ito, T. Watanabe, T. Tashiro, and K. Toi. Reaction of preadsorbed methane with oxygen over magnesium-oxide at low-temperatures. *Journal of the Chemical Society-Faraday Transactions I*, 85:2381–2395, 1989.
- [59] M. Sterrer, E. Fischbach, M. Heyde, N. Nilius, H.-P. Rust, T. Risse, and H.-J. Freund. Electron paramagnetic resonance and scanning tunneling microscopy investigations on the formation of F^+ and F^0 color centers on the surface of thin $\text{MgO}(001)$ films. *The Journal of Physical Chemistry B*, 110(17):8665–8669, 2006.
- [60] M. Sterrer, M. Heyde, M. Novicki, N. Nilius, T. Risse, H.-P. Rust, G. Pacchioni, and H.-J. Freund. Identification of color centers on $\text{MgO}(001)$ thin films with scanning tunneling microscopy. *The Journal of Physical Chemistry B*, 110(1):46–49, 2006.
- [61] M. Sterrer, E. Fischbach, T. Risse, and H.-J. Freund. Geometric characterization of a singly charged oxygen vacancy on a single-crystalline $\text{MgO}(001)$ film by electron paramagnetic resonance spectroscopy. *Physical Review Letters*, 94(18):186101, 2005.

- [62] H.-M. Benia, P. Myrach, A. Gonchar, T. Risse, N. Nilius, and H.-J. Freund. Electron trapping in misfit dislocations of MgO thin films. *Physical Review B*, 81(24):241415, 2010.
- [63] S. Utamapanya, K. J. Klabunde, and J. R. Schlup. Nanoscale metal oxide particles/clusters as chemical reagents. synthesis and properties of ultrahigh surface area magnesium hydroxide and magnesium oxide. *Chemistry of Materials*, 3(1):175–181, 1991.
- [64] F. Kapteijn and J. A. Moulijn. Laboratory catalytic reactors: Aspects of catalyst testing. In *Handbook of Heterogeneous Catalysis*. Wiley-VCH Verlag GmbH & Co. KGaA, 2008.
- [65] S. Stankic, M. Cottura, D. Demaille, C. Noguera, and J. Jupille. Nucleation and growth concepts applied to the formation of a stoichiometric compound in a gas phase: The case of MgO smoke. *Journal of Crystal Growth*, 329(1):52–56, 2011.
- [66] O. Korup, S. Mavlyankariyev, M. Geske, C. F. Goldsmith, and R. Horn. Measurement and analysis of spatial reactor profiles in high temperature catalysis research. *Chemical Engineering and Processing: Process Intensification*, 50(10):998–1009, 2011.
- [67] S. J. Korf, J. A. Roos, N. A. de Bruijn, J. G. van Ommen, and J. R. H. Ross. Influence of CO₂ on the oxidative coupling of methane over a lithium promoted magnesium oxide catalyst. *Journal of the Chemical Society, Chemical Communications*, (19):1433–1434, 1987.
- [68] B. Tope, Y. Zhu, and J. A. Lercher. Oxidative dehydrogenation of ethane over Dy₂O₃/MgO supported LiCl containing eutectic chloride catalysts. *Catalysis Today*, 123(14):113–121, 2007.
- [69] K. Aika and J. H. Lunsford. Surface reactions of oxygen ions. i. dehydrogenation of alkanes by oxygen(1-) ions on magnesium oxide. *The Journal of Physical Chemistry*, 81(14):1393–1398, 1977.
- [70] J. H. Lunsford. The catalytic oxidative coupling of methane. *Angewandte Chemie International Edition in English*, 34(9):970–980, 1995.
- [71] K. P. Peil, J. G. Goodwin Jr, and G. Marcelin. Surface phenomena during the oxidative coupling of methane over Li/MgO. *Journal of Catalysis*, 131(1):143–155, 1991.
- [72] E. Iwamatsu and K.-I. Aika. Kinetic analysis of the oxidative coupling of methane over Na⁺-doped MgO. *Journal of Catalysis*, 117(2):416–431, 1989.

- [73] Y. K. Kao, L. Lei, and Y. S. Lin. A comparative simulation study on oxidative coupling of methane in fixed-bed and membrane reactors. *Industrial & Engineering Chemistry Research*, 36(9):3583–3593, 1997.
- [74] R. H. Nibbelke, J. Scheerova, M. H. J. M. Decroon, and G. B. Marin. The oxidative coupling of methane over mgo-based catalysts: A steady-state isotope transient kinetic analysis. *Journal of Catalysis*, 156(1):106–119, 1995.
- [75] J. Sun, J. W. Thybaut, and G. B. Marin. Microkinetics of methane oxidative coupling. *Catalysis Today*, 137(1):90–102, 2008.
- [76] J. W. Thybaut, J. Sun, L. Olivier, A. C. Van Veen, C. Mirodatos, and G. B. Marin. Catalyst design based on microkinetic models: Oxidative coupling of methane. *Catalysis Today*, 159(1):29–36, 2011.
- [77] G. J. Tjatjopoulos and I. A. Vasalos. A mechanistic kinetic model for oxidative coupling of methane over Li/MgO catalysts. *Catalysis Today*, 13(23):361–370, 1992.
- [78] J. M. N. van Kasteren, J. W. M. H. Geerts, and K. van der Wiele. Methane oxidative coupling using Li/MgO catalysts: The importance of consecutive reactions. In K. J. Jens A. Holmen and S. Kolboe, editors, *Studies in Surface Science and Catalysis*, volume Volume 61, pages 139–146. Elsevier, 1991.
- [79] Y. Tong and J. H. Lunsford. Mechanistic and kinetic studies of the reactions of gas-phase methyl radicals with metal oxides. *Journal of the American Chemical Society*, 113(13):4741–4746, 1991/06/01 1991.
- [80] M. T. Xu, T. H. Ballinger, and J. H. Lunsford. Quantitative studies of methyl radicals reacting with metal-oxides. *Journal of Physical Chemistry*, 99(39):14494–14499, 1995.
- [81] A. M. Ferrari, S. Huber, H. Knozinger, K. M. Neyman, and N. Rosch. FTIR spectroscopic and density functional model cluster studies of methane adsorption on MgO. *Journal of Physical Chemistry B*, 102(23):4548–4555, Jun 4 1998.
- [82] M. Anpo and M. Che. Applications of photoluminescence techniques to the characterization of solid surfaces in relation to adsorption, catalysis, and photocatalysis. In W. O. Haag, B. C. Gates, and H. Knozinger, editors, *Advances in Catalysis, Vol 44*, volume 44 of *Advances in Catalysis*, pages 119–257. 1999.
- [83] C. Chizallet, G. Costentin, J.-M. Krafft, H. Lauron-Pernot, and M. Che. Kinetic model of energy transfer processes between low-coordinated ions on MgO by photoluminescence decay measurements, 2006.

- [84] S. Stoll and A. Schweiger. EasySpin, a comprehensive software package for spectral simulation and analysis in EPR. *Journal of Magnetic Resonance*, 178(1):42–55, 2006.
- [85] K. I. Hadjiivanov and G. N. Vayssilov. Characterization of oxide surfaces and zeolites by carbon monoxide as an IR probe molecule. In *Advances in Catalysis, Vol 47*, volume 47 of *Advances in Catalysis*, pages 307–511. Academic Press Inc, San Diego, 2002.
- [86] M. A. Babaeva, D. S. Bystrov, A. Y. Kovalgin, and A. A. Tsyganenko. CO interaction with the surface of thermally activated CaO and MgO. *Journal of Catalysis*, 123(2):396–416, 1990.
- [87] E. Guglielminotti, S. Coluccia, E. Garrone, L. Cerruti, and A. Zecchina. Infrared study of CO adsorption on magnesium oxide. *Journal of the Chemical Society, Faraday Transactions 1: Physical Chemistry in Condensed Phases*, 75:96–108, 1979.
- [88] N. S. Hush and M. L. Williams. Carbon monoxide bond length, force constant and infrared intensity variations in strong electric fields: Valence-shell calculations, with applications to properties of adsorbed and complexed CO. *Journal of Molecular Spectroscopy*, 50(13):349–368, 1974.
- [89] G. Pacchioni, G. Cogliandro, and P. S. Bagus. Molecular orbital cluster model study of bonding and vibrations of CO adsorbed on MgO surface. *International Journal of Quantum Chemistry*, 42(5):1115–1139, 1992.
- [90] R. Soave and G. Pacchioni. New bonding mode of CO on stepped MgO surfaces from density functional cluster model calculations. *Chemical Physics Letters*, 320(34):345–351, 2000.
- [91] C. Trionfetti, I. V. Babich, K. Seshan, and L. Lefferts. Presence of lithium ions in MgO lattice: Surface characterization by infrared spectroscopy and reactivity towards oxidative conversion of propane. *Langmuir*, 24(15):8220–8228, 2008.
- [92] C. Li, G. Li, and Q. Xin. FT-IR spectroscopic studies of methane adsorption on magnesium oxide. *The Journal of Physical Chemistry*, 98(7):1933–1938, 1994/02/01 1994.
- [93] N. Sheppard and D. J. C. Yates. Changes in the infra-red spectra of molecules due to physical adsorption. *Proceedings of the Royal Society of London. Series A. Mathematical and Physical Sciences*, 238(1212):69–89, 1956.
- [94] E. Knözinger, K.-H. Jacob, S. Singh, and P. Hofmann. Hydroxyl groups as IR active surface probes on MgO crystallites. *Surface Science*, 290(3):388–402, 1993.

- [95] J. D. Levine and P. Mark. Theory and observation of intrinsic surface states on ionic crystals. *Physical Review*, 144(2):751, 1966.
- [96] S. Coluccia, A. M. Deane, and A. J. Tench. Photoluminescent spectra of surface states in alkaline earth oxides. *Journal of the Chemical Society, Faraday Transactions 1: Physical Chemistry in Condensed Phases*, 74(0):2913–2922, 1978.
- [97] S. Benedetti, H. M. Benia, N. Nilius, S. Valeri, and H. J. Freund. Morphology and optical properties of MgO thin films on Mo(001). *Chemical Physics Letters*, 430(46):330–335, 2006.
- [98] P. V. Sushko and A. L. Shluger. Electronic structure of excited states at low-coordinated surface sites of MgO. *Surface Science*, 421(3):L157–L165, 1999.
- [99] S. Coluccia, A. J. Tench, and R. L. Segall. Surface-structure and surface-states in magnesium-oxide powders. *Journal of the Chemical Society-Faraday Transactions I*, 75:1769, 1979.
- [100] E. Giamello, E. Garrone, P. Ugliengo, M. Che, and A. J. Tench. Experimental-evidence for the hyperfine interaction between a surface superoxide species on MgO and a neighboring hydroxylic proton. *Journal of the Chemical Society-Faraday Transactions I*, 85:3987–3994, 1989.
- [101] M. Che and A. J. Tench. Characterization and reactivity of molecular-oxygen species on oxide surfaces. *Advances in Catalysis*, 32:1–148, 1983.
- [102] E. Giamello, P. Ugliengo, and E. Garrone. Superoxide ions formed on MgO through the agency of presorbed molecules. part 1.-spectroscopic electron spin resonance features. *Journal of the Chemical Society, Faraday Transactions 1: Physical Chemistry in Condensed Phases*, 85(6):1373–1382, 1989.
- [103] D. M. Murphy, R. D. Farley, I. J. Purnell, C. C. Rowlands, A. R. Yacob, M. C. Paganini, and E. Giamello. Surface defect sites formed on partially and fully dehydrated MgO: An EPR/ENDOR study. *Journal of Physical Chemistry B*, 103(11):1944–1953, Mar 1999.
- [104] O. Diwald and E. Knozinger. Intermolecular electron transfer on the surface of MgO nanoparticles. *Journal of Physical Chemistry B*, 106(13):3495–3502, 2002.
- [105] M. C. Paganini, M. Chiesa, P. Martino, E. Giamello, and E. Garrone. EPR study of the surface basicity of calcium oxide. 2: The interaction with alkanes. *Journal of Physical Chemistry B*, 107(11):2575–2580, Mar 20 2003.

- [106] N. H. de Leeuw, G. W. Watson, and S. C. Parker. Atomistic simulation of the effect of dissociative adsorption of water on the surface structure and stability of calcium and magnesium oxide. *The Journal of Physical Chemistry*, 99(47):17219–17225, 1995/11/01 1995.
- [107] Z. Hu, B. Li, X.-Y. Sun, and H. Metiu. Chemistry of doped oxides: The activation of surface oxygen and the chemical compensation effect. *Journal of Physical Chemistry C*, 115(7):3065–3074, Feb 24 2011.
- [108] H. Metiu, S. Chretien, Z. Hu, B. Li, and X. Sun. Chemistry of lewis acid-base pairs on oxide surfaces. *Journal of Physical Chemistry C*, 116(19):10439–10450, May 17 2012.
- [109] X. Sun, B. Li, and H. Metiu. Methane dissociation on Li-, Na-, K-, and Cu-doped flat and stepped CaO(001). *Journal of Physical Chemistry C*, 117(14):7114–7122, Apr 11 2013.
- [110] M. C. Paganini, M. Chiesa, P. Martino, S. Livraghi, and E. Giamello. An EPR study of the surface reactivity of CaO and a comparison with that of MgO. In A. Gamble, C. Colella, and S. Coluccia, editors, *Oxide Based Materials: New Sources, Novel Phases, New Applications*, volume 155 of *Studies in Surface Science and Catalysis*, pages 441–449. 2005.
- [111] M. Iwamoto and J. H. Lunsford. Surface reactions of oxygen ions. 5. oxidation of alkanes and alkenes by O_2^- on magnesium oxide. *The Journal of Physical Chemistry*, 84(23):3079–3084, 1980.
- [112] K. Refson, R. A. Wogelius, D. G. Fraser, M. C. Payne, M. H. Lee, and V. Milman. Water chemisorption and reconstruction of the MgO surface. *Physical Review B*, 52(15):10823–10826, 1995.
- [113] D. Costa, C. Chizallet, B. Ealet, J. Goniakowski, and F. Finocchi. Water on extended and point defects at MgO surfaces. *Journal of Chemical Physics*, 125(5), 2006.
- [114] D. R. Sempolinski and W. D. Kingery. Ionic-conductivity and magnesium vacancy mobility in magnesium-oxide. *JOURNAL OF THE AMERICAN CERAMIC SOCIETY*, 63(11-1):664–669, 1980.
- [115] D. R. Sempolinski, W. D. Kingery, and H. L. Tuller. Electronic conductivity of single crystalline magnesium-oxide. *JOURNAL OF THE AMERICAN CERAMIC SOCIETY*, 63(11-1):669–675, 1980.

- [116] L. Leveles, K. Seshan, J. A. Lercher, and L. Lefferts. Oxidative conversion of propane over lithium-promoted magnesia catalyst: I. kinetics and mechanism. *Journal of Catalysis*, 218(2):296–306, 2003.
- [117] P. Schwach, M.-G. Willinger, A. Trunschke, and R. Schlögl. Methane coupling over magnesium oxide: How doping can work. *Angewandte Chemie International Edition*, 52(43):11381–11384, 2013.
- [118] H. Schwarz. Chemistry with methane: Concepts rather than recipes. *Angewandte Chemie International Edition*, 50(43):10096–10115, 2011.
- [119] C. Hammond, S. Conrad, and I. Hermans. Oxidative methane upgrading. *ChemSusChem*, 5(9):1668–1686, 2012.
- [120] D. Beruto, A. W. Searcy, R. Botter, and M. Giordani. Thermodynamics and kinetics of water vapor chemisorption and solubility in nanometric and single-crystal magnesia particles during sintering. *The Journal of Physical Chemistry*, 97(36):9201–9205, 1993.
- [121] K. Blick, T. D. Mitrelias, J. S. J. Hargreaves, G. J. Hutchings, R. W. Joyner, C. J. Kiely, and F. E. Wagner. Methane oxidation using Au/MgO catalysts. *Catalysis Letters*, 50(3-4):211–218, 1998.
- [122] G. Lehmann. Ligand field and charge transfer spectra of Fe(3)-O complexes. *Z. Phys. Chem. Neue Folge*, 72:279, 1970.
- [123] C. F. Bohren and D. R. Huffman. *Absorption and Scattering of Light by Small Particles*. John Wiley and Sons, New York, 1983.
- [124] K. C. Grabar, R. G. Freeman, M. B. Hommer, and M. J. Natan. Preparation and characterization of Au colloid monolayers. *Analytical Chemistry*, 67(4):735–743, 1995.
- [125] B. V. King and F. Freund. Surface charges and subsurface space-charge distribution in magnesium oxides containing dissolved traces of water. *Physical Review B*, 29(10):5814–5824, 1984.
- [126] J. S. J. Hargreaves, G. J. Hutchings, R. W. Joyner, and C. J. Kiely. Relationship between morphology and catalytic performance of lithium and gold doped magnesium oxide catalysts for the oxidative coupling of methane. *Catalysis Today*, 13(2-3):401–407, 1992.
- [127] M. J. Hytch, E. Snoeck, and R. Kilaas. Quantitative measurement of displacement and strain fields from HRTEM micrographs. *Ultramicroscopy*, 74(3):131–146, 1998.

- [128] P. Landon, P. J. Collier, A. J. Papworth, C. J. Kiely, and G. J. Hutchings. Direct formation of hydrogen peroxide from H_2/O_2 using a gold catalyst. *Chemical Communications*, 0(18):2058–2059, 2002.
- [129] G. J. Hutchings. Promotion in heterogeneous catalysis: A topic requiring a new approach? *Catalysis Letters*, 75(1-2):1–12, 2001.
- [130] W. Low. Paramagnetic resonance spectrum of manganese in cubic MgO and CaF_2 . *Phys. Rev.*, 105:793–800, 1957.
- [131] S. Eidels-Dubovoi and V. Beltran-Lopez. Powder pattern effects in the ESR spectrum of polycrystalline MgO:Mn^{2+} . *Journal of Magnetic Resonance*, 74(1):94 – 104, 1987.
- [132] V. Beltran-Lopez and J. Castro-Tello. EPR lineshapes in polycrystalline samples: $6\text{S}_{5/2}$ ions in axial and cubic crystal fields. *Journal of Magnetic Resonance (1969)*, 39(3):437 – 460, 1980.
- [133] T. Castner, G. S. Newell, W. C. Holton, and C. P. Slichter. Note on the paramagnetic resonance of iron in glass. *The Journal of Chemical Physics*, 32(3):668–673, 1960.
- [134] R. S. de Biasi and A. Caldas. Electron paramagnetic resonance of Fe^{3+} in orthorhombic symmetry sites in magnesium oxide. *Journal of Physics C: Solid State Physics*, 10(1):107, 1977.
- [135] R. S. de Biasi. Influence of temperature and iron concentration on the ESR spectrum of tetragonal and orthorhombic Fe^{3+} centres in MgO . *Journal of Physics C: Solid State Physics*, 14(32):4885, 1981.